

The Role of Vortex Ring on Propulsion

(推進における渦輪の役割)

2016年3月

羽二生 稔大

The Role of Vortex Ring on Propulsion

The Role of Vortex Ring on Propulsion

Toshihiro Haniu

Doctoral Program in Engineering

Akita University

Tegata gakuen-machi, Akita 010-8502

March 2016

ACKNOWLEDGEMENTS

I would like to show my greatest appreciation to Prof. Hiroaki Hasegawa, Graduate school of Engineering at Utsunomiya University, for useful advice, valuable guidance, and tremendous support of the whole study. Prof. Hideki Takagi, University of Tsukuba, and Asst. Hirofumi Shimojo, Niigata University of Health and Welfare, whose supports and helpful comments in water tunnel test were an enormous help to me and I thank them for their contributions. I want to thank Prof. Masahide Nakamura and Technical Specialist Ms. Oriie Tamura, Graduate School of Engineering & Resource Science at Akita University, for enormous help after the Prof. Hiroaki Hasegawa transferred to Utsunomiya University.

Thanks to members of the Hasegawa lab at Akita University, for their help and providing a great work environment. In particular, thanks to Mr. Shigekazu Tekuramori, Master degree's student, for long-term help and support with wind tunnel experiment in the adverse environment such as high-temperature and humidity.

Finally, I would like to acknowledge my parents for tremendous and moral support over many years.

ABSTRACT

Flying animals and insects flap their wings by using a combination of pitching and heaving oscillations. This movement generates a vortex, which affects unsteady fluid forces. The propulsive force generated by these animals is related to the unsteady forces accompanied with vortex motion. It is well known that vortex motion plays an important role in the generation and enhancement of unsteady fluid forces, which must be considered when estimating the propulsive force generated by swimmers. The purpose of this study is to experimentally explain the mechanism of unsteady fluid force generation from vortex ring structure, and to examine its behavior in typical swimming motions. The swimming actions analyzed in this study include the S-shaped pull used in the front crawl, and the motions associated with the use of a monofin. The unsteady fluid force was calculated from the momentum of a vortex ring. In addition, the effect of the shed vortex ring on the propulsive force was investigated. In an experiment involving a swimmer, the parameters of movement are limited. In addition, in order to measure the 3D vortex structure, motion repeatability is important. Therefore, oscillations of the test model were mechanically controlled by a driver unit. The flow fields were measured using stereoscopic particle image velocimetry (PIV), which was applied at several downstream positions, and three components of velocity measurements were synchronized to the model movements. The fluid force acting on the model was measured by using a load cell. The oscillation that occurs as the angular speed changes generates a strong vortex near the model, enhancing the fluid force. Based on the comparison between the flow field and the fluid force, the vortex near the model affects unsteady fluid force generation to a greater extent than the shed vortex. The variation in propulsive force calculated from the momentum of the growing vortex on the upper surface of the monofin exhibits the same trend as the measured variation. Therefore, there is no large difference between measured and calculated propulsive force during one cycle.

TABLE OF CONTENTS

	<i>Page</i>
ACKNOWLEDGEMENTS	III
ABSTRACT	IV
TABLE OF CONTENTS	V
LIST OF TABLES	VIII
LIST OF FIGURES	IX
 CHAPTER	
1 INTRODUCTION	1
1.1 Background	1
1.2 Literature Review	3
1.3 Aim of This Study	5
 2 EXPERIMENTAL APPARATUS	 7
2.1 Wind Tunnel	7
2.2 Water Channel	7
2.3 Test Models	8
2.4 Fluid Force Measurements	9
2.5 Measurements of Angle of Attack Variation of Test Model	9
2.6 Flow Field Measurements	9
2.6.1 Two Component PIV	9
2.6.2 Stereoscopic PIV	10
2.7 Three-Components Vorticity	11
2.8 Q Invariant of Velocity Gradient Tensor	12
 3 EFFECT OF DIFFERENT AIRFOIL SHAPES ON UNSTEADY LIFT DURING IMPULSIVE INCIDENCE VARIATION	 22
3.1 Experimental method	22
3.2 Results and Discussion	23
3.2.1 Different Discoid Airfoil Motion	23

3.2.2	Different Airfoil Shapes	25
3.3	Conclusions	26
4	VORTEX STRUCTURE AROUND DISCOID AIRFOIL DURING PITCH-OSCILLATING MOTION	45
4.1	Experimental method	45
4.2	Results and Discussions	46
4.3	Conclusions	48
5	EFFECT OF THREE-DIMENSIONAL AIRFOIL SHAPE ON VORTEX RING STRUCTURE DURING PITCHING MOTION	64
5.1	Experimental Method	64
5.2	Results and Discussion	65
5.2.1	3D Vortex Structure around a Discoid Airfoil	65
5.2.2	3D Vortex Structure around a Rectangular Airfoil	66
5.2.3	Fluid Force Characteristics	67
5.3	Conclusions	67
6	PROPULSIVE FORCE AND THREE-DIMENSIONAL VORTEX STRUCTURE DURING MONOFIN OSCILLATION	78
6.1	Experimental Method	78
6.2	Results and Discussion	79
6.3	Conclusions	82
7	PROPULSIVE FORCE CALCULATION BASED ON VORTEX RING	93
7.1	Experimental Method	93
7.1.1	Theory of Propulsive Force Calculation	93
7.1.2	Area Calculation of Vortex Ring	94
7.1.3	Circulation Calculation of Vortex Ring	95
7.2	Results and Discussion	95
7.3	Conclusions	98
8	SUMMARY	104

REFERENCES	106
APPENDICES	110
A. LIST OF USED SYMBOLS	110
B. PROPULSIVE FORCE ESTIMATION PROGRAM BASED ON VORTEX RING MOMENTUM	112

LIST OF TABLES

<i>Table</i>	<i>Page</i>
6.1 Ratio of kick-up and kick-down speed · · · · ·	84

LIST OF FIGURES

<i>Figure</i>	<i>Page</i>
2.1.1 Wind tunnel schematic · · · · ·	14
2.1.2 Test section for the wind tunnel test · · · · ·	14
2.2.1 Water channel schematic · · · · ·	15
2.2.2 Test section for the water channel test · · · · ·	15
2.3.1 Discoid airfoil	
(a) Discoid airfoil dimensions (mm) · · · · ·	16
(b) Discoid airfoil shape · · · · ·	16
2.3.2 Rectangular airfoil dimensions (mm) · · · · ·	16
2.3.3 Triangular airfoil dimensions (mm) · · · · ·	17
2.4 Monofin shape · · · · ·	17
2.5 Fluid force measurement system · · · · ·	18
2.6 Schematic of the 2C PIV system used for the wind tunnel test	
(a) x - z plane · · · · ·	19
(b) x - y plane · · · · ·	19
2.7 Schematic of the Stereoscopic PIV system used for the wind tunnel test · · ·	20
2.8 Schematic of the Stereoscopic PIV system used for the water channel test · ·	20

2.9 Computational domain	
(a) Inside	21
(b) Boundary	21
3.1 The temporal change in angle of attack	28
3.2 The measurement region for stereoscopic PIV for impulsive incidence variation	28
3.3 Lift curve for the discoid airfoil in the stationary condition	29
3.4 Lift curve for the discoid airfoil as it is impulsively changed from 0° – 36° at $T^* = 2.0$	30
3.5 Lift curve for the discoid airfoil as it is impulsively changed from 36° – 0° at $T^* = 2.0$	30
3.6 Three-dimensional vortex structure for the discoid airfoil as it is impulsively changed from 0° – 36° for $T^* = 2.0$	
(a) $tUdc = 0$	31
(b) $tUdc = 1$	31
(c) $tUdc = 2$	31
(d) $tUdc = 3$	32
(e) $tUdc = 5$	32
(f) $tUdc = 7$	32
(g) $tUdc = 12$	33
(h) $tUdc = 20$	33
(i) $tUdc = 30$	33
3.7 Three-dimensional vortex structure of ω_y for the discoid airfoil as it is impulsively changed from 0° – 36° for $T^* = 2.0$	
(a) $tUdc = 1$	34
(b) $tUdc = 2$	34

(c) $tUdc = 3$	34
(d) $tUdc = 7$	34
(e) $tUdc = 12$	34
(f) $tUdc = 30$	34
3.8 Three-dimensional vortex structure of ω_x for the discoid airfoil as it is impulsively changed from 0° – 36° for $T^* = 2.0$	
(a) $tUdc = 1$	35
(b) $tUdc = 2$	35
(c) $tUdc = 3$	35
(d) $tUdc = 7$	35
(e) $tUdc = 12$	35
(f) $tUdc = 30$	35
3.9 Three-dimensional vortex structure for the discoid airfoil as it is impulsively changed from 36° – 0° for $T^* = 2.0$	
(a) $tUdc = 0$	36
(b) $tUdc = 1$	36
(c) $tUdc = 2$	36
(d) $tUdc = 3$	37
(e) $tUdc = 5$	37
3.10 Density map of vorticity in the x – z plane for the discoid airfoil as it is impulsively changed from 36° – 0° for $T^* = 2.0$	
(a) $tUdc = 2$	38
(b) $tUdc = 3$	38
3.11 Lift curve for the triangular airfoil in the stationary condition	
	38
3.12 Lift curve for the triangular airfoil as it is impulsively changed from 0° – 18°	
(a) $T^* = 5$	39
(b) $T^* = 2$	39

3.13 Lift curve for the triangular airfoil as it is impulsively changed from 0° – 36°

- (a) $T^* = 5$ 40
 (b) $T^* = 2$ 40

3.14 Three-dimensional vortex structure for the triangular airfoil as it is impulsively changed from 0° – 36° for $T^* = 2.0$

- (a) $tUdc = 0$ 41
 (b) $tUdc = 1.5$ 41
 (c) $tUdc = 2$ 41
 (d) $tUdc = 3$ 42
 (e) $tUdc = 7$ 42
 (f) $tUdc = 15$ 42

3.15 Three-dimensional vortex structure of ω_y for the triangular airfoil as it is impulsively changed from 0° – 36° for $T^* = 2.0$

- (a) $tUdc = 0$ 43
 (b) $tUdc = 1$ 43
 (c) $tUdc = 2$ 43
 (d) $tUdc = 3$ 43
 (e) $tUdc = 7$ 43
 (f) $tUdc = 15$ 43

3.16 Three-dimensional vortex structure of ω_x for the triangular airfoil as it is impulsively changed from 0° – 36° for $T^* = 2.0$

- (a) $tUdc = 0$ 44
 (b) $tUdc = 1$ 44
 (c) $tUdc = 2$ 44
 (d) $tUdc = 3$ 44
 (e) $tUdc = 7$ 44
 (f) $tUdc = 15$ 44

4.1 The temporal change of α during pitch-oscillating motion

- (a) Type-1 50

(b) Type-2 · · · · ·	50
4.2 Measurement region for 2CPIV	
(a) x - z plane · · · · ·	51
(b) x - y plane · · · · ·	51
4.3 Calculation of fluid forces using a momentum conservation law · · · · ·	
4.4 Three-dimensional vortex structure under stationary condition at $Re = 3.0 \times 10^4$	
(a) $\alpha = 90^\circ$ · · · · ·	53
(b) $\alpha = 69.8^\circ$ · · · · ·	53
(c) $\alpha = 110.2^\circ$ · · · · ·	53
4.5 Density map of vorticity in the x - z plane for Type-1 at $y/c = 0.0$ and $Re = 3.0 \times 10^4$	
(a) $t' = 0$ · · · · ·	54
(b) $t' = 0.13$ · · · · ·	54
(c) $t' = 0.25$ · · · · ·	54
(d) $t' = 0.4$ · · · · ·	54
(e) $t' = 0.5$ · · · · ·	54
(f) $t' = 0.63$ · · · · ·	54
(g) $t' = 0.75$ · · · · ·	54
(h) $t' = 0.9$ · · · · ·	54
4.6 Density map of vorticity in the x - z plane for Type-1 at $y/c = 0.4$ and $Re = 3.0 \times 10^4$	
(a) $t' = 0$ · · · · ·	55
(b) $t' = 0.13$ · · · · ·	55
(c) $t' = 0.25$ · · · · ·	55
(d) $t' = 0.4$ · · · · ·	55
(e) $t' = 0.5$ · · · · ·	55
(f) $t' = 0.63$ · · · · ·	55

(g) $t' = 0.75$ ·····	55
(h) $t' = 0.9$ ·····	55

4.7 Density map of vorticity in the x - z plane for Type-2 at $y/c = 0.0$ and $Re = 3.0 \times 10^4$

(a) $t' = 0$ ·····	56
(b) $t' = 0.13$ ·····	56
(c) $t' = 0.25$ ·····	56
(d) $t' = 0.4$ ·····	56
(e) $t' = 0.5$ ·····	56
(f) $t' = 0.63$ ·····	56
(g) $t' = 0.75$ ·····	56
(h) $t' = 0.9$ ·····	56

4.8 Time history of the fluid force variation during pitch-oscillating motion at $Re = 3.0 \times 10^4$ ·····

57

4.9 Three-dimensional vortex structure for Type-1 at $Re = 3.0 \times 10^4$

(a) $t' = 0$ ·····	58
(b) $t' = 0.13$ ·····	58
(c) $t' = 0.25$ ·····	58
(d) $t' = 0.4$ ·····	59
(e) $t' = 0.5$ ·····	59
(f) $t' = 0.63$ ·····	59
(g) $t' = 0.75$ ·····	60
(h) $t' = 0.9$ ·····	60

4.10 Three-dimensional vortex structure for Type-2 at $Re = 3.0 \times 10^4$

(a) $t' = 0$ ·····	61
(b) $t' = 0.13$ ·····	61
(c) $t' = 0.25$ ·····	61
(d) $t' = 0.4$ ·····	62
(e) $t' = 0.5$ ·····	62

(f) $t' = 0.63$	62
(g) $t' = 0.75$	63
(h) $t' = 0.9$	63
5.1 Measurement region of stereoscopic PIV	69
5.2 Three-dimensional vortex structure around the pitch-oscillating discoid airfoil for $k = 0.97$ and $Re = 3.0 \times 10^4$	
(a) $t' = 0.08$	70
(b) $t' = 0.25$	70
(c) $t' = 0.42$	70
(d) $t' = 0.58$	71
(e) $t' = 0.75$	71
(f) $t' = 0.92$	71
5.3 Three-dimensional vortex structure of each vorticity component around the discoid airfoil for $k = 0.97$ and $Re = 3.0 \times 10^4$	
(a) $t' = 0.08$	72
(b) $t' = 0.25$	72
(c) $t' = 0.42$	72
(d) $t' = 0.58$	72
(e) $t' = 0.75$	72
(f) $t' = 0.92$	72
5.4 Time history of each vorticity component during a pitch-oscillating cycle for the discoid airfoil for $k = 0.97$ and $Re = 3.0 \times 10^4$	73
5.5 Three-dimensional vortex structure around the pitch-oscillating rectangular airfoil for $k = 0.97$ and $Re = 3.0 \times 10^4$	
(a) $t' = 0.08$	74
(b) $t' = 0.25$	74
(c) $t' = 0.42$	74
(d) $t' = 0.58$	75

(e) $t' = 0.75$	75
(f) $t' = 0.92$	75
5.6 Three-dimensional vortex structure of each vorticity component around the rectangular airfoil for $k = 0.97$ and $Re = 3.0 \times 10^4$	
(a) $t' = 0.08$	76
(b) $t' = 0.25$	76
(c) $t' = 0.42$	76
(d) $t' = 0.58$	76
(e) $t' = 0.75$	76
(f) $t' = 0.92$	76
5.7 Time history of each vorticity component during a pitch-oscillating cycle for the rectangular airfoil for $k = 0.97$ and $Re = 3.0 \times 10^4$	
	77
5.8 Fluid force curve during pitch-oscillating motion for $k = 0.97$ and $Re = 4.0 \times 10^4$	
	77
6.1 The temporal change of α during oscillating motion	
	84
6.2 Measurement region of stereoscopic PIV for the monofin	
	85
6.3 Propulsive force variation during one kick stroke	
	85
6.4 Contour map of vorticity and velocity vectors in the x - z plane ($y = 0$ mm) at the time immediately after the propulsive force reaches its maximum value	
(a) Standard	86
(b) Fast kick-up 1	86
(c) Fast kick-down 1	86
6.5 Three-dimensional vortex structure for the standard case	
(a) $t' = 0$	87
(b) $t' = 0.17$	87

(c) $t' = 0.33$ ·····	87
(d) $t' = 0.5$ ·····	88
(e) $t' = 0.75$ ·····	88
(f) $t' = 0.83$ ·····	88
6.6 Three-dimensional vortex structure for the fast kick-up 1 case	
(a) $t' = 0$ ·····	89
(b) $t' = 0.17$ ·····	89
(c) $t' = 0.42$ ·····	89
(d) $t' = 0.58$ ·····	90
(e) $t' = 0.75$ ·····	90
(f) $t' = 0.92$ ·····	90
6.7 Three-dimensional vortex structure for the fast kick-down 1 case	
(a) $t' = 0$ ·····	91
(b) $t' = 0.17$ ·····	91
(c) $t' = 0.33$ ·····	91
(d) $t' = 0.5$ ·····	92
(e) $t' = 0.67$ ·····	92
(f) $t' = 0.83$ ·····	92
7.1 Detection of vortex line	
(a) Top view ·····	100
(b) Perspective view ·····	100
7.2 Calculation of vortex ring profile area	
(a) Profile area in the x direction A_x ·····	101
(b) Profile area in the z direction A_z ·····	101
7.3 Calculation of vortex ring circulation ·····	
102	
7.4 Circulation calculated by Stokes theorem with respect to the threshold percentage of the maximum vorticity ·····	
102	

7.5 Propulsive force calculated from vortex ring in the wake of the monofin . . . 103

7.6 Contribution of the upstream and downstream sides of a vortex ring to the momentum in the freestream direction 103

1. INTRODUCTION

1.1 Background

The importance of unsteady effects was demonstrated by animal flight at low Reynolds numbers. Because, a quasi-steady-state approach to predicting fluid forces acting on an insect wing leads to errors that suggest that flight using steady fluid force is impossible. Vortex motion plays an important role in the generation of unsteady fluid forces. Flying and aquatic animals generate a vortex by oscillating their wings or fins, respectively, and unsteady fluid forces are generated by the change in vortex movement. In the two-dimensional flow field, flapping insects create a leading edge vortex (LEV) on the upper surfaces of their wings. The lift is generated by the presence of a low-pressure region in the LEV core. In recent years, the development of numerical analyses and a flow field measuring technique have allowed for greater investigation of the three-dimensional vortex structure. The vortex ring generated by flapping motion has downward momentum, and it is suggested that insects fly using the reaction force of momentum generation. However, the relationship between the three-dimensional vortex (vortex ring) structure and unsteady fluid forces is inconclusive.

It seems that during front crawl and monofin swimming motions, the swimmer effectively uses the unsteady effect to move through the water. For example, the propulsive force of a swimmer engaged in a front crawl is mainly generated by hand motion, and the actual motion of their hand is noticeably unsteady. In particular, the unique S-shaped pulling motion performed during crawl stroke creates circumstances in which the direction

of circulation around the hand changes during the cycle of a single stroke. Namely, during one cycle of pitch-oscillation, the leading edge of the discoid airfoil (which simulates the hand of a swimmer) displaces the trailing edge. From the results of the experiment using a swimmer, it has been predicted that the swimmer uses the unsteady lift created by the shed vortex and bound vortex around their hand, which is enhanced by vortex shedding. Therefore, unsteady forces must be considered when estimating the propulsive forces of swimmers performing the front crawl. A monofin is a type of swim fin typically used in underwater sports, such as fin swimming, free diving, and underwater orienteering. In addition, monofins have been used for fin swimming competitions. Monofin swimmers can reach speeds up to 3.58 m/s. It is known that monofin fin swimmers are much faster than freestyle swimmers. The monofin swimmer uses their body to undulate waves towards the monofin, similar to a dolphin kick. The actual motion of a monofin is obviously unsteady; however, the three-dimensional vortex structure, and the unsteady fluid forces associated with swimmer propulsion were not investigated. Furthermore, the reduced frequency (which represents unsteady effect magnitude) and Reynolds number achieved by a swimmer are very different from flying animals, so it is impossible to apply the earlier study on insect/bird flapping to swimming.

If the relationship between the unsteady fluid force and the vortex ring can be clarified, it will allow for the propulsive force generated by a swimmer to be optimized from a hydrodynamical point of view. In addition, an understanding of the unsteady fluid force generation mechanism has application to not only the enhancement of the propulsive force generated by the swimmer, but also to the aerospace field. For example, improving propulsive efficiency makes it possible to achieve high performance while using minimal energy. It can be expected that the lift enhancement enabled by the unsteady fluid force can be applied to MAVs (Micro Air Vehicles). MAVs can explore buildings destroyed by earthquakes or serve as exploration spacecraft on Mars where the low-density atmosphere makes it

difficult for wings to maintain steady lift.

1.2 Literature Review

The quasi-steady assumption was used to explain the flight mechanism of insects or birds. The lift force calculation based on the quasi-steady theory was performed for hovering hummingbirds and drosophila by Weis-Fogh (1972) [1]. Weis-Fogh concluded that the hovering flight of hummingbirds and drosophila is consistent with quasi-steady theory. On the other hand, Ellington (1984) showed that a quasi-steady state approach using the more accurate kinematic data of wing movement yielded errors, suggesting that flight is impossible [2]. Gray (1936) estimated the propulsive force generated by a dolphin based on its muscle weight, and he indicated that the swimming speed estimated from dolphin's muscle weight is not reached the actual one (known as the Gray's paradox) [3]. Therefore, the influence of unsteady effects on the flight and propulsion of animate beings is important. It is known that the fluid force generated by unsteady motion (unsteady fluid force) is greater than the fluid force generated under stationary conditions. For example, when a wing with an angle of attack changes suddenly from rest, the unsteady lift is twice as large as the steady lift (Izumi (1983) [4]).

In recent years, many studies have been conducted to investigate the relationship between unsteady fluid force generation and the flow field. Sane (2003) summarized the fundamental unsteady mechanism in terms of insect flight [5]. The importance of LEV on lift generation in insect flight is indicated by Maxworthy (1979) [6]. The effect of Reynolds number on the LEV and fluid force for flapping wings was studied by Birch et al. (2003), and they concluded that the LEV is enhanced as the Reynolds number is increased [7]. Zhao et al. (2011) showed that the lift force is increased with increasing LEV strength, which is caused by a decrease in wing flexibility [8]. Recently, three-dimensional investigations of flow fields were conducted as a

result of improvements made to the particle image velocimetry (PIV) technique. For example, the three-dimensional vortex structure generated during the pitching and surging of flat revolving plates was measured using tomographic PIV (Percin et al. (2015) [9]). This technique is able to obtain three-component velocity in 3D volume. The temporal sequence of the vortex ring on a live butterfly wing was measured in three dimensions by Fuchiwaki et al. (2013) [10]. A series of linked vortex rings generated by dorsal, caudal, and anal fins in the wake of free swimmers was shown (Flammang et al. (2011) [11]). However, the relationship between the mechanism of unsteady fluid force generation and flow field remains unclear. Several studies have been conducted to estimate propulsive force from the flow field. The self-energy of a vortex ring in the wake of free-swimming fish was computed by Muller et al. (1977) [12], and the impulse was estimated from the momentum of the vortex ring generated by an 'S' type turning fish (Epps et al. (2007) [13]). Nauen et al. (2002) computed the time-averaged thrust forces from the vortex ring in the wake of steadily swimming fish, and the results suggested that the estimated thrust forces were not different from the drag force measured by towing the fish body [14]. The time-varying propulsive force acting on the fin was calculated from the momentum of the vortex ring connected to the fin (Imamura et al. (2013) [15]), using the method developed by Dickinson (1996) [16]. However, the propulsive force calculated from the vortex ring was overestimated because the circulation was calculated by the spanwise vorticity in the central plane of the fin.

Many studies have been conducted to estimate the propulsive forces of swimmers performing the front crawl (Schleithauf et al. (1983) [17] and Berger et al. (1995) [18]). This estimation has been essentially based on the quasi-steady flow theory. In the quasi-steady flow theory, the magnitude of force is proportional to the square of the sweep speed of the hand of a swimmer. However, during an S-shaped pull, hand speed is faster for an expert swimmer than it is for a novice swimmer (Matsuuchi (2007) [19]). In particular, the unique S-shaped pulling motion of the crawl stroke creates a

scenario in which the direction of circulation around the hand changes during the cycle of a single stroke (Matsuuchi et al. (2008) [20]). In a previous study, fundamental unsteady pitch-oscillating motion was utilized to investigate the effects of airfoil shape on the unsteady fluid forces, and the differences in the effects of unsteadiness on the discoid airfoil and the NACA 0012 airfoil were considered (Hasegawa et al. (2010) [21]). It was concluded that the vortex grows and the fluid force increases when the reduced frequency of oscillation is increased, and the effect of unsteadiness during pitch-oscillating motion varies depending on airfoil shape.

Several kinematic and dynamic studies have been reported on monofin swimming. The propulsive force acting on the fin swimmer was calculated by a simulation that uses the measured bending stiffness and damping coefficient of a monofin (Nakashima et al. (2010) [22]). The influence of gender, skill level, and race distance on selected kinematic parameters of surface monofin swimming were measured by Gautier et al. (2004) [23]. Nicolas et al. (2009) compared efficiency and active drag kinematic parameters for an underwater and surface fin swimming trial [24]. The monofin swimmer uses their body to undulate waves towards the monofin (Arellano et al. (2002) [25] and Nicolas et al. (2007) [26]), similar to a dolphin kick. The actual motion of a monofin is unsteady, meaning that these forces must also be considered when estimating the propulsive force generated by a monofin.

1.3 Aim of This Study

The purpose of this study is to investigate the relationship between unsteady fluid force and three-dimensional vortex structure. The specific goals of this study are described as follows:

1. To understand the fundamental relationship between unsteady fluid force and vortex structure [27].

2. To investigate the effect of differing oscillating motions on vortex generation [28, 29].
3. To clarify the effects of three-dimensional airfoil shapes on vortex ring structures [30, 31].
4. To estimate the unsteady fluid force acting on the model from the vortex ring, and to explain the influence of the vortex ring scenario (i.e. shed or attached the vortex ring on monofin) on force generation.

The contents of this study are described as follows: Chapter 1 contains the introduction, which includes background information and the goals of this study. In Chapter 2, we explain the experimental apparatus for the wind tunnel and water channel test. In Chapter 3, the unsteady lift and flow field was investigated during impulsive incidence variation of the angle of attack. In Chapter 4, we examine the three-dimensional vortex structure around the discoid airfoil. This structure is observed during pitch-oscillating motion around an oscillating 90° center angle as the angular speed is changed. The effect of three-dimensional airfoil shape on vortex structures during pitching motions was researched in Chapter 5. In Chapter 6, the propulsive force and vortex ring were investigated for the monofin using the driver unit. In Chapter 7, the propulsive force was estimated from the momentum of the vortex ring using the results obtained in Chapter 6. In Chapter 8, we summarize the results of the study.

2. EXPERIMENTAL APPARATUS

2.1 Wind Tunnel

The experiments were carried out using a low-speed, open-type wind tunnel. Figure 2.1.1 shows the schematic of the wind tunnel. The wind tunnel consists of the driving section, diffuser, rectifier portion, nozzle, and test section. The wind tunnel was driven by an electric blower (Showa fan A-7KM, Showa Denki Co., Ltd). The total length from the diffuser inlet to the nozzle outlet is 3,780 mm. Three screens were set in the diffuser, and the rectifier portion has a honeycomb and four screens. Freestream velocity varied from 0–30 m/s with a freestream turbulence intensity of 5 %. Figure 2.1.2 shows the test section used to measure the flow field. The test section is constructed with acrylic plate, and its inlet dimensions are 300×300 mm. The origin of the coordinate system is defined as the center of the model. The velocity is denoted by three components (u , v , and w) in three directions (x , y , z .) The oscillating motions of the airfoil were generated using a five-phase stepping motor (RK544, Oriental Motor Co., Ltd.) with a 0.072° step around its mid-chord axis. The stepping motor was controlled using a personal computer.

2.2 Water Channel

The experiments for the monofin were performed using a circular water channel, and Figure 2.2.1 shows its schematic. The test section has a length of 4.6 m, a span of 2.0 m, and a depth (water level) of 1.2 m. The

glass-windowed observation sections are positioned on the side and at the bottom of the test section to perform the flow visualization. The freestream velocity varied from 0–2.5 m/s at equal intervals of 0.1 m/s. Figure 2.2.2 shows the test section and the driver unit used for the monofin. The origin of the coordinate system is defined as the center of the oscillation axis. Monofin oscillation is performed by using a stepping motor (AR911AA-3, Oriental Motor Co., Ltd.) set at the top of the driver unit. The power of the motor is transmitted to the oscillation axis via two belt pulleys and a crank mechanism.

2.3 Test Models

For the wind tunnel test, three types of airfoils were used to investigate the effect of airfoil shape on vortex structure. The schematic of a discoid airfoil (to simulate the hand of swimmer), a rectangular airfoil (with a NACA 0015 profile), and a triangular airfoil are shown in Figs. 2.3.1, 2.3.2 and 2.3.3, respectively. The discoid airfoil is created by rotating the NACA 0015 profile from the leading edge to the maximum thickness around its mid-chord axis (Fig. 2.3.1 (b)). Each airfoil has a chord, c , of 150 mm and a span of 150 mm. The maximum thicknesses of the discoid airfoil, the rectangular airfoil, and the triangular airfoil are 37.5 mm, 22.5 mm and 22.5 mm, respectively. The oscillating axis was fixed at 75 mm from the leading edge for the discoid and rectangular airfoils, and 100 mm from the leading edge for the triangular airfoil. The airfoil edge has a smooth, semi-circular shape.

In the water channel test, a monofin (similar to the caudal fin of a dolphin) was used, and its schematic is shown in Fig. 2.4. The monofin has a chord, c , of 320 mm and a span of 360 mm. The monofin was made from laminate composite materials and its thickness decreased from the root to the tip.

2.4 Fluid Force Measurement

Two types of load cells were used in this study because the range of the fluid force is widely different between wind tunnel and water channel measurements. In the wind tunnel test, a 50 mN, ultra-small capacity, load cell (LVS-500GA, Kyowa Electronic Instruments Co., Ltd.) is used. The load cell was set at one end of the oscillating axis. In the water channel test, a 200 N compact tension/compression load cell (LUR-A-SA1, Kyowa Electronic Instruments Co., Ltd.) is used. The load cell was fixed on the front side of the frame, which was set at the top of the water channel. The monofin drive unit was placed on the slider of the frame and can move freely in the x -direction (Fig. 2.5). Therefore, the fluid force acting on the monofin was measured by connecting the load cell and driver unit. The output of the load cell was imported to a personal computer via a dynamic strain amplifier (DPM-601AM67, Kyowa Electronic Instruments Co., Ltd.) and an A/D board (AD16-16U(PCI)EH, Contec Co., Ltd.).

2.5 Measurement of Angle of Attack Variation of Test Model

To confirm the oscillation of the model, the time series data of the angle of attack was measured using a potentiometer. The potentiometer was fixed at one end of the oscillating axis. In the water channel test, the potentiometer was covered by a waterproof case.

2.6 Flow Field Measurements

2.6.1 Two Component PIV

Figure 2.6 shows the two component (2C) PIV system, which is able to measure two-dimensional, two-component velocity in the measuring plane. The 2C PIV system consists of a high-speed camera (FASTCAM SA3, Photron Co., Ltd.) and an Nd-YAG laser (PIV G8000 Laser, Katokoken Co., Ltd.). The tracer particle is glycol oil mist with a particle diameter ranging from 0.3–1 μm , and it is generated by a smoke generator (Model 8304, Kanomax Inc.). Fig. 2.6 (a) and (b) show the configuration of the PIV system in the x - z and x - y plane, respectively. In the x - z plane, the vertical laser sheet is deflected by a mirror set at the top of the test section, and the particle images are captured from the side of the test section using the high-speed camera (Fig. 2.6 (a)). In the x - y plane, the horizontal laser sheet irradiates the directly and the particle images are captured from the top of the test section through the mirror (Fig. 2.6 (b)).

2.6.2 Stereoscopic PIV

The flow fields were measured using a stereoscopic PIV method that is able to measure two-dimensional, three-component velocity in the measurement plane. In the wind tunnel test, the stereo PIV system consists of a double pulse Nd: YAG laser (Solo 120XT, New Wave Research, Inc.) and two charge-coupled device (CCD) cameras (Megaplus ES1.0, $1,008 \times 1,024$ pixels, Kodak Co., Ltd.); the stereo PIV system is shown Fig. 2.7. The tracer particle is glycol oil mist. The 3 mm thick laser sheet was irradiated in the y - z plane from the side of the test section, and two CCD cameras were placed on both sides of the test section to capture the particle images. The PIV cameras were mounted on a specially designed rig with an adjustable viewing angle. The angle between the optical axes of the two cameras was set to approximately 90° to satisfy the Scheimpflug condition. The time interval, Δt , between two sequence image capturing was set to 0.5 ms. To synchronize image capture with the airfoil motion, the flow fields were measured based on a timing cycle generated by the trigger of the pulse generator (Model 9314,

Quantum Composers, Inc.). Figure 2.8 shows the stereoscopic PIV system in the water channel test. The measurement was tested on the 8 mm wide laser sheet at a time interval, Δt , of 2.5 ms.

2.7 Three-Component Vorticity

The three components of vorticity are defined as

$$(\omega_x, \omega_y, \omega_z) = \left(\frac{\partial w}{\partial y} - \frac{\partial v}{\partial z}, \frac{\partial u}{\partial z} - \frac{\partial w}{\partial x}, \frac{\partial v}{\partial x} - \frac{\partial u}{\partial y} \right) \quad (2.1)$$

Each term on the right hand side of Eq. (2.1) is disregarded by using the central finite difference approximation for the second order. Considering ω_x by using the Taylor expansion around the points w_n , w_{n+1} , and w_{n-1} (Fig. 2.9 (a)) are follow

$$w_{n\pm 1} = w(y \pm \Delta y) = w_n \pm \Delta y w_n' + \frac{1}{2} (\Delta y)^2 w_n'' + \dots \quad (2.2)$$

Hence,

$$\frac{\partial w}{\partial y} = w_n' \approx \frac{w_{n+1} - w_{n-1}}{2\Delta y} \quad (2.3)$$

Similarly, $\partial v / \partial z$ is written as

$$\frac{\partial v}{\partial z} = v_n' \approx \frac{v_{n+1} - v_{n-1}}{2\Delta z} \quad (2.4)$$

where Δy and Δz represent the mesh spacing of the PIV in the spanwise and heightwise direction, respectively. At the boundary in the measurement region, one side difference is used. w_{n+1} and w_{n+2} (Fig. 2.9 (b)) are written as

$$w_{n\pm 1} = w_n \pm \Delta y w_n' + \frac{(\pm \Delta y)^2}{2!} w_n'' + \dots \quad (2.5)$$

$$w_{n\pm 2} = w_n \pm 2\Delta y w_n' + \frac{(\pm 2\Delta y)^2}{2!} w_n'' + \dots \quad (2.6)$$

Hence,

$$\frac{\partial w}{\partial y} = w_n' \approx \frac{\mp 3w_n \pm 4w_{n\pm 1} \mp w_{n\pm 2}}{2\Delta y} \quad (2.7)$$

$$\frac{\partial v}{\partial z} = v_n' \approx \frac{\mp 3v_n \pm 4v_{n\pm 1} \mp v_{n\pm 2}}{2\Delta z} \quad (2.8)$$

ω_y and ω_z are calculated in the similar way.

2.8 Q Invariant of Velocity Gradient Tensor

The velocity gradient tensor is shown as

$$\nabla u = \frac{\partial u_i}{\partial x_j}. \quad (2.9)$$

∇u can be divided into the symmetric tensor and the antisymmetric tensor.

$$\nabla u = \frac{1}{2} \left(\frac{\partial u_j}{\partial x_i} + \frac{\partial u_i}{\partial x_j} \right) + \frac{1}{2} \left(\frac{\partial u_j}{\partial x_i} - \frac{\partial u_i}{\partial x_j} \right) = S_{ij} + \Omega_{ij}, \quad (2.10)$$

where S_{ij} and Ω_{ij} represent the stretching tensor rate and the rotation tensor rate, respectively. Each tensor is written by

$$S_{ij} = \begin{bmatrix} \frac{\partial u}{\partial x} & \frac{1}{2} \left(\frac{\partial v}{\partial x} + \frac{\partial u}{\partial y} \right) & \frac{1}{2} \left(\frac{\partial u}{\partial z} + \frac{\partial w}{\partial x} \right) \\ \frac{1}{2} \left(\frac{\partial v}{\partial x} + \frac{\partial u}{\partial y} \right) & \frac{\partial v}{\partial y} & \frac{1}{2} \left(\frac{\partial w}{\partial y} + \frac{\partial v}{\partial z} \right) \\ \frac{1}{2} \left(\frac{\partial u}{\partial z} + \frac{\partial w}{\partial x} \right) & \frac{1}{2} \left(\frac{\partial w}{\partial y} + \frac{\partial v}{\partial z} \right) & \frac{\partial w}{\partial z} \end{bmatrix}, \quad (2.11)$$

$$\Omega_{ij} = \begin{bmatrix} 0 & -\frac{1}{2} \left(\frac{\partial v}{\partial x} - \frac{\partial u}{\partial y} \right) & \frac{1}{2} \left(\frac{\partial u}{\partial z} - \frac{\partial w}{\partial x} \right) \\ \frac{1}{2} \left(\frac{\partial v}{\partial x} - \frac{\partial u}{\partial y} \right) & 0 & -\frac{1}{2} \left(\frac{\partial w}{\partial y} - \frac{\partial v}{\partial z} \right) \\ -\frac{1}{2} \left(\frac{\partial u}{\partial z} - \frac{\partial w}{\partial x} \right) & \frac{1}{2} \left(\frac{\partial w}{\partial y} - \frac{\partial v}{\partial z} \right) & 0 \end{bmatrix}. \quad (2.12)$$

The second invariant of the velocity gradient tensor, Q , is defined as

$$Q = \Omega_{ij} \Omega_{ij} - S_{ij} S_{ij}. \quad (2.13)$$

Namely, Q is a local measure of the excess rotation rate relative to the strain rate. The vortices are defined as the region where the magnitude of the

rotation rate is greater than the magnitude of the strain rate, i.e. $Q > 0$
(Miura et al. (1998) [32]).

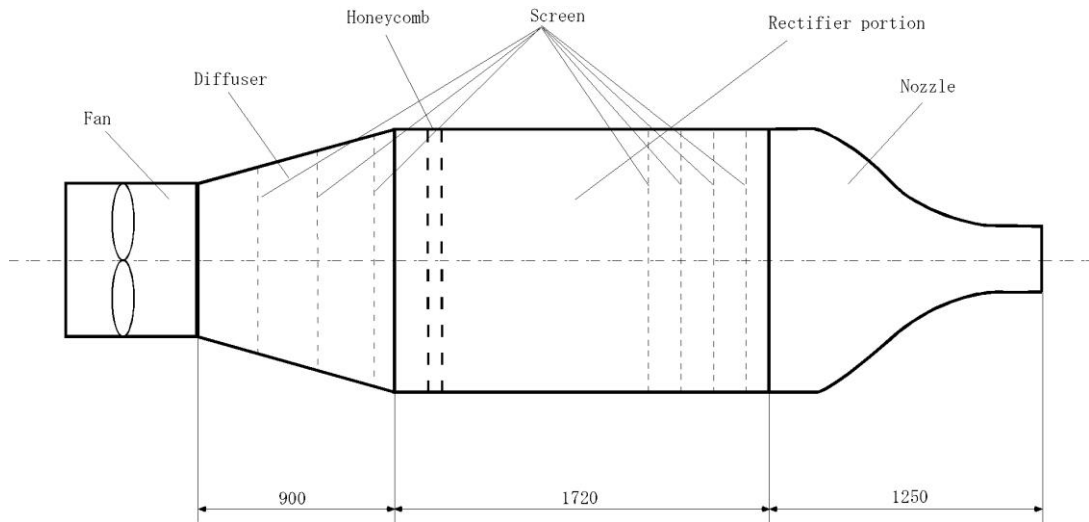


Fig. 2.1.1 Wind tunnel schematic

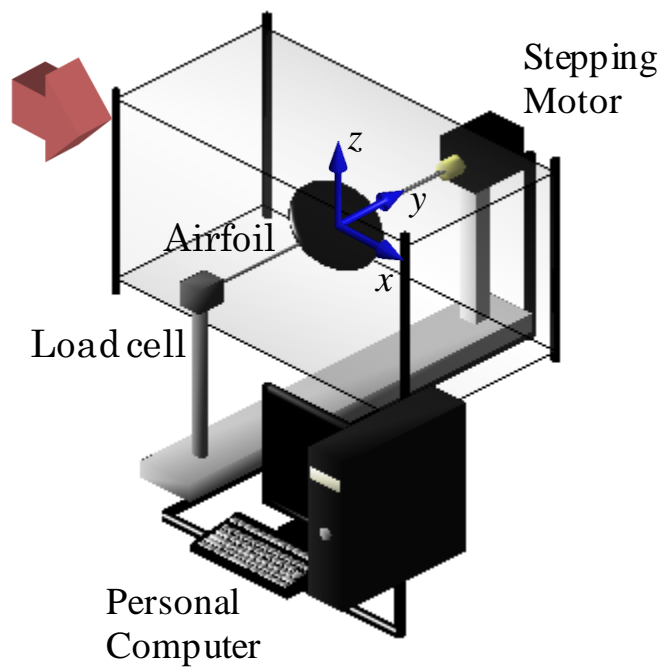


Fig. 2.1.2 Test section for the wind tunnel test

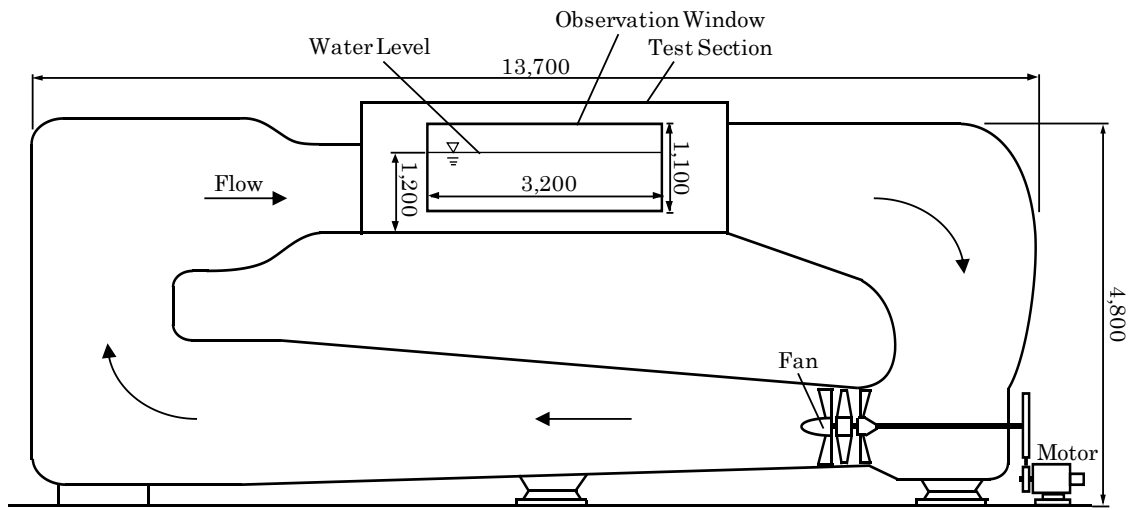


Fig. 2.2.1 Water channel schematic

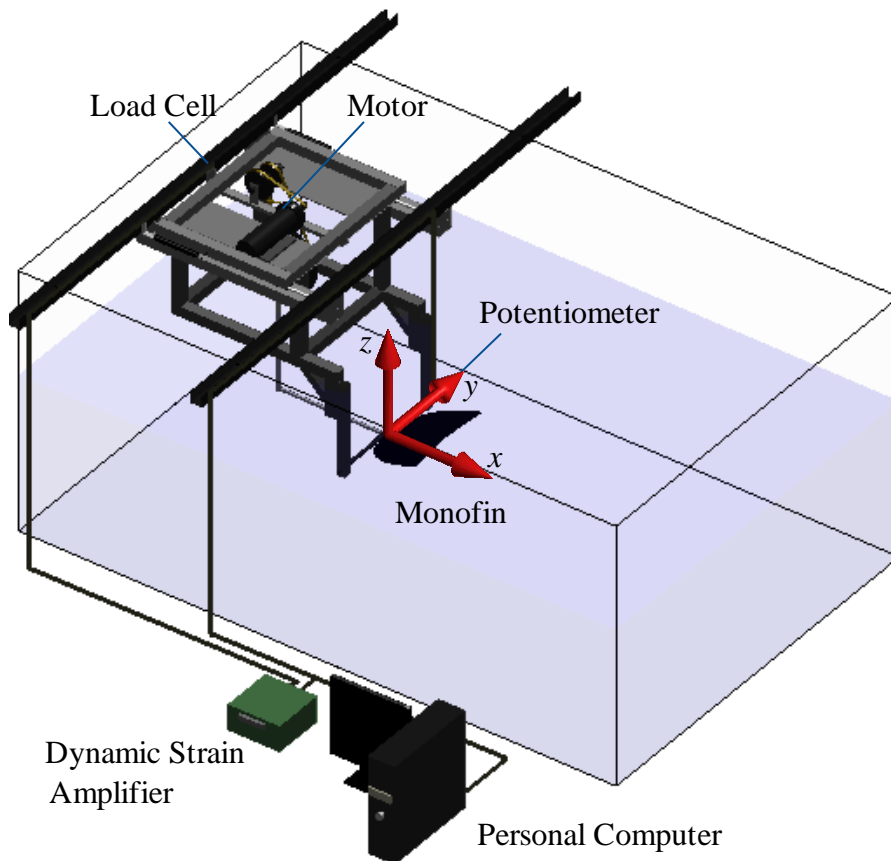
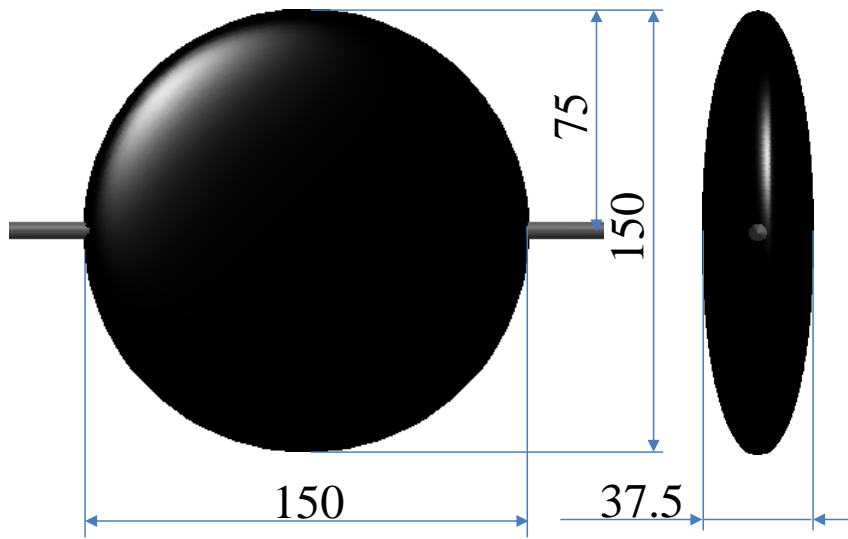
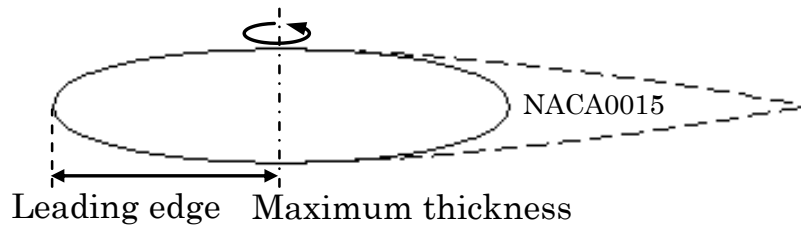


Fig. 2.2.2 Test section for the water channel test



(a) Discoid airfoil dimensions (mm)



(b) Discoid airfoil shape

Fig. 2.3.1 Discoid airfoil

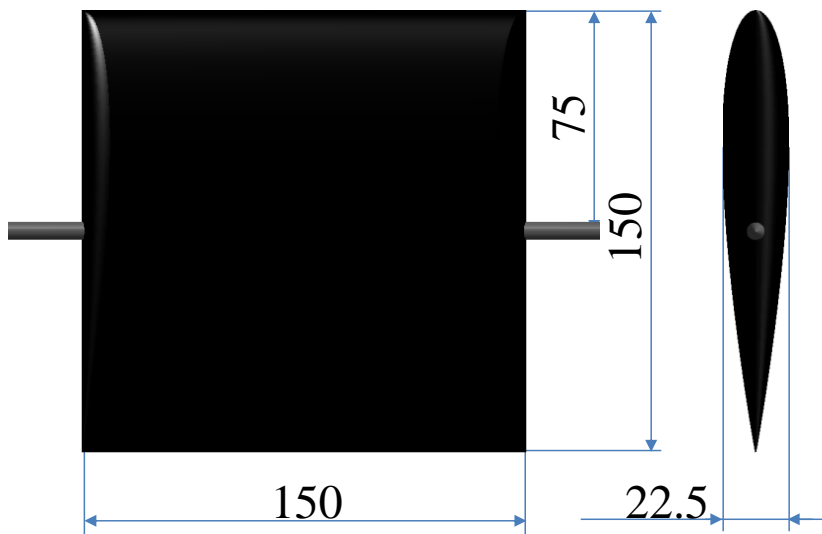


Fig. 2.3.2 Rectangular airfoil dimensions (mm)

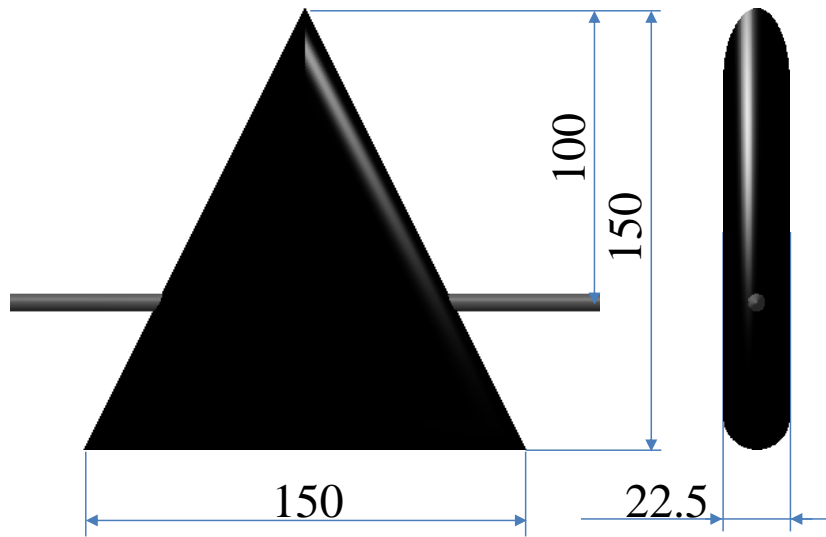
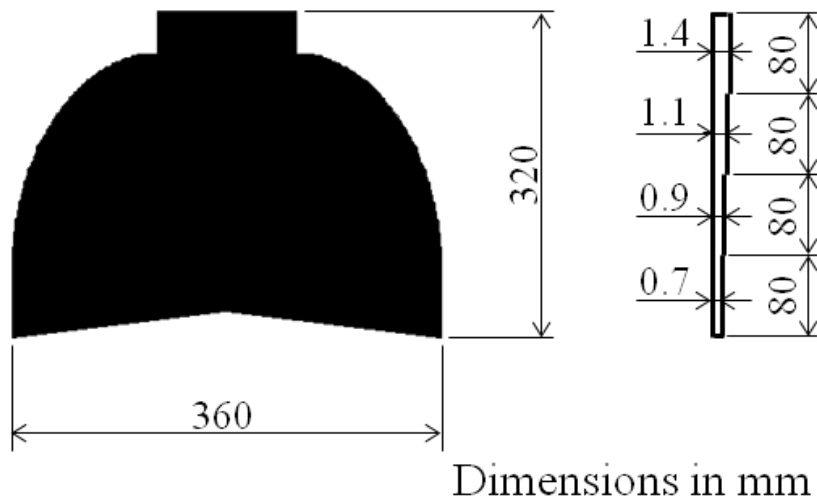


Fig. 2.3.3 Triangular airfoil dimensions (mm)



Dimensions in mm

Fig. 2.4 Monofin shape

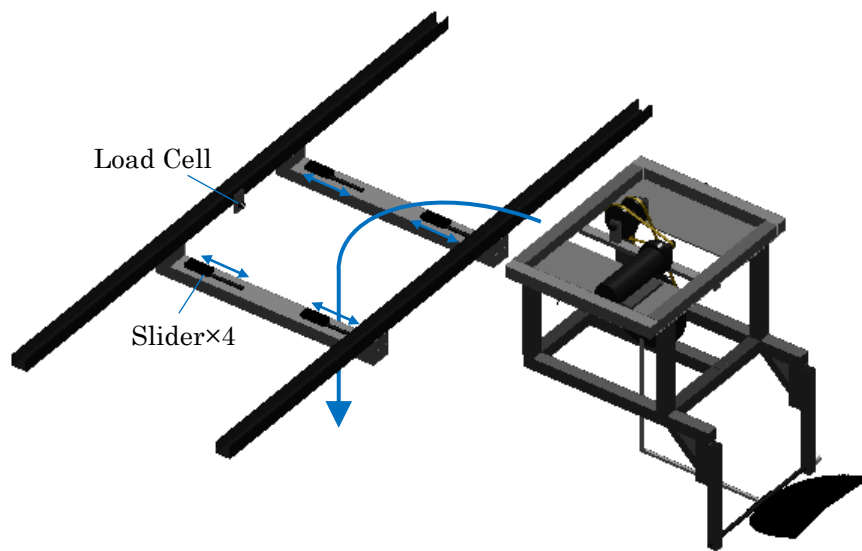
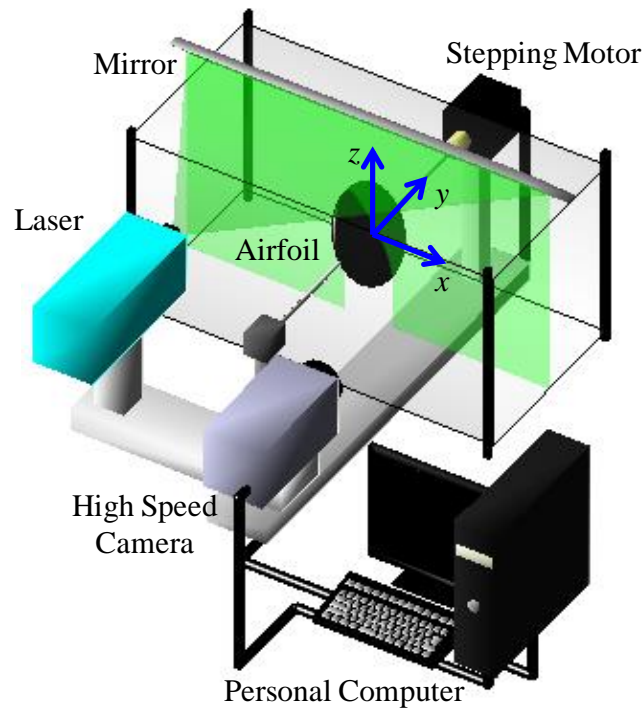
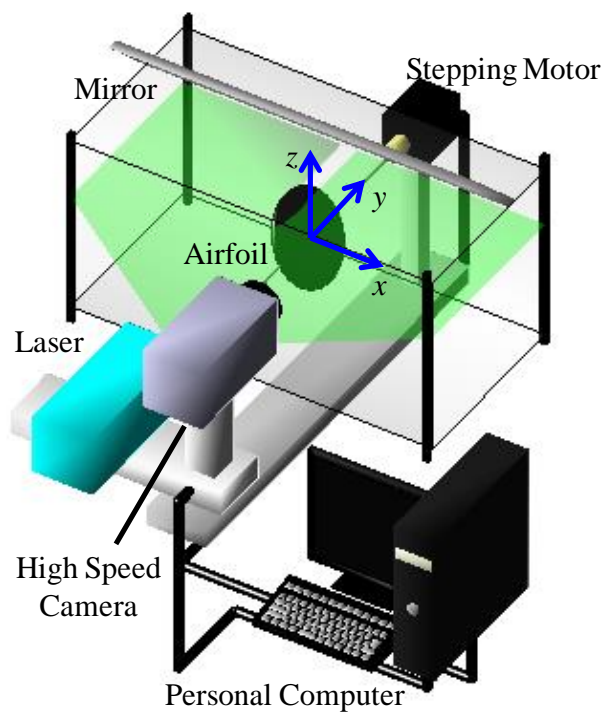


Fig. 2.5 Fluid force measurement system



(a) $x-z$ plane



(b) $x-y$ plane

Fig. 2.6 Schematic of the 2C PIV system used for the wind tunnel test

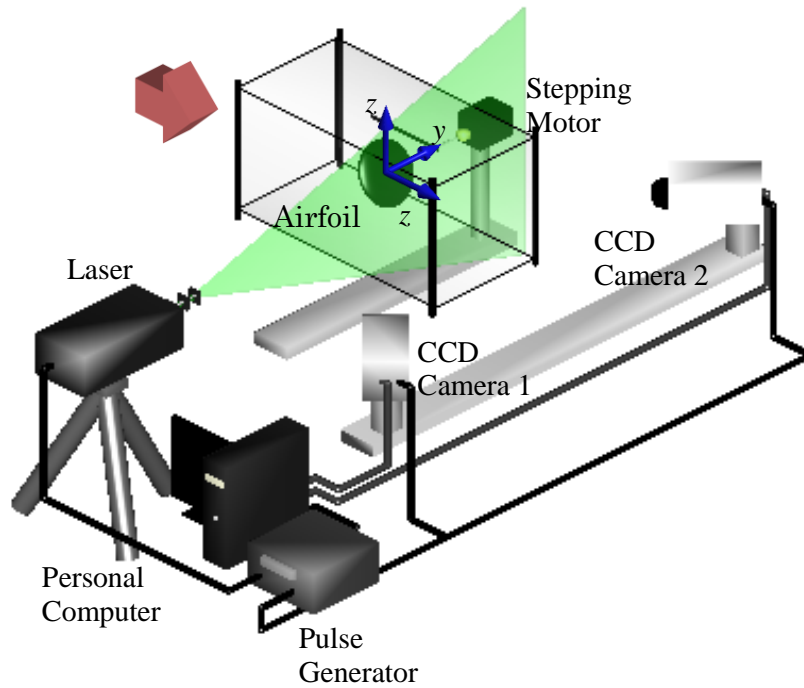


Fig. 2.7 Schematic of the Stereoscopic PIV system used for the wind tunnel test

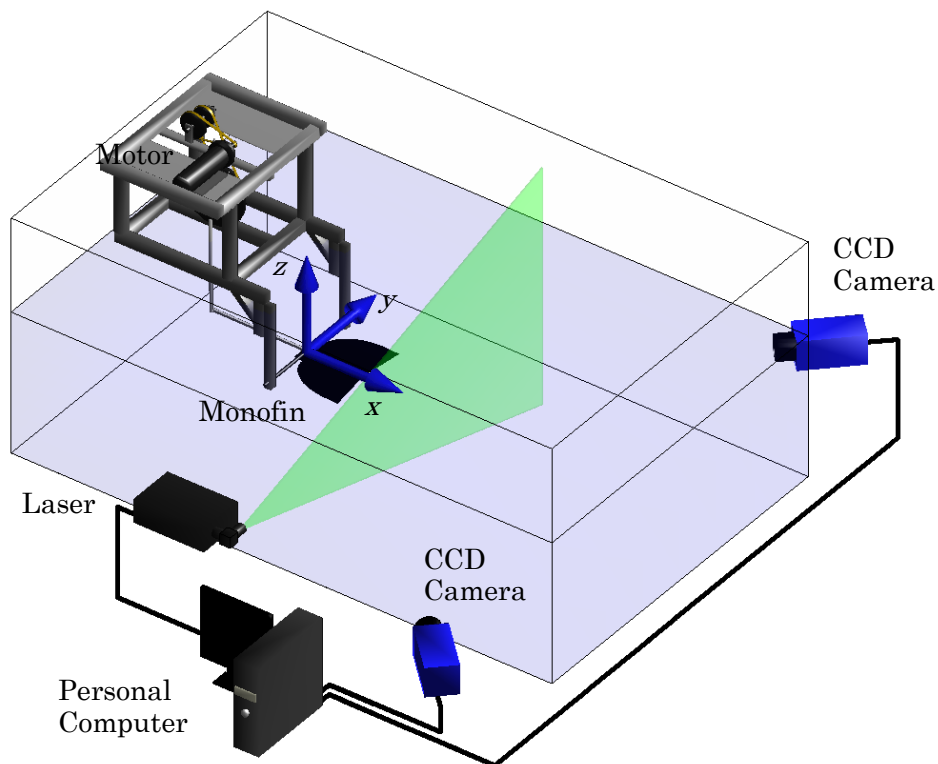
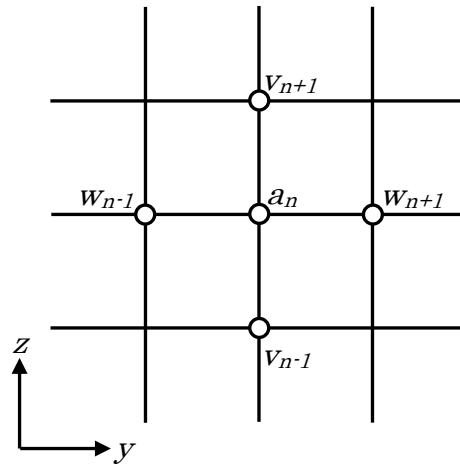
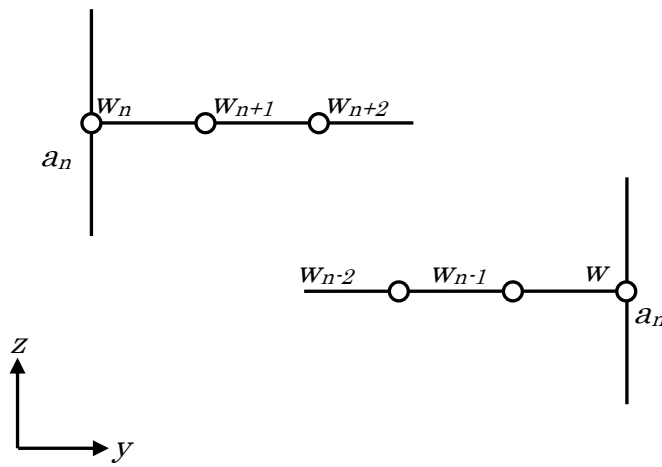


Fig. 2.8 Schematic of the Stereoscopic PIV system used for the water channel test



(a) Inside



(b) Boundary

Fig. 2.9 Computational domain

3. EFFECT OF DIFFERENT AIRFOIL SHAPES ON UNSTEADY LIFT DURING IMPULSIVE INCIDENCE VARIATION

To understand the fundamental relationship between unsteady fluid force and three-dimensional vortex structure, the angle of attack of three-dimensional airfoils was subjected impulsive incidence variation. The simple unsteady phenomenon appears close to the airfoil during the impulsive incidence variation.

3.1 Experimental method

The experiments were conducted using the wind tunnel described in Fig 2.1.1. The free-stream Reynolds number, Re , is defined as $Re = cU_0/\nu$, where c is the chord length of the airfoil, U_0 ($= 3$ m/s) is the free-stream velocity, and ν is the kinematic viscosity of the air. The test models are the discoid airfoil (with a NACA0015 profile) and the triangular airfoil, and the schematics for each airfoil are shown in Figs. 2.3.1 and 2.3.3, respectively. Figure 3.1 shows the angle of attack, α , variation of the airfoil with respect to the nondimensional time, tU_0/c , where t is the time. The degree of the airfoil movement was defined by the nondimensional rise time, $T^* (= t_a U_0/c)$, where t_a is the time period during which the airfoil angle of attack is varied. A small T^* value indicates a fast change in angle of attack during the impulsive incidence variation. The experiments were conducted at $T^* = 2$ and $T^* = 5$, and the amplitude angle, α_0 (Fig. 3.1), is 18° and 36° , respectively. The flow fields are measured using the stereoscopic PIV method. The schematic of the

stereoscopic PIV system is shown in Fig. 2.7. Figure 3.2 shows the measurement region for the stereoscopic PIV. The measurements were performed in the region from $x/c = -0.5-1.0$, at equal intervals of $x/c = 0.033$ in the $y-z$ plane. The measurement regions in the $y-z$ plane range from $y/c = -1-0$ and from $z/c = -0.7-0.7$. The velocity data on the right-hand side was interpolated using the mirror image of the velocity data on the left-hand side, because the flow field is symmetrical in the $y-z$ plane. The flow field is estimated using an ensemble averaged velocity over 10 cycles. The image of three-dimensional vortex structure is depicted by plotting the iso-Q surface.

3.2 Results and Discussion

3.2.1 Different Discoid Airfoil Motion

Figure 3.3 shows the lift curve for the discoid airfoil under stationary conditions at $Re = 3.0 \times 10^4$. The static fluid forces were measured in the region for an angle of attack, α , ranging from $0^\circ-44.64^\circ$ at equal intervals of $\alpha = 1.44^\circ$. The maximum lift coefficient, C_{Lmax} , is 0.68, and the stall angle is 24° for the discoid airfoil under stationary conditions at $Re = 3.0 \times 10^4$. Figure 3.4 shows the C_L variation during the impulsive incidence variation from $\alpha = 0^\circ$ to $\alpha = 36^\circ$ for $T^* = 2$, compared to the C_L variation under stationary conditions. In this figure, the blue line and red dotted line represent the C_L variation during the impulsive incidence variation and under stationary conditions, respectively. C_L in the stationary condition is plotted at an angle of attack that corresponds to the angle of attack during the impulsive incidence variation. C_L is calculated by ensemble averaging over 10 consecutive measurements. Fig. 3.4 shows that stall delay is observed as the angle of attack is impulsively changed, and C_L increases beyond the static stall angle. The maximum C_L for $T^* = 2$ is greater than the maximum C_L at the stationary condition. After the airfoil stop moving, C_L gradually decreases until it asymptotically approaches the C_L value achieved in the

stationary condition. Figure 3.5 shows the C_L variation for the discoid airfoil during impulsive incidence variation, when the angle of attack is varied from $\alpha = 36^\circ$ to $\alpha = 0^\circ$ for $T^* = 2$. C_L decreases as the angle of attack is decreased, and negative lift is observed before the airfoil stops moving. C_L increases after the airfoil stops moving and the lift value is positive from $tU_0/c = 3-5$. After $tU_0/c = 5$, C_L eventually coincides with its stationary value.

Figure 3.6 shows the three-dimensional vortex structure around the discoid airfoil during impulsive incidence variation from $\alpha = 0^\circ$ to $\alpha = 36^\circ$. In Fig. 3.6, the green regions show the iso-surface of the nondimensional Q invariant of the velocity gradient tensor, $Qc^2/U_0^2 = 5$. The leading edge vortex (LEV) attaches to the upper surface of the airfoil, even at angles beyond the stall angle (Fig. 3.6 (c)). Because the effective angle of attack decreases with impulsive increases in angle of attack, the tip vortex (TIV) appears at both left and right extremities of the discoid airfoil when the airfoil stops moving (Fig. 3.6 (c)). The separation on the whole upper surface of the discoid airfoil is suppressed by the TIV even after the LEV detaches from the upper surface after the airfoil stops moving. Figures 3.7 and 3.8 show the three-dimensional vortex structure of ω_y and ω_x for the discoid airfoil to illustrate the behavior of the LEV and the TIV around the discoid airfoil, respectively. The LEV attaches to the upper surface of the airfoil just after the airfoil stops moving. The attached LEV region decreases in the spanwise direction over time. The TIV appears near the trailing edge at $tU_0/c = 2$. Immediately after the airfoil stops moving, a strong TIV exists in the wake of the airfoil (Figs. 3.8 (c)). The TIV moves toward the center axis of the airfoil because of the curvature of the discoid airfoil (Figs. 3.8 (e) and (e)). The TIV becomes weaker over time and the flow on the upper surface detaches gradually. For the two-dimensional airfoil, it was reported that C_L rapidly decreases after the airfoil stops moving. This occurs during impulsive incidence variation from 0° to the angle set beyond the static stall angle for small values of nondimensional rise time (Aihara et al. (1985) [33]). On the other hand, for the discoid airfoil, C_L gradually decreases after the airfoil

stops moving. This occurs because C_L variation is affected by the TIV behavior after the airfoil stops moving.

Figure 3.9 shows the three-dimensional vortex structure for the discoid airfoil during impulsive incidence variation from $\alpha = 36^\circ$ to $\alpha = 0^\circ$. The LEV is successively shed from the leading edge of the airfoil and the flow on the upper surface detaches even at the angles below the stall angle (Fig. 3.9 (b)). This occurs because the effective angle of attack is increased as the angle of attack is impulsively decreased. The airfoil remains in a stalled state and C_L is less than it is at the stationary condition just after the airfoil stops moving. After the airfoil stops moving, C_L increases as the flow gradually attaches to the upper surface of the airfoil (Fig. 3.10 which shows the two-dimensional vortex structure in the $x-z$ plane at $y/c = 0$). Furthermore, positive lift is produced because the LEV attaches to the upper surface of the airfoil (Fig. 3.10 (b)). Subsequently, the flow field and C_L eventually coincide with their stationary values.

3.2.2 Different Airfoil Shapes

Figure 3.11 shows the lift curve for the triangular airfoil under stationary conditions at $Re = 3.0 \times 10^4$. The maximum lift coefficient, C_{Lmax} , is 0.75 and the stall angle is 33° . Figures 3.12 and 3.13 show the C_L variation for the triangular airfoil during the impulsive incidence variation from $\alpha = 0^\circ$ to $\alpha = 18^\circ$, and from $\alpha = 0^\circ$ to $\alpha = 36^\circ$, respectively. In all cases involving the triangular airfoil (similar to the discoid airfoil (Hasegawa et al. (2014) [34])), C_{Lmax} is greater during impulsive incidence variation than at the stationary condition, and it increases with the increasing amplitude angle, α_0 , and with decreasing nondimensional rise time, T^* . From $\alpha = 0^\circ$ to $\alpha = 36^\circ$ (Fig. 3.13), stall delay is observed. C_{Lmax} (= 1.08) for the triangular airfoil at $T^* = 2$ and $\alpha_0 = 36^\circ$ (Fig. 3.13 (b)) is approximately equivalent to the discoid airfoil, but the difference between C_{Lmax} under stationary and unsteady conditions is smaller than it is for the discoid airfoil. In contrast to the discoid airfoil, C_L

decreases rapidly just after the airfoil stops moving. At $tU_0/c = 15$, C_L during the impulsive incidence variation under reaches stationary values.

Figure 3.14 shows the three-dimensional vortex structure around the triangular airfoil during impulsive incidence variation from $\alpha = 0^\circ$ to $\alpha = 36^\circ$ for $T^* = 2$. Figures 3.15 and 3.16 show the three-dimensional vortex structure of ω_y and ω_x for the triangular airfoil to illustrate the behavior of the LEV and the TIV around the triangular airfoil, respectively. The starting vortex (SV) grows near the trailing edge as the angle of attack increases. Therefore, the circulation around the airfoil is augmented and the lift increases. The LEVs are formed on the upper surface along the right and left leading edges of the triangular airfoil just before the airfoil stops moving (Fig. 3.14 (b)). After the airfoil stops, the detached point of the LEV moves from the trailing edge toward the leading edge as time passes (Fig. 3.14 (c)-(f) right column and Fig. 3.16 (c)-(f)). The nondimensional time at which the flow field reaches a stationary condition is smaller than that for the discoid airfoil. As a result, the lift decreases abruptly after the triangular airfoil stops moving. Because the fundamental vortex structure after the triangular airfoil stops moving is similar to that of the stationary condition. On the other hand, the separation on whole upper surface of the discoid airfoil is suppressed by the noticeably strong TIV, which was not observed under stationary condition. In addition, the effect of impulsive incidence variation (unsteady effect) on the LEV for the triangular airfoil is relatively small because strong LEVs were generated under stationary conditions, even at the angles greater than the stall angle. Therefore, the unsteady effect on the unsteady force and the flow field during impulsive incidence variation for the discoid airfoil is greater than that for the triangular airfoil.

3.3 Conclusions

To understand the fundamental relationship between unsteady fluid force and three-dimensional vortex structure, upward and downward airfoil

movements are performed and the angle of attack of the airfoil is impulsively changed between 0° – 36° . In addition, two types of airfoils were used. The results of the experiment are summarized as follows:

1. Stall delay is observed when the discoid airfoil is motioned upward, and the maximum lift coefficient is greater than at the stationary condition. C_L gradually decreases after the airfoil stops, and the value of C_L asymptotically approaches that of the stationary condition. C_L variation is affected by the TIV behavior after the airfoil stops moving for upward motions.
2. When the discoid airfoil is motioned downward, C_L decreases as the angle of attack decreases, and negative lift is observed before the airfoil stops moving. The flow on the upper surface detaches even at angles below the stall angle. C_L increases as the flow gradually attaches to the upper surface of the airfoil after it stops moving.
3. In contrast to the discoid airfoil, C_L decreases rapidly for the triangular airfoil immediately after it stops moving. The nondimensional time at which the flow field reaches a stationary condition is smaller than that for the discoid airfoil. The unsteady effect on the unsteady lift and the flow field during impulsive incidence variation for the discoid airfoil is greater than that for the triangular airfoil.

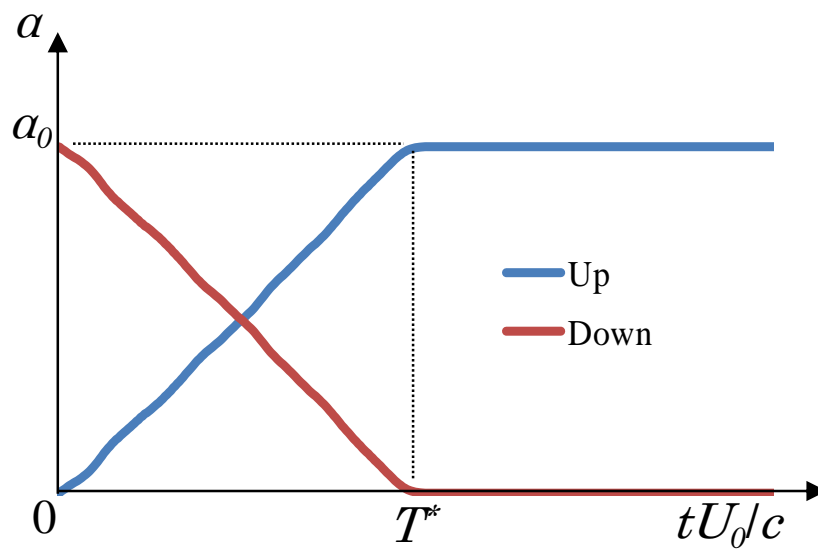


Fig. 3.1 The temporal change in angle of attack

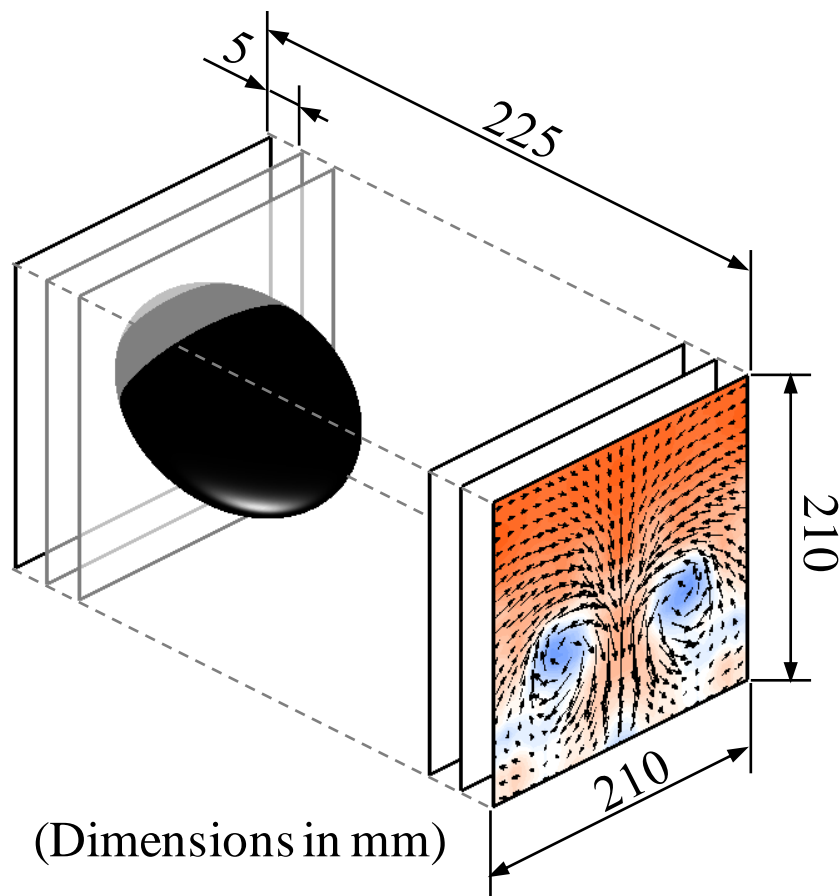


Fig. 3.2 The measuring region for stereoscopic PIV for impulsive incidence variation

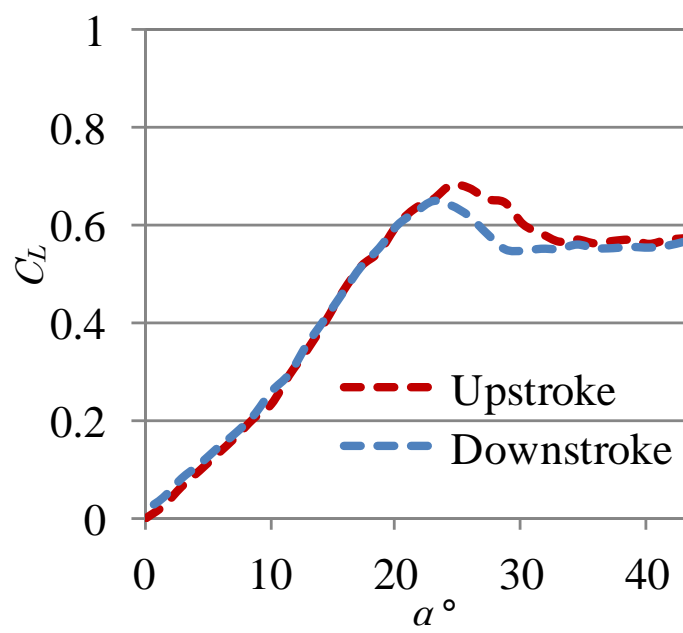


Fig. 3.3 Lift curve for the discoid airfoil in the stationary condition

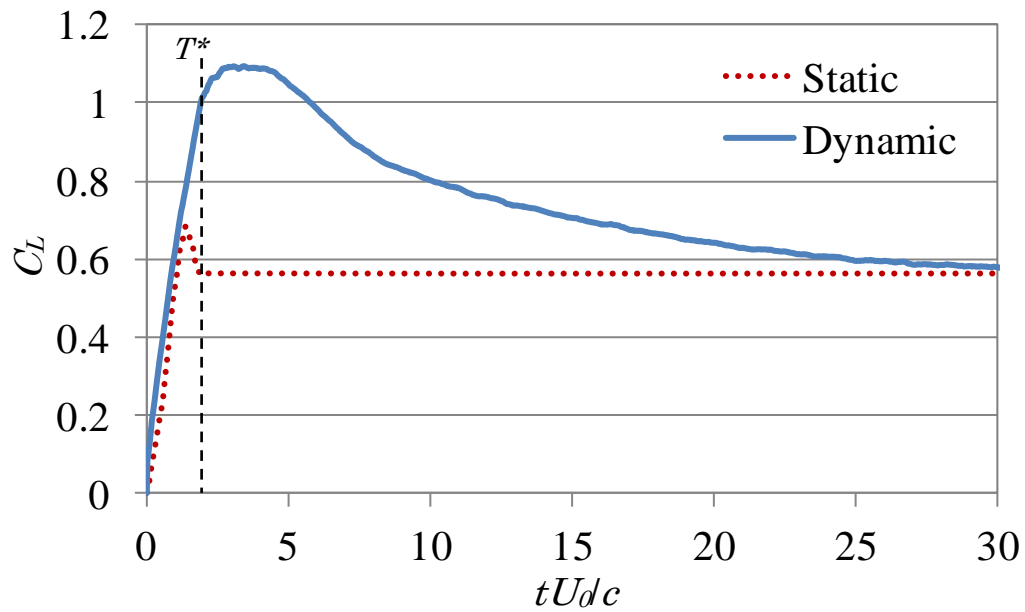


Fig. 3.4 Lift curve for the discoid airfoil as it is impulsively changed from 0° – 36° at $T^* = 2.0$

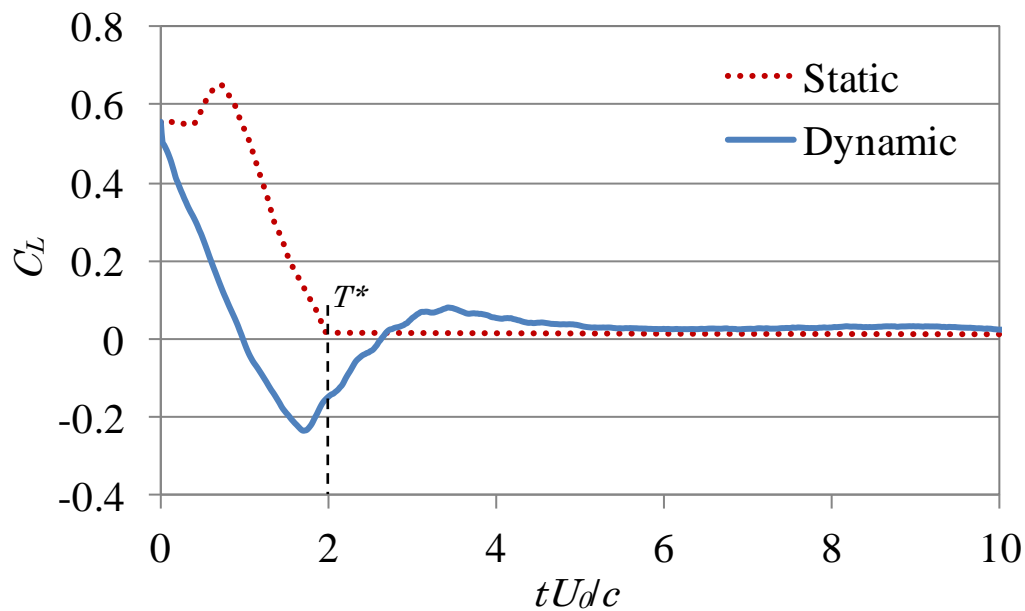
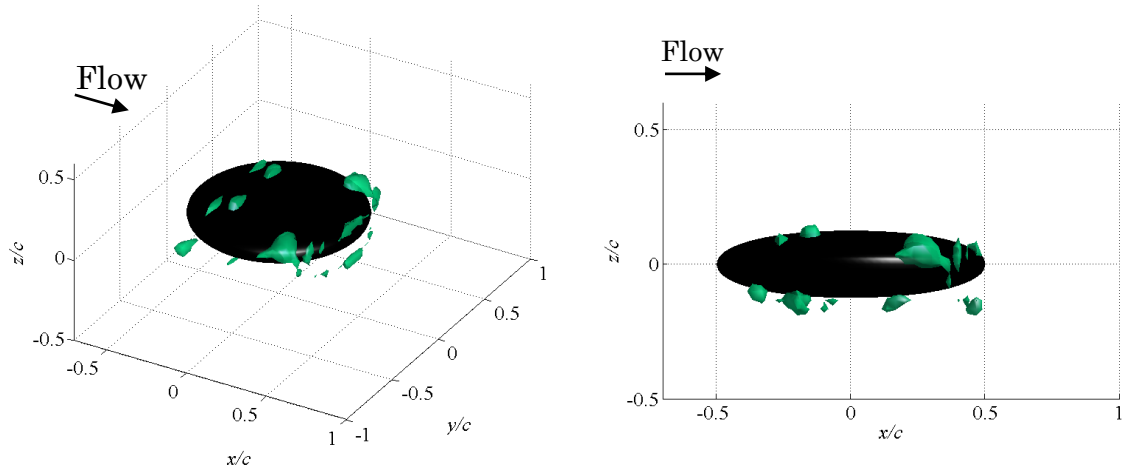
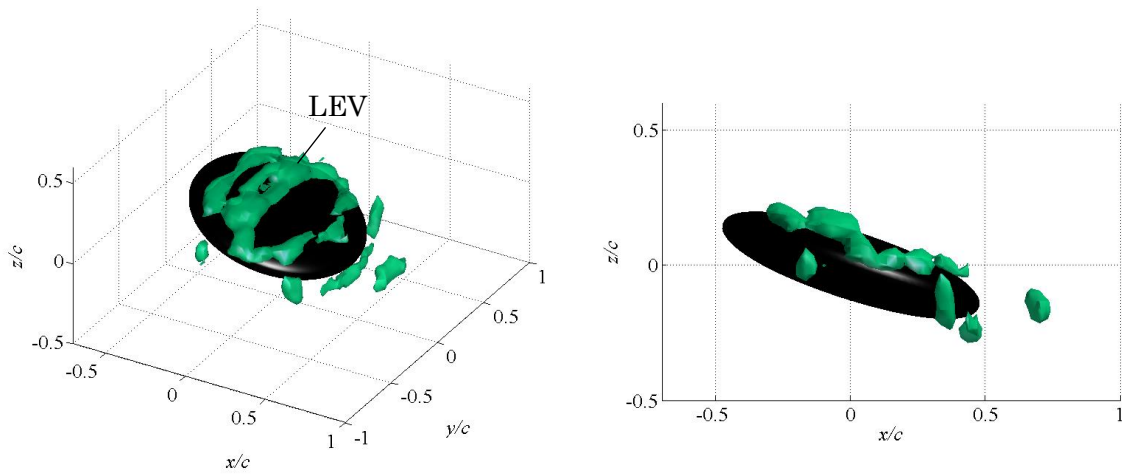
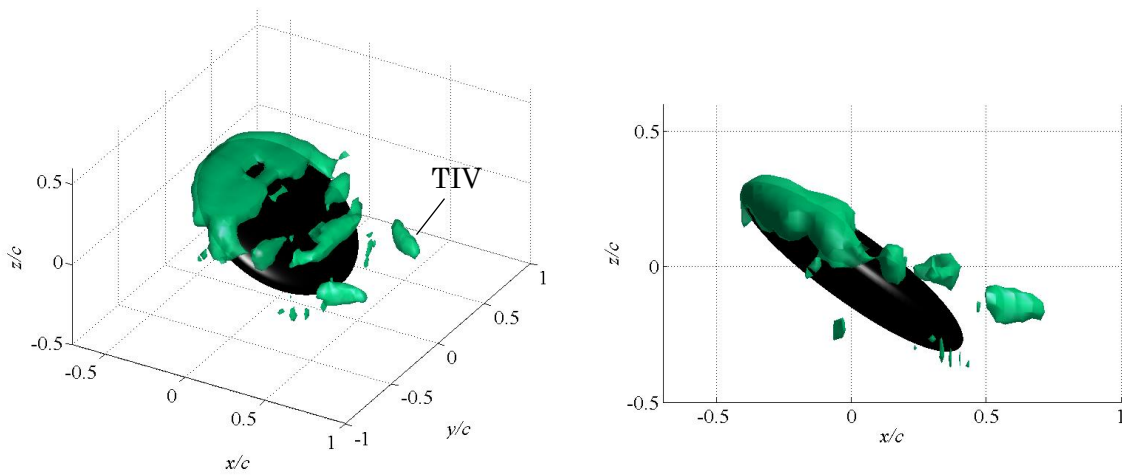
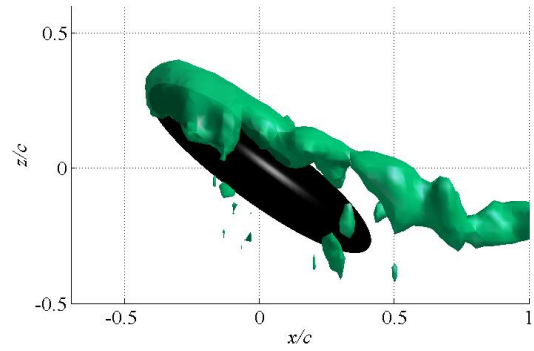
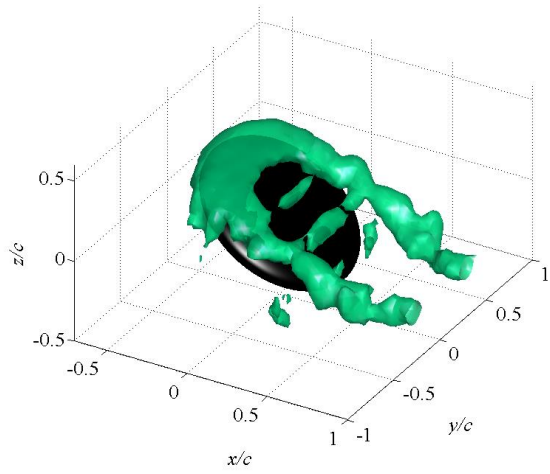
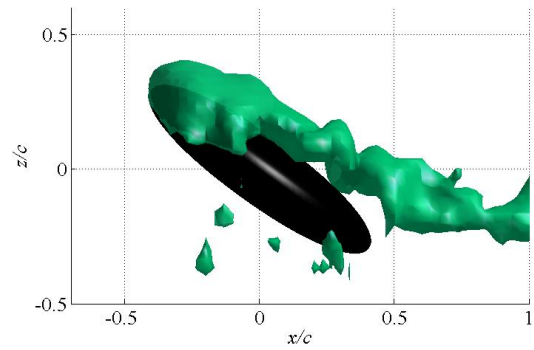
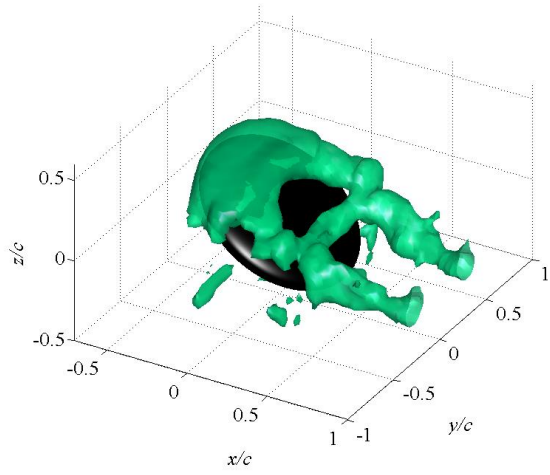
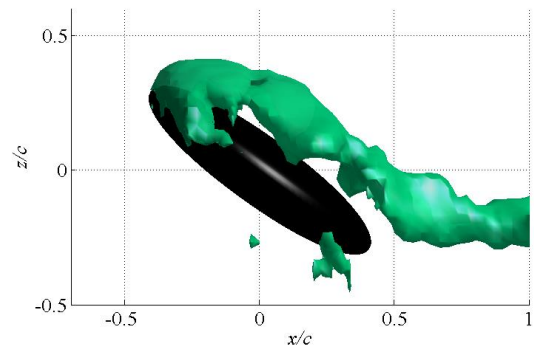
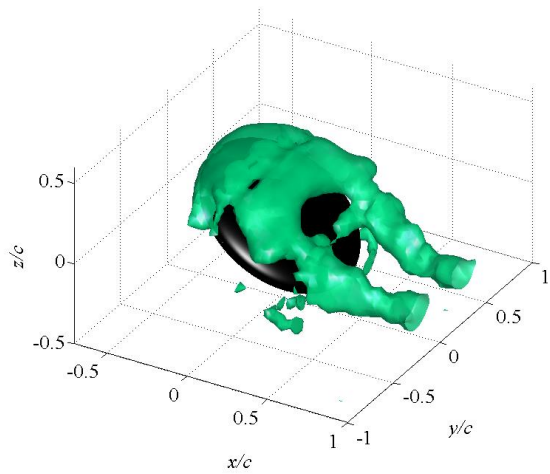


Fig. 3.5 Lift curve for the discoid airfoil as it is impulsively changed from 36° – 0° at $T^* = 2.0$

$$Qc^2/U\sigma^2 = 5$$

(a) $tUd/c = 0$ (b) $tUd/c = 1$ (c) $tUd/c = 2$

(d) $tUd/c = 3$ (e) $tUd/c = 5$ (f) $tUd/c = 7$

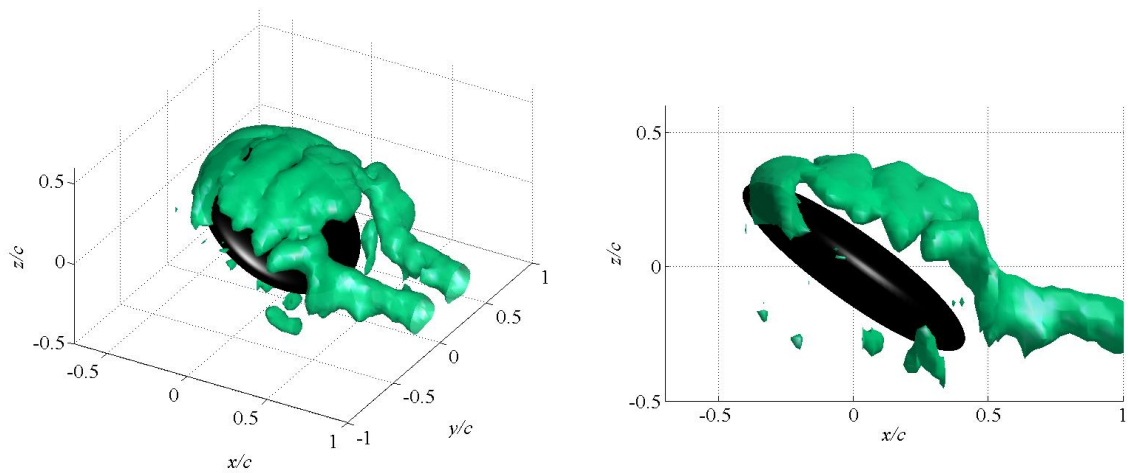
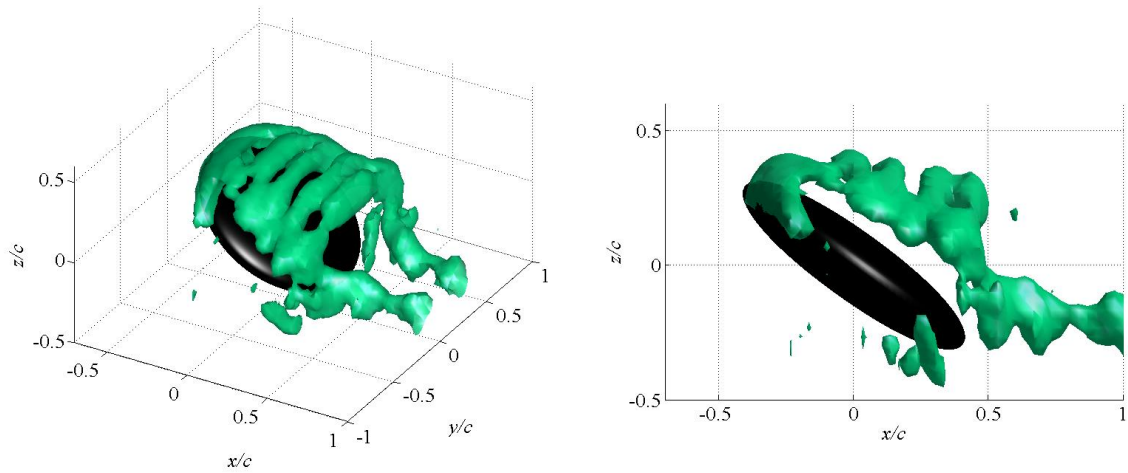
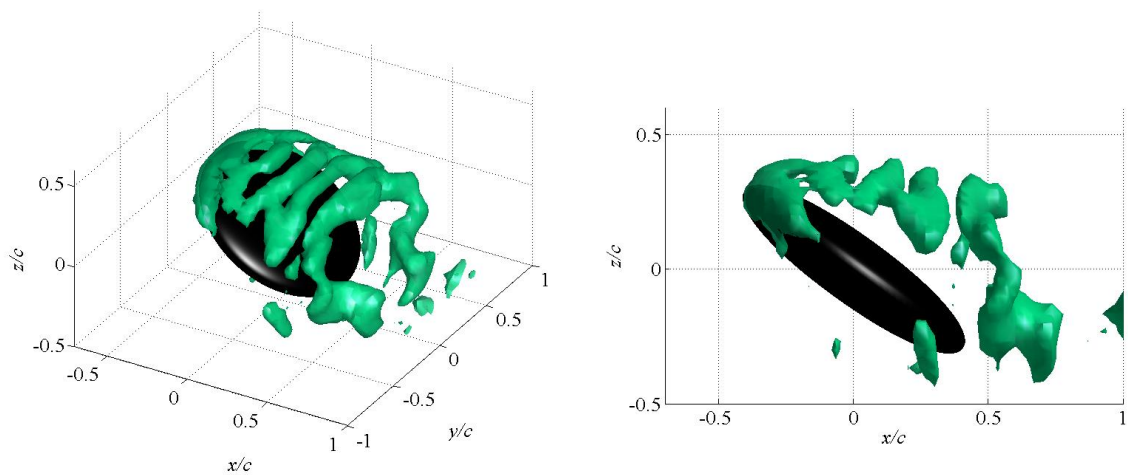
(g) $tU_d/c = 12$ (h) $tU_d/c = 20$ (i) $tU_d/c = 30$

Fig. 3.6 Three-dimensional vortex structure for the discoid airfoil as it is impulsively changed from 0° – 36° for $T^* = 2.0$

$$\omega_y c / U_0 = -5$$

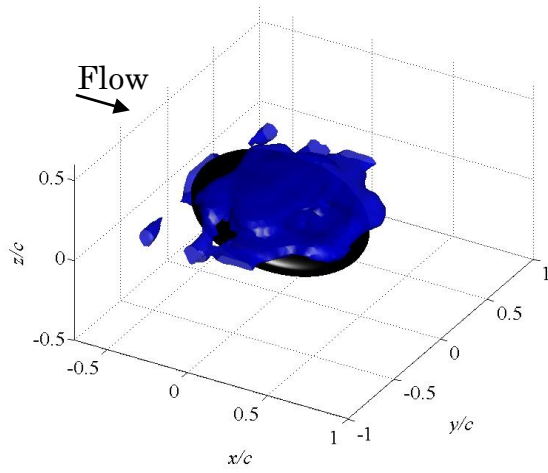
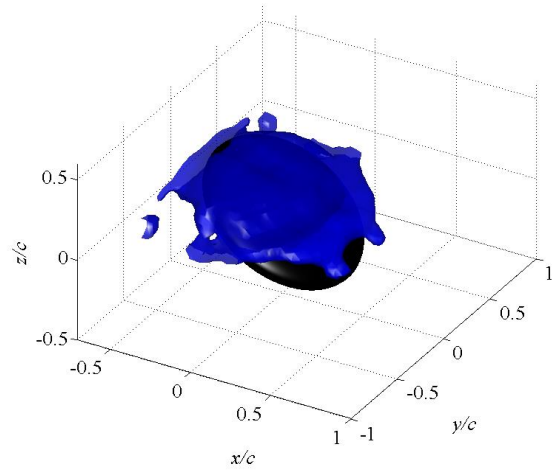
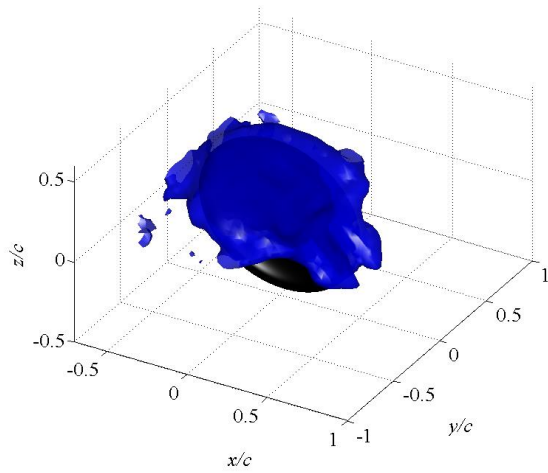
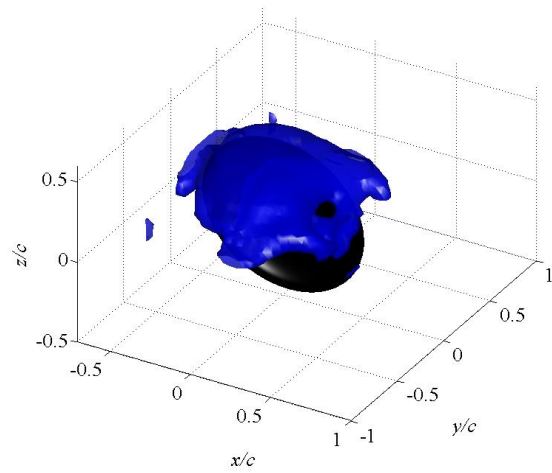
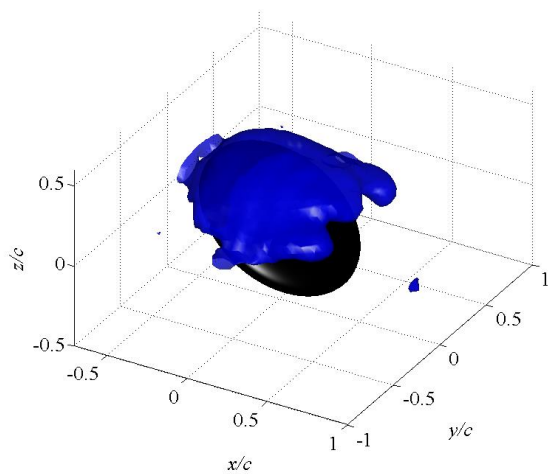
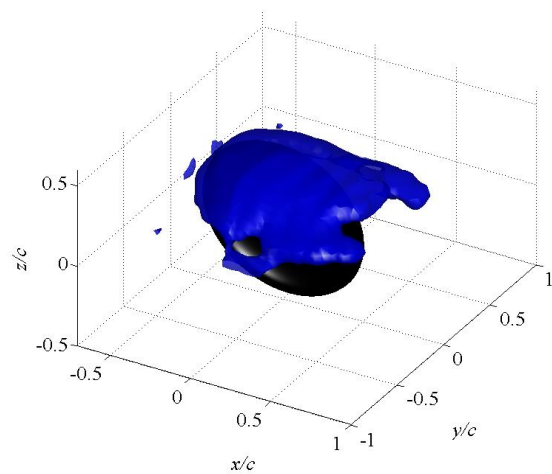
(a) $tU_d/c = 1$ (b) $tU_d/c = 2$ (c) $tU_d/c = 3$ (d) $tU_d/c = 7$ (e) $tU_d/c = 12$ (f) $tU_d/c = 30$

Fig. 3.7 Three-dimensional vortex structure of ω_y for the discoid airfoil as it is impulsively changed from 0° – 36° for $T^* = 2.0$

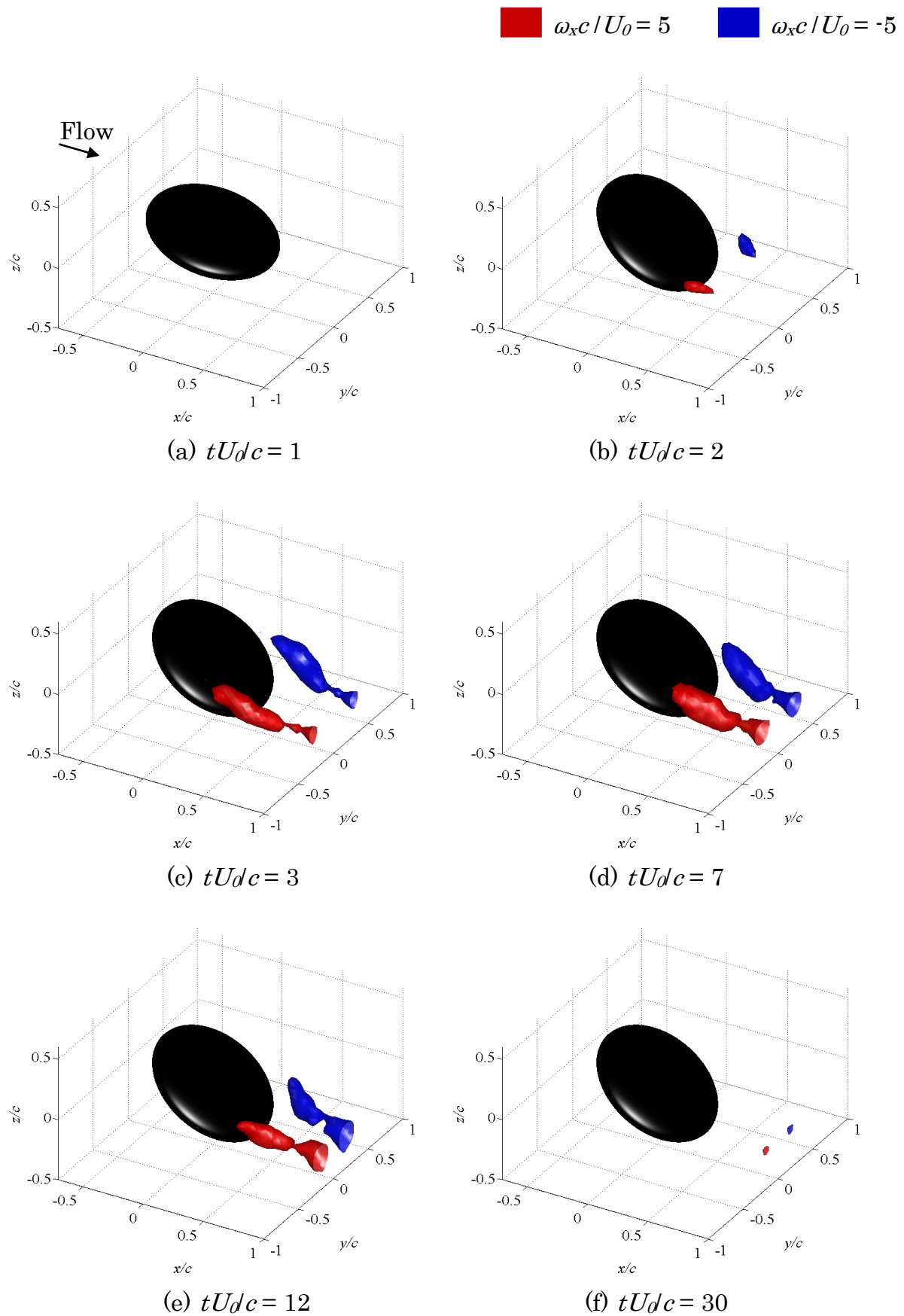
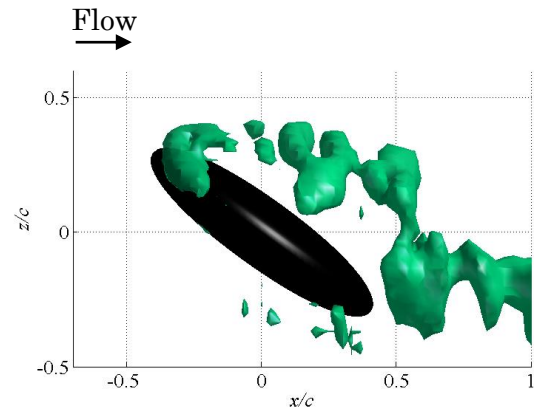
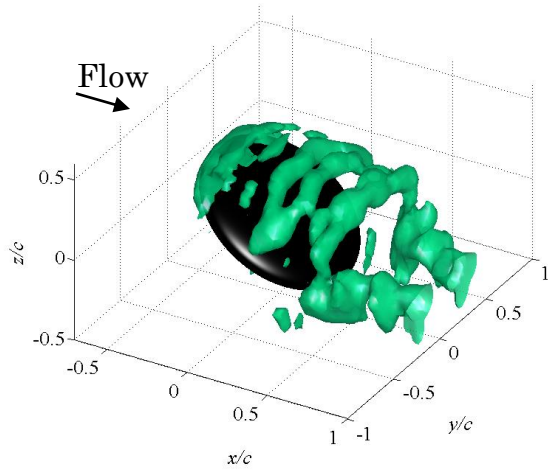
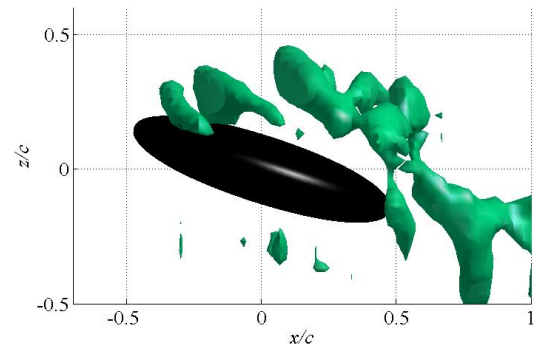
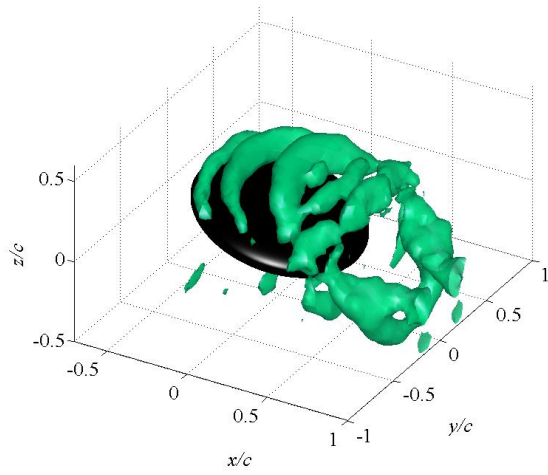
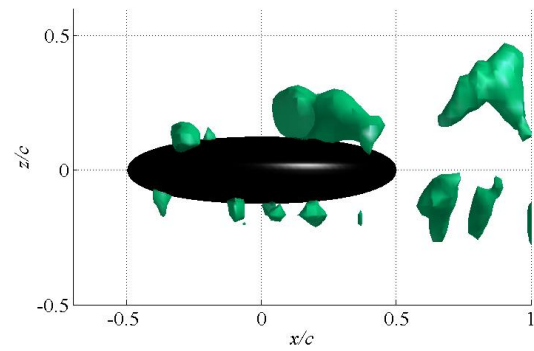
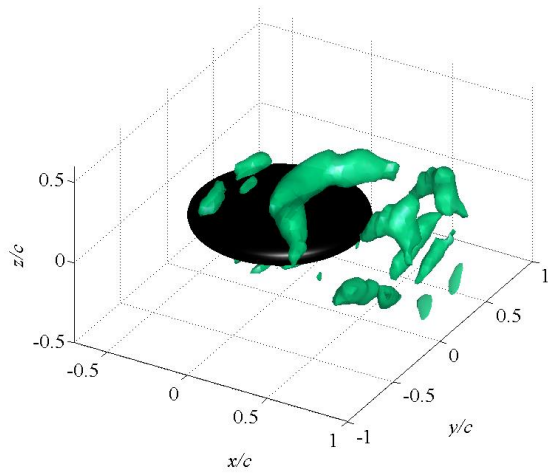


Fig. 3.8 Three-dimensional vortex structure of ω_x for the discoid airfoil as it is impulsively changed from 0° – 36° for $T^* = 2.0$

$$Qc^2/U\sigma^2 = 5$$

(a) $tUd/c = 0$ (b) $tUd/c = 1$ (c) $tUd/c = 2$

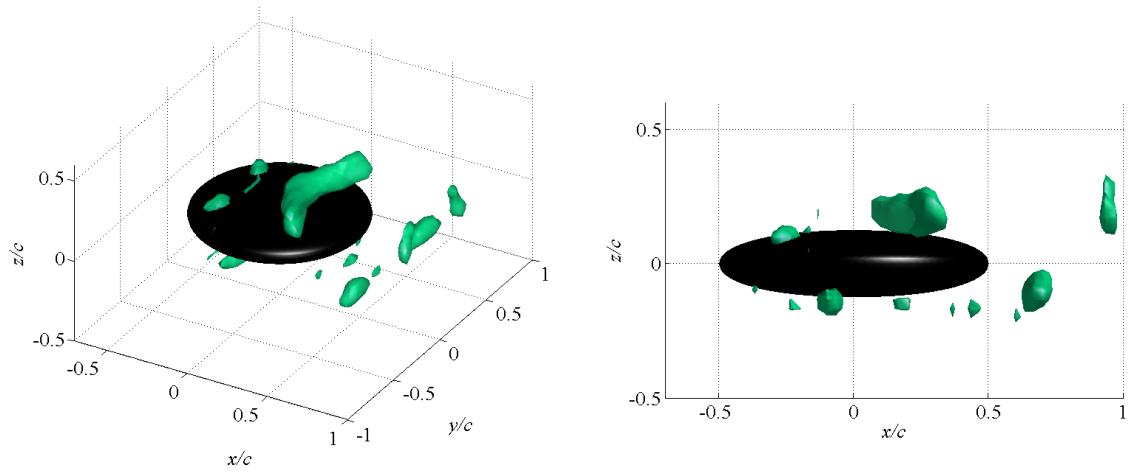
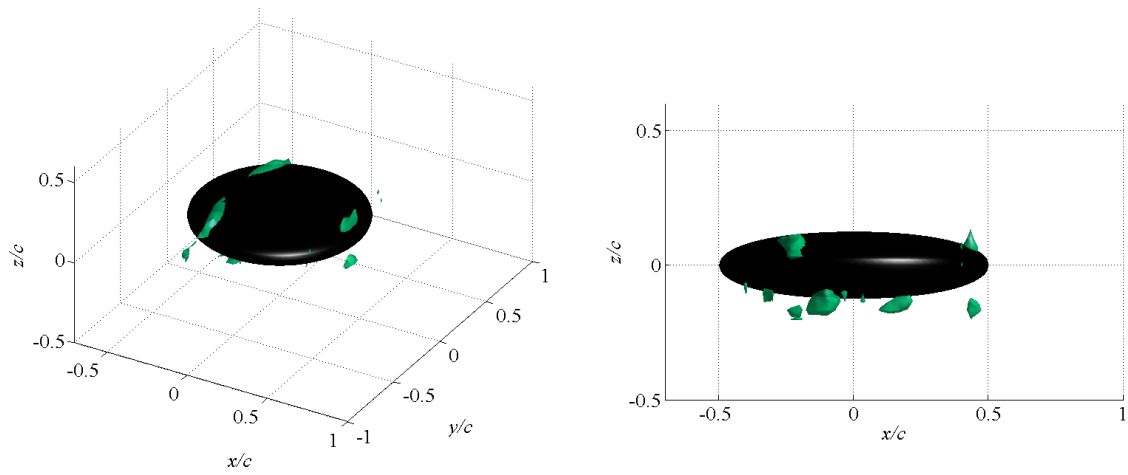
(d) $tUd/c = 3$ (e) $tUd/c = 5$

Fig. 3.9 Three-dimensional vortex structure for the discoid airfoil as it is impulsively changed from 36° – 0° for $T^* = 2.0$

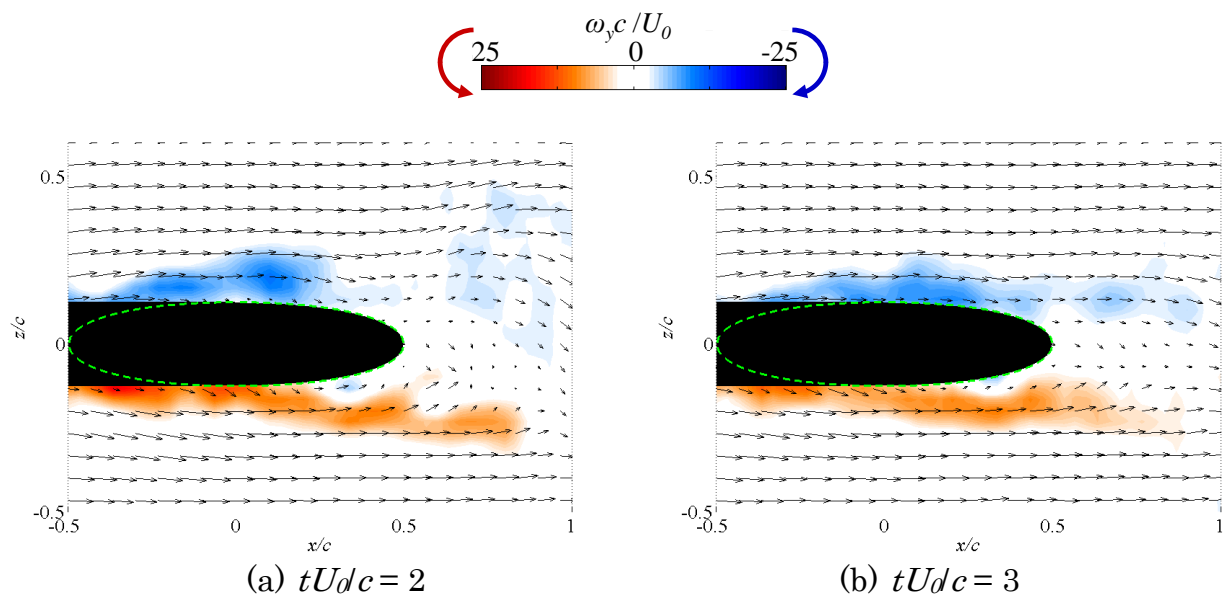


Fig. 3.10 Density map of vorticity in the x - z plane for the discoid airfoil as it is impulsively changed from 36° - 0° for $T^* = 2.0$

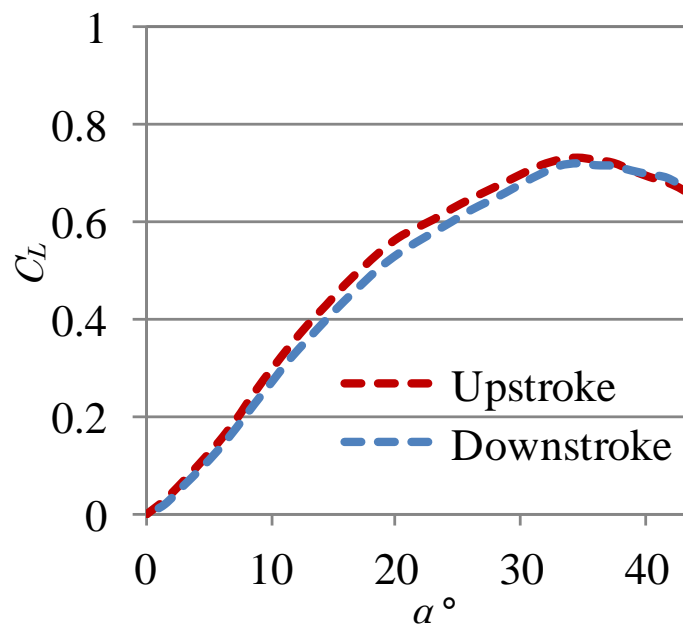
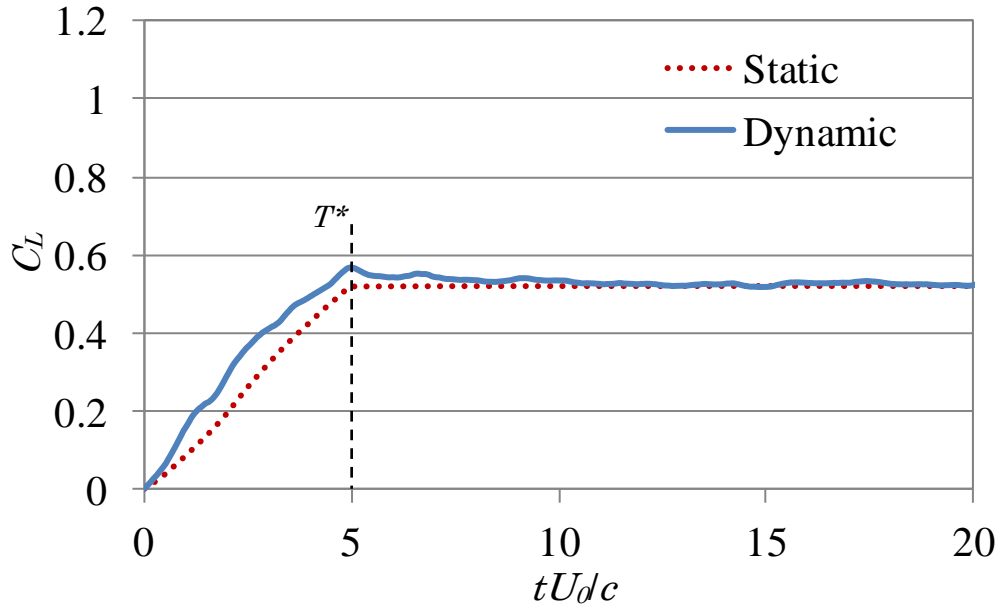
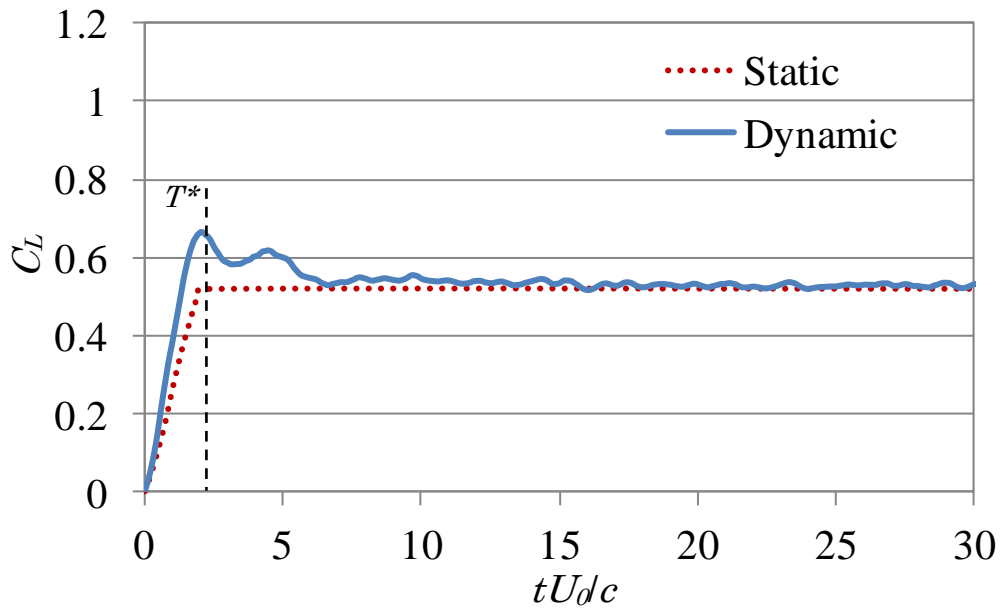
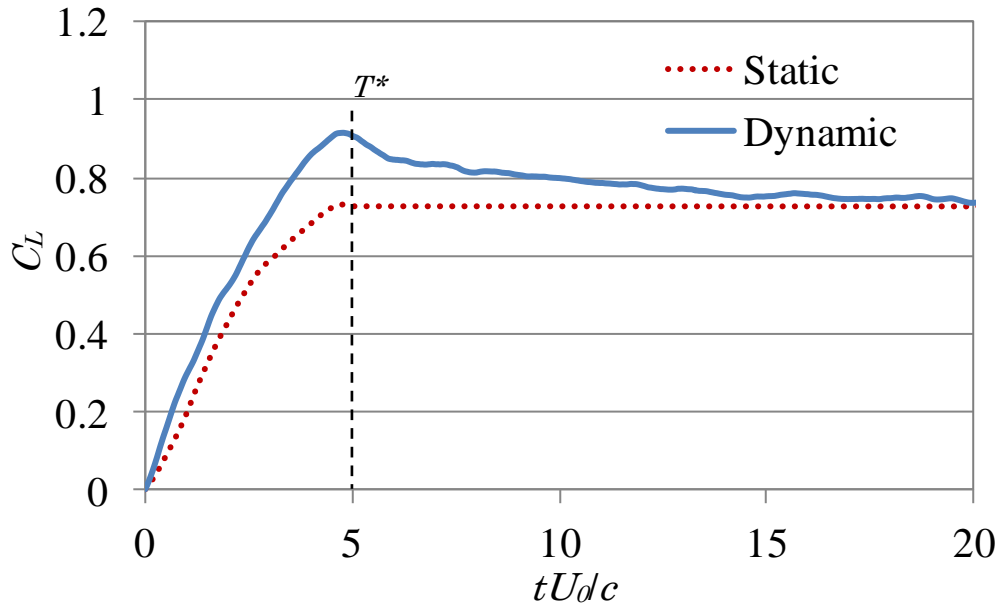
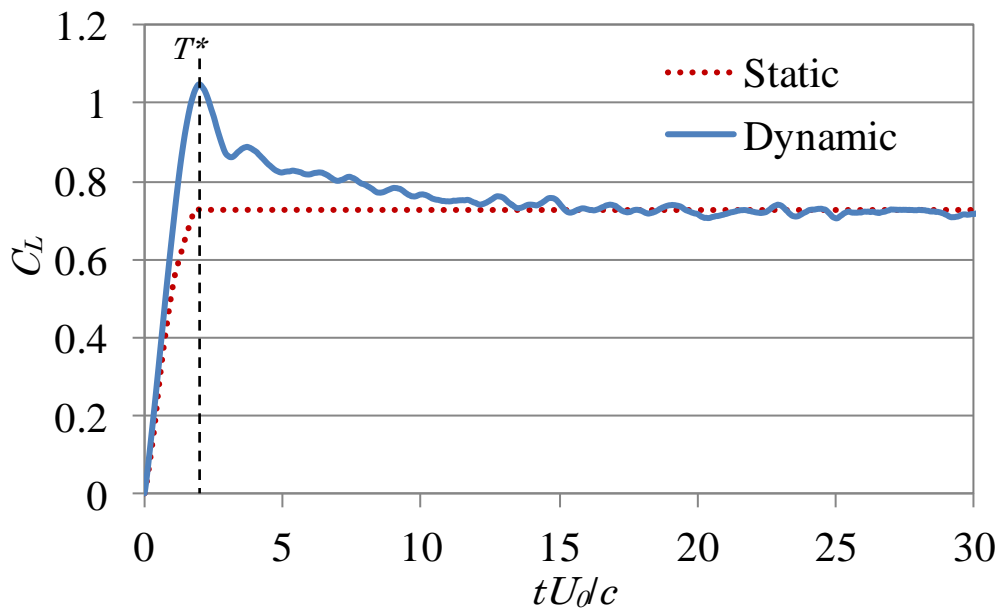
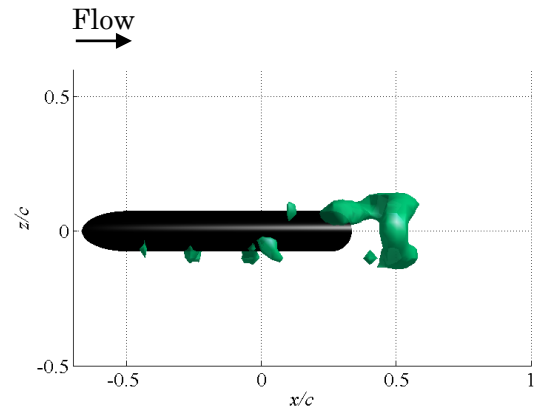
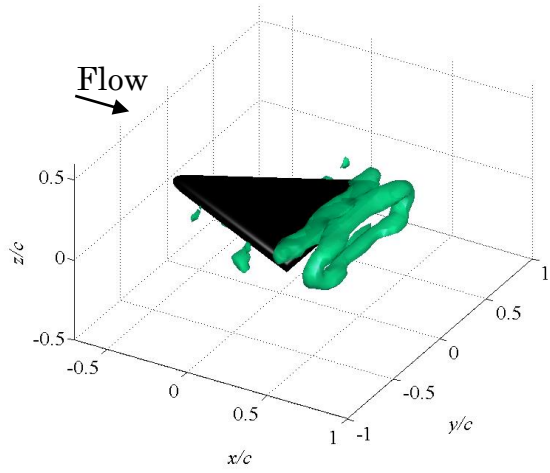
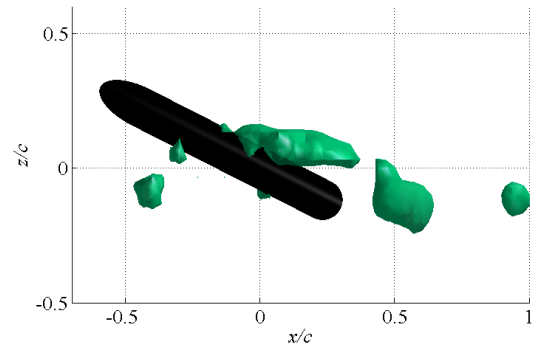
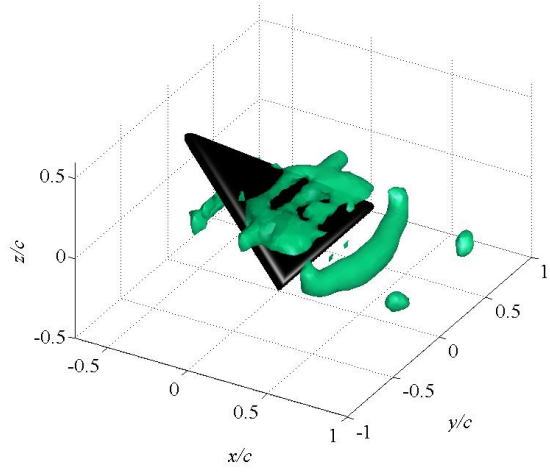
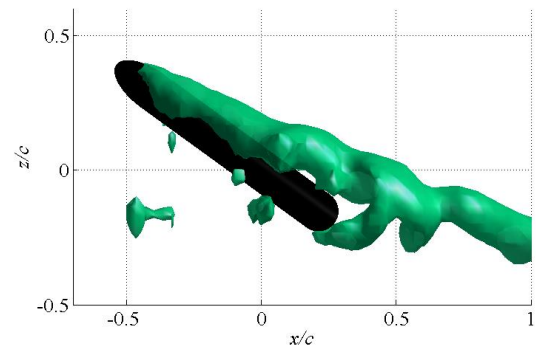
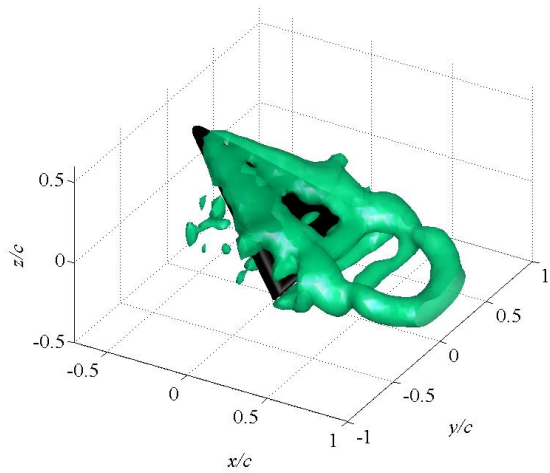


Fig. 3.11 Lift curve for the triangular airfoil in the stationary condition

(a) $T^* = 5$ (b) $T^* = 2$ Fig. 3.12 Lift curve for the triangular airfoil as it is impulsively changed from 0° – 18°

(a) $T^* = 5$ (b) $T^* = 2$ Fig. 3.13 Lift curve for the triangular airfoil as it is impulsively changed from 0° – 36°

$$Qc^2/U\sigma^2 = 5$$

(a) $tUd/c = 0$ (b) $tUd/c = 1.5$ (c) $tUd/c = 2$

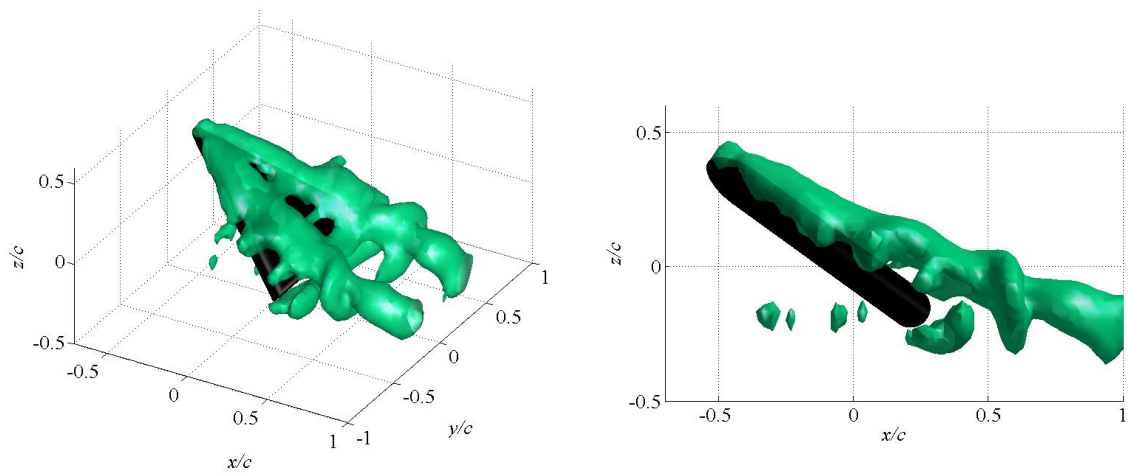
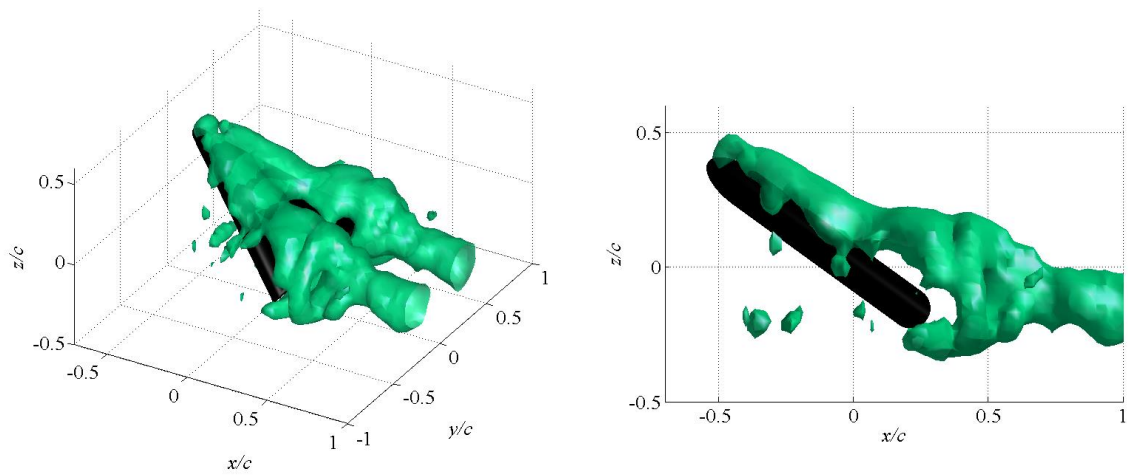
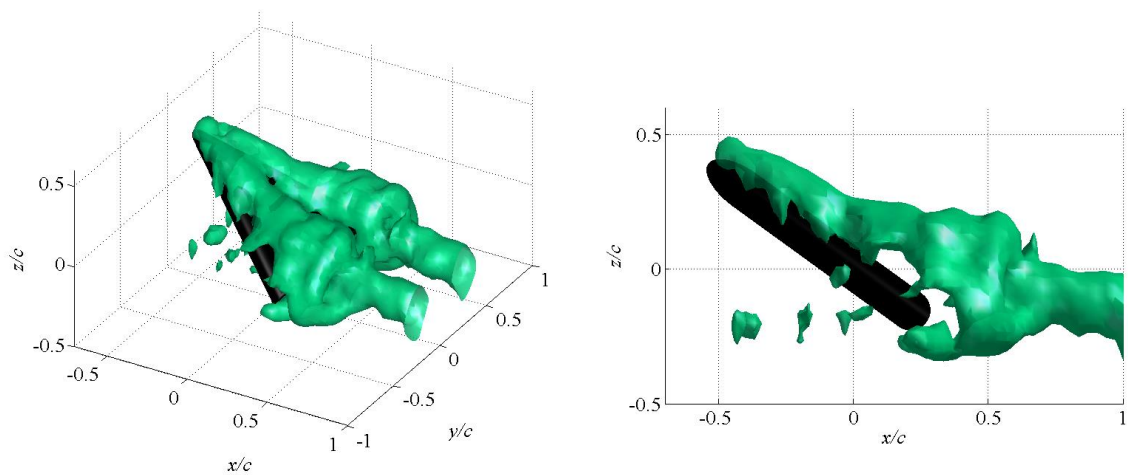
(d) $tUd/c = 3$ (e) $tUd/c = 7$ (f) $tUd/c = 15$

Fig. 3.14 Three-dimensional vortex structure for the triangular airfoil as it is impulsively changed from 0° – 36° for $T^* = 2.0$

$$\omega_y c / U_0 = 5$$

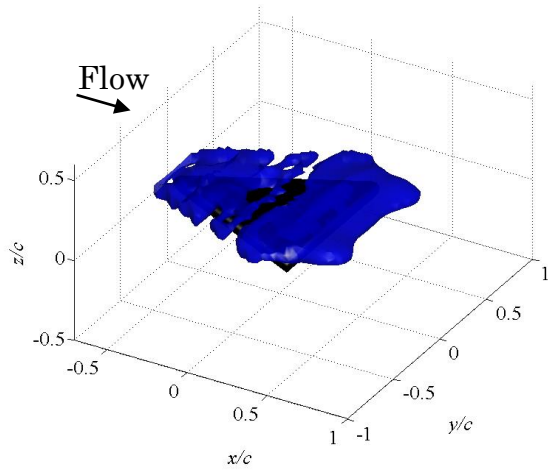
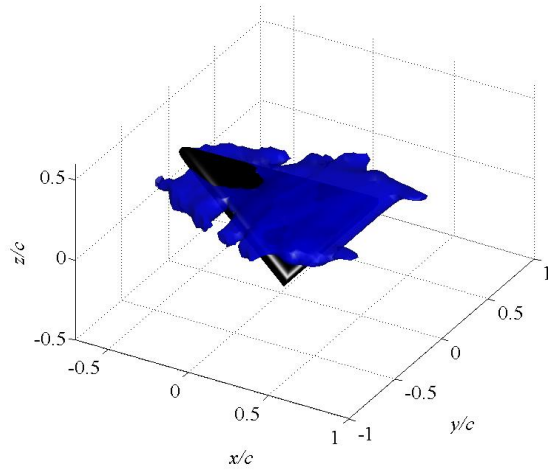
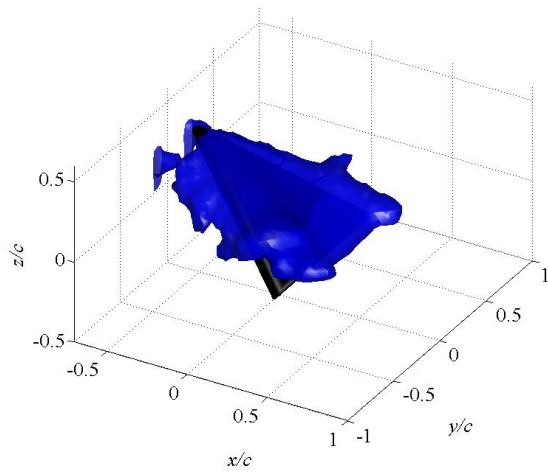
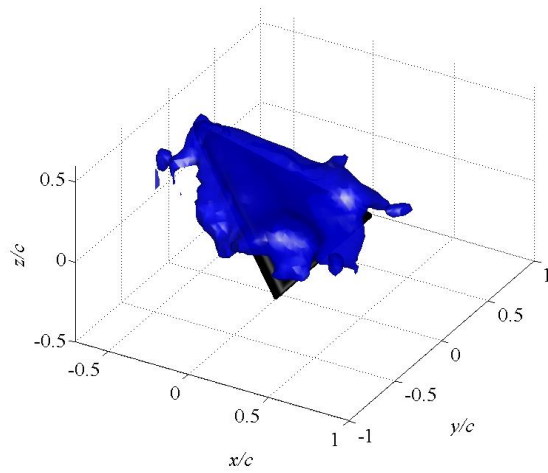
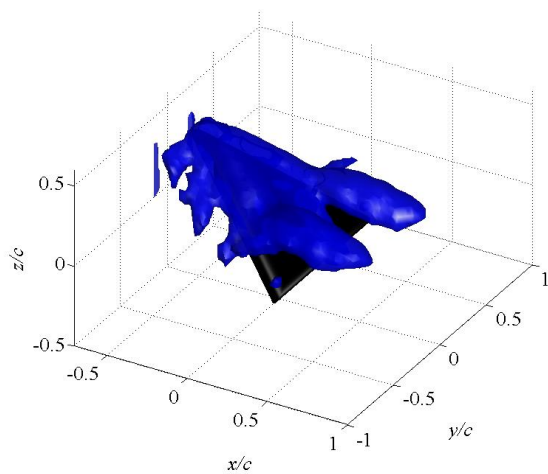
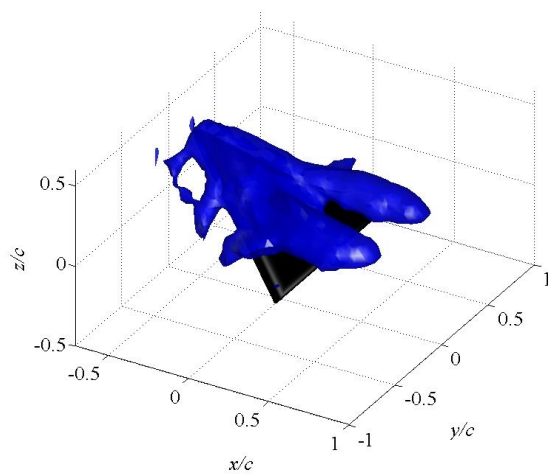
(a) $tU_d/c = 0$ (b) $tU_d/c = 1$ (c) $tU_d/c = 2$ (d) $tU_d/c = 3$ (e) $tU_d/c = 7$ (f) $tU_d/c = 15$

Fig. 3.15 Three-dimensional vortex structure of ω_y for the triangular airfoil as it is impulsively changed from 0° – 36° for $T^* = 2.0$

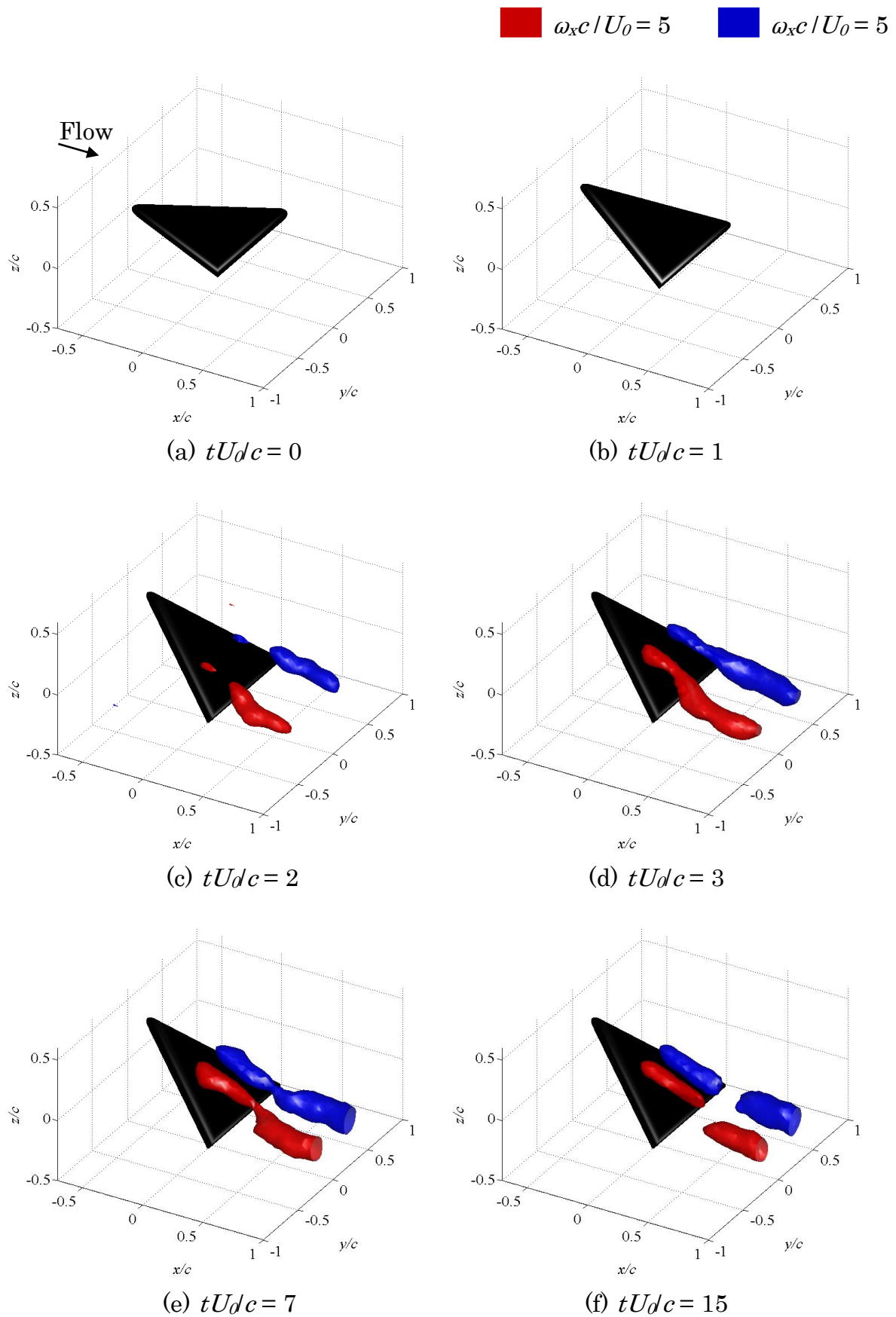


Fig. 3.16 Three-dimensional vortex structure of ω_x for the triangular airfoil as it is impulsively changed from 0° – 36° for $T^* = 2.0$

4. VORTEX STRUCTURE AROUND DISCOID AIRFOIL DURING PITCH-OSCILLATING MOTION

To investigate the effect of oscillating motion on vortex generation, two types of pitch-oscillating motion around the oscillating 90° center angle (the leading edge of the airfoil displaces the trailing edge during one cycle of oscillation) are conducted as the angular speed is changed.

4.1 Experimental method

Experiments were carried out using the wind tunnel described in Fig 2.1.1. The experiments described here were performed using $Re = 3.0 \times 10^4$, which corresponds to the Reynolds number range for the hand of a swimmer. The test model is the discoid airfoil shown in Fig. 2.3.1. To investigate the effect of angular velocity on vortex structures during one cycle of pitching motion, two types of airfoil oscillations were performed. In the following analysis, the nondimensional time, t' is defined as $t' = t/T$, where T is the total time of one cycle of oscillation, and t is the time. Figure 4.1 shows the angle of attack of the airfoil model with respect to nondimensional time. For the standard oscillation case (Type-1), the variation in angle of attack follows that of a sinusoidal curve. The angle of attack of the model varies according to the equation

$$\alpha = \alpha_c + a_0 \sin(2\pi t'), \quad (4.1)$$

where a_0 is the amplitude, f is the oscillation frequency, and α_c is the angle of the pitching center. The airfoil model moves slowly at the beginning of the

downstroke and upstroke, at $t' = 0-0.25$ and $0.5-0.75$, respectively (Type-2). For the Type-1 case, the airfoil model oscillates at a constant speed. For the Type-2 case, the oscillating motion changes in speed over the course of a single cycle of pitch-oscillating motion. The angular velocity abruptly increases immediately before the upstroke and decreases immediately after the upstroke. The reduced frequency, k , is defined as $k = \pi f c / U_0$. In general, it is known that the unsteady effect appears for $k > 0.2$ (Azuma (1993) [35]), and becomes significant for $k > 1$. The local reduced frequency for Type-2 oscillation is $0.5 k$ from $t' = 0.0-0.25$, and $1.4 k$ from $t' = 0.25-0.5$. The flow fields are measured using the 2CPIV method. For the oscillation in this chapter, it is inferred that the vortex generated by the discoid airfoil mainly consists of ω_y and ω_z . Therefore, to investigate the three-dimensional vortex structure, the PIV measurement is applied to several $x-z$ and $x-y$ plane (see fig. 4.2). The measurements were performed in the region from $y/c = 0.0-0.5$ at equal intervals of $y/c = 0.1$ in the $x-z$ plane, and in the region from $z/c = 0.0$ to 0.5 at equal intervals of $z/c = 0.1$ in the $x-y$ plane (Fig. 4.2). ω_y in the $x-z$ plane at $y/c > 0.5$ and ω_z in $x-y$ plane at $z/c > 0.5$ is neglected because these values are sufficiently small. The flow field is estimated using an ensemble averaged velocity over 20 pitching cycles.

Figure 4.3 shows the control volume used to evaluate the unsteady fluid force acting on the airfoil over a pitch-oscillating cycle. The control volume is chosen around the discoid airfoil, and the fluid force is estimated from time variations of momentum in the control volume using a momentum conservation law (Arita et al. (2011)) [36]. We confirmed that the variation of the fluid force calculated from this method follows the same trend as the fluid force measured by a load cell at $Re = 5.0 \times 10^4$.

4.2 Results and Discussions

Figure 4.4 shows the vortex structure under stationary conditions. Fig. 4.4 (a) shows that the discoid airfoil forms a vortex ring in the wake.

This vortex ring travels downstream. For $\alpha = 69.8^\circ$ and $\alpha = 110.2^\circ$, an inclined vortex ring is observed and the inclined angle of the vortex ring increases as the angle of attack increases. However, the inclined angle becomes smaller as the vortex ring travels downstream. The vortex ring is shed in the wake with a frequency of 100 Hz, and there is no difference in vortex shedding frequency for other angles of attack.

Figures 4.5 and 4.6 show the contour maps for the Type-1 vorticity in the x - z plane at $y/c = 0.0$ and 0.4 , respectively. The color bar indicates the strength of the vorticity. The airfoil profile is depicted for better understanding of the airfoil position at the measured angle of attack. For the discoid airfoil, the distance between the pitching axis and the airfoil edge decreases as y/c increases. Therefore, strong vortices are observed at $y/c = 0$, in contrast to those observed at $y/c = 0.4$. Namely, the vortex has a different structure in the spanwise direction, and three-dimensional deformation occurs in the wake.

Figure 4.7 shows the contour maps for Type-2 vorticity in the x - z plane at $y/c = 0.0$. A strong negative vortex exists near the upper edge of the airfoil from $t' = 0.4$ – 0.5 , in contrast to those for Type-1. This is because the angular velocity for Type-2, from $t' = 0.25$ – 0.5 , is faster than that for Type-1. At $t' = 0.63$, the vortices generated during downstrokes are concentrated in one large-scale vortex that travels in the downstream direction. The fluid forces generated by the airfoil model were calculated using a momentum conservation law applied to the flow field around the airfoil. Figure 4.8 shows the variation of the fluid force with respect to nondimensional time. There are two peaks in the fluid force over a single period of pitch-oscillating motion. In Type-1 oscillation, the two peaks in the fluid force curve were observed at $t' = 0.25$ and $t' = 0.75$. In Type-2 oscillation, the two peaks were observed at $t' = 0.4$ and 0.9 . In addition, the nondimensional time at which the fluid force indicated a peak value was delayed compared to that of Type-1. In addition, the peak value of the fluid force for Type-2 is larger than that for Type-1. Figures 4.9 and 4.10 show the three-dimensional vortex

structure for Type-1 and Type-2 oscillation, respectively. In these figures, the green regions show an iso-surface of nondimensional vorticity $|\omega c / U_0| = 6$. For Type-1 oscillation, during the downstroke of the pitch-oscillating motion, vortex growth is promoted near the upper edge of the airfoil. This occurs because of the pressure difference between the front and back sides of the airfoil. The fluid force increases as the vortex grows near the airfoil. A large-scale vortex exists near the upper edge of the airfoil at $t' = 0.25$. Thereafter, the fluid force decreases as the shed vortex travels in the downstream direction.

From $t' = 0-0.25$, the vortex remains close to the upper edge for Type-2 oscillation compared to that of Type-1 oscillation. Vortex growth is promoted after $t' = 0.25$ because of the change in the speed of airfoil movement associated with Type-2 oscillation, and the peak value of the fluid force increases relative to that for Type-1 oscillation. For Type-2, the oscillation speed abruptly increases immediately before the upstroke and decreases immediately after the downstroke. Therefore, the vortex grows near the upper edge of the airfoil immediately before the upstroke, and a strong vortex exists near the upper edge of the airfoil at $t' = 0.5$ (Fig. 4.10 (e)). For Type-2 oscillation, a strong vortex exists over a prolonged period of time near the airfoil edge because the fluid force increases over the course of a single pitching oscillation. This behavior is in contrast to that of Type-1 oscillation.

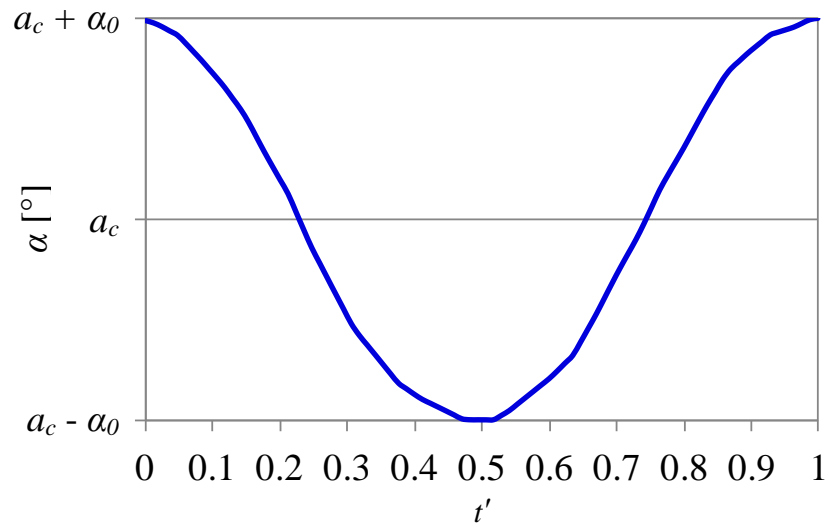
4.3 Conclusions

The vortical flow fields were measured during pitching oscillation as the angular speed was changed. The fluid force was calculated using a momentum conservation law, and the results of the experiment are summarized as follows:

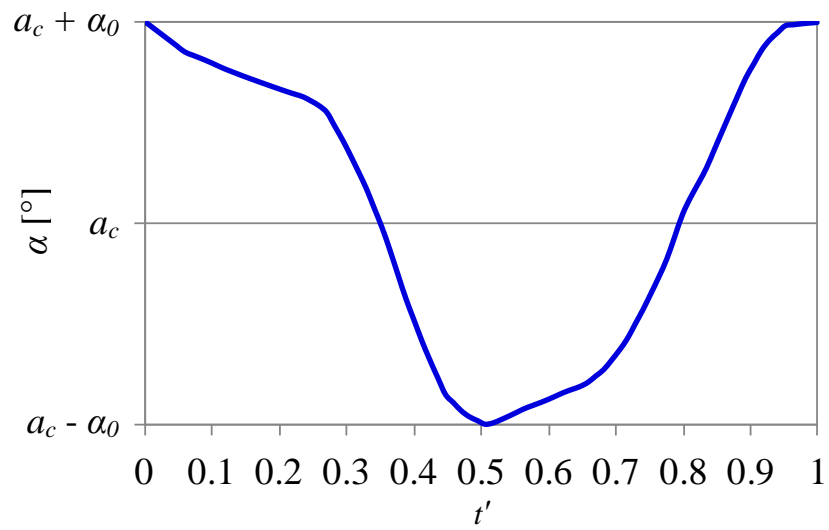
1. There are two peaks in the fluid force over the course of a single pitching

motion cycle. In Type-2 oscillation, the nondimensional time at which the fluid force exhibits a peak value is delayed in comparison with that of Type-1 oscillation.

2. The fluid force increases as a vortex grows near the airfoil. Thereafter, the fluid force decreases as the shed vortex travels in the downstream direction.
3. The peak value of the fluid force for Type-2 oscillation is larger than that for Type-1 oscillation. For Type-2 oscillation, a strong vortex exists close to the airfoil over a prolonged period of time. The fluid force increases over a single period of pitching oscillation, in contrast to what is observed in Type-1 oscillation.

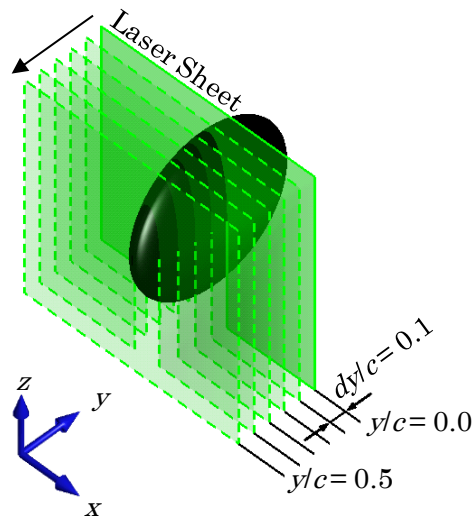


(a) Type-1

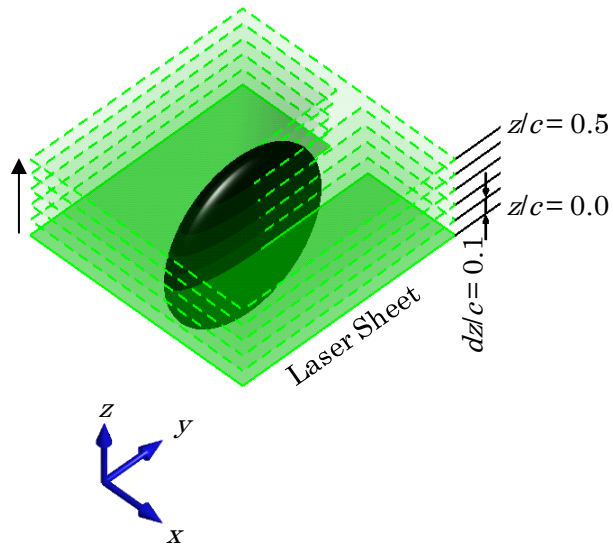


(b) Type-2

Fig. 4.1 The temporal change of α during pitch-oscillating motion



(a) x - z plane



(b) x - y plane

Fig. 4.2 Measurement region for 2CPIV

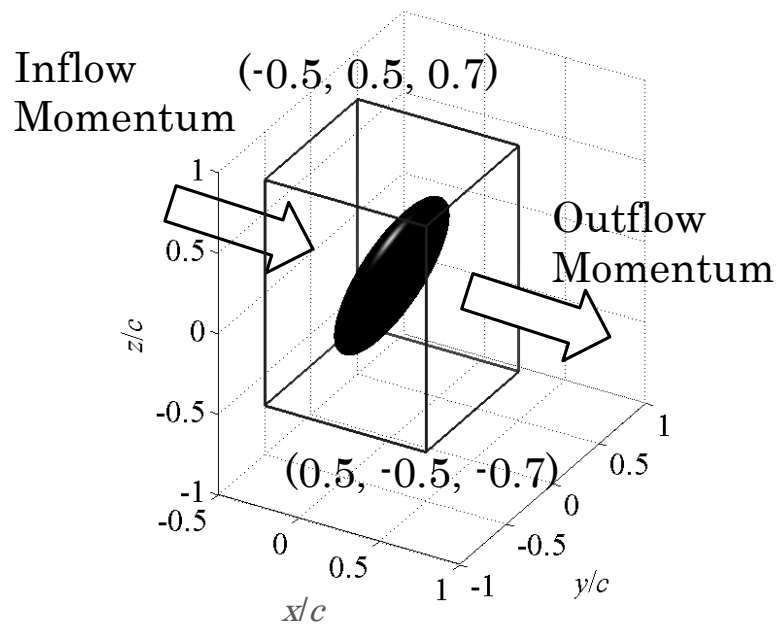
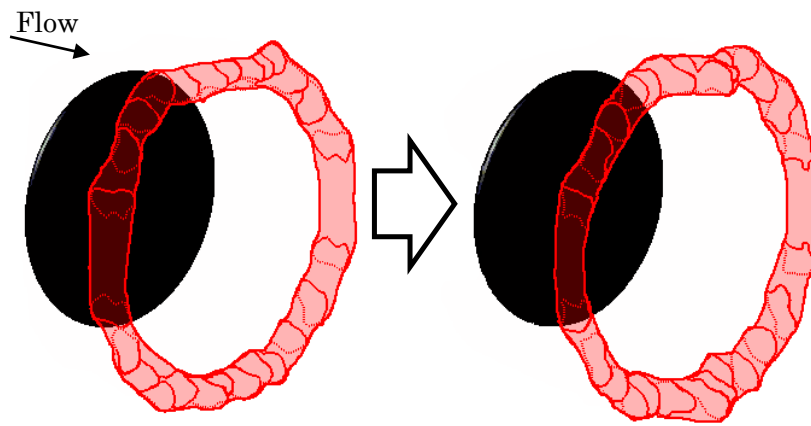
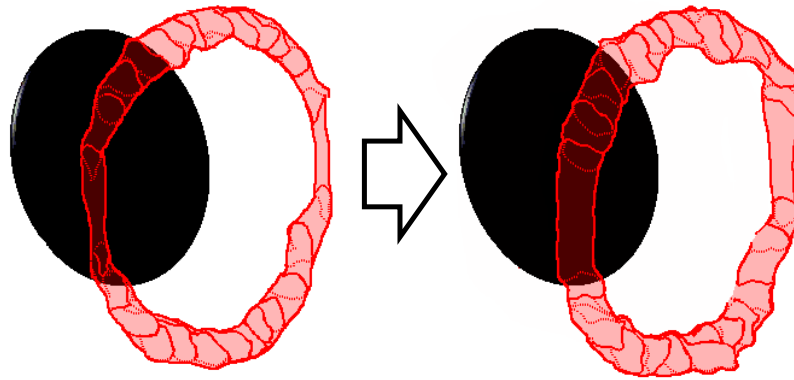
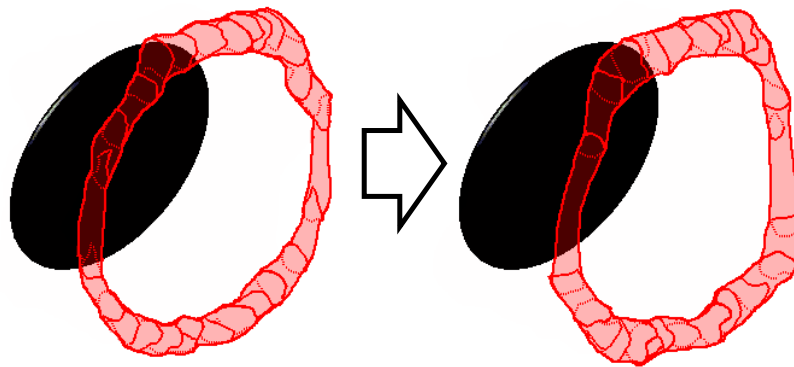


Fig. 4.3 Calculation of fluid forces using a momentum conservation law

(a) $\alpha = 90^\circ$ (b) $\alpha = 69.8^\circ$ (c) $\alpha = 110.2^\circ$ Fig. 4.4 Three-dimensional vortex structure under stationary conditions at $Re = 3.0 \times 10^4$

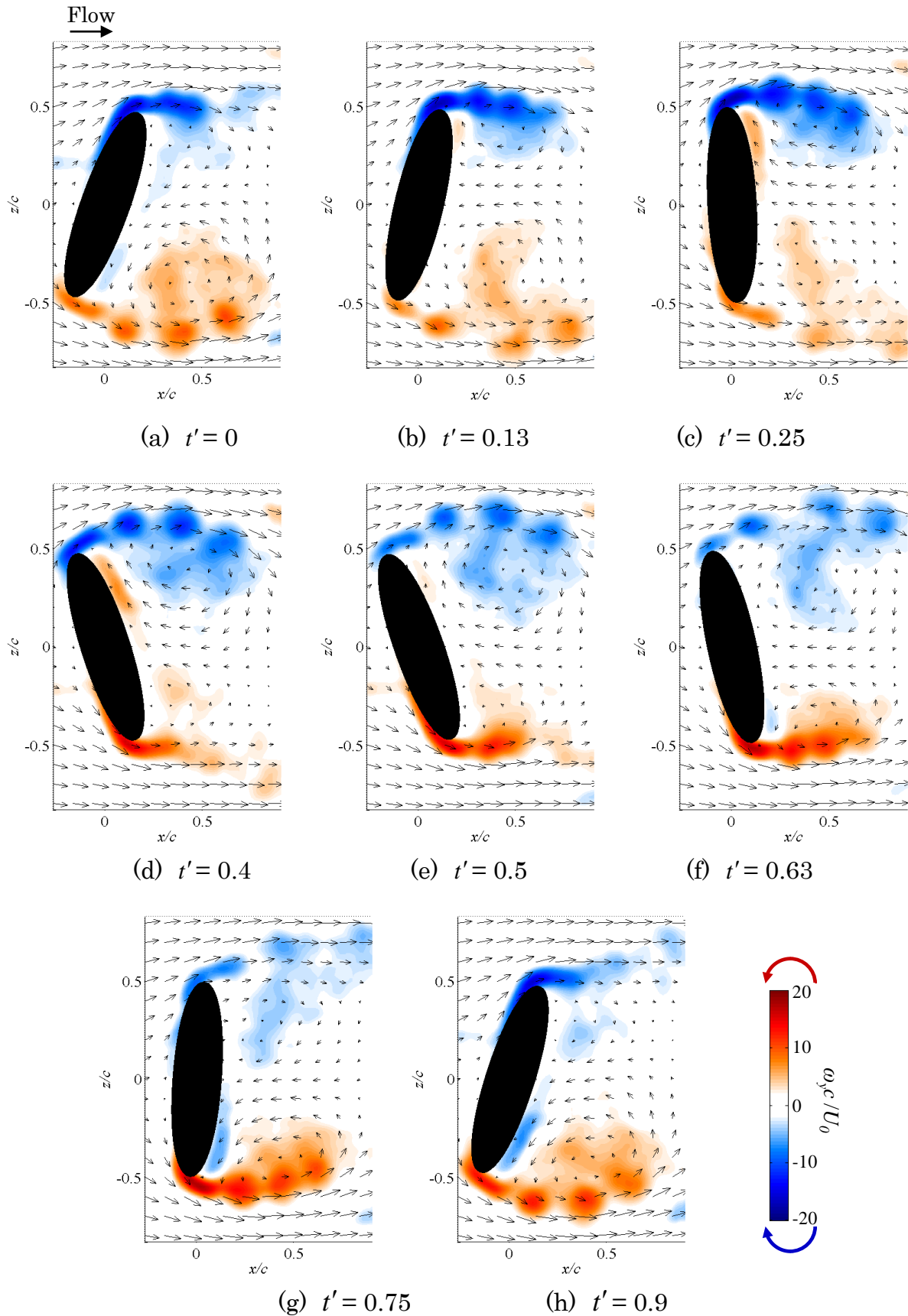


Fig. 4.5 Density map of vorticity in the x - z plane for Type-1 at $y/c = 0.0$ and $Re = 3.0 \times 10^4$

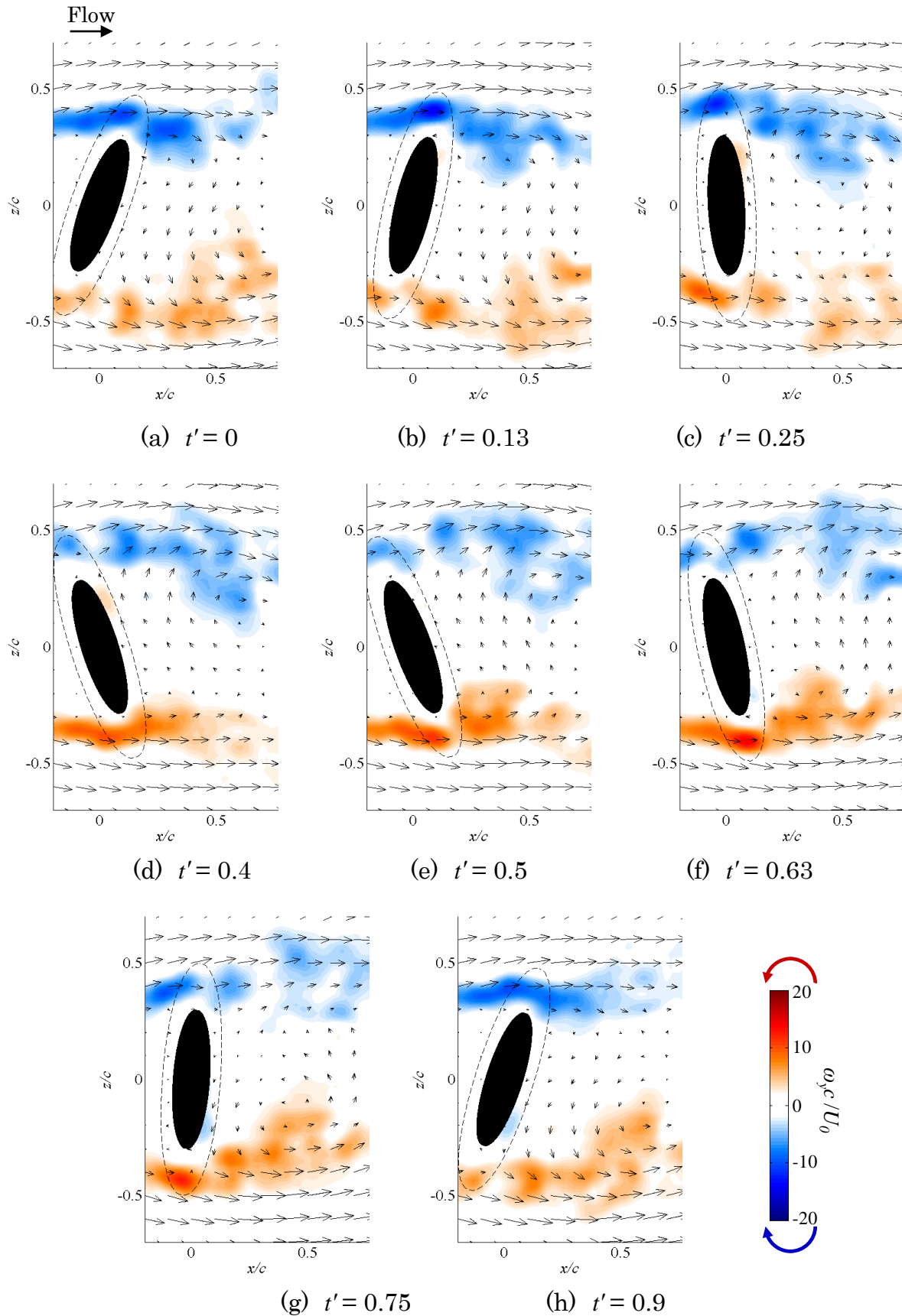


Fig. 4.6 Density map of vorticity in the x - z plane for Type-1 at $y/c = 0.4$ and $Re = 3.0 \times 10^4$

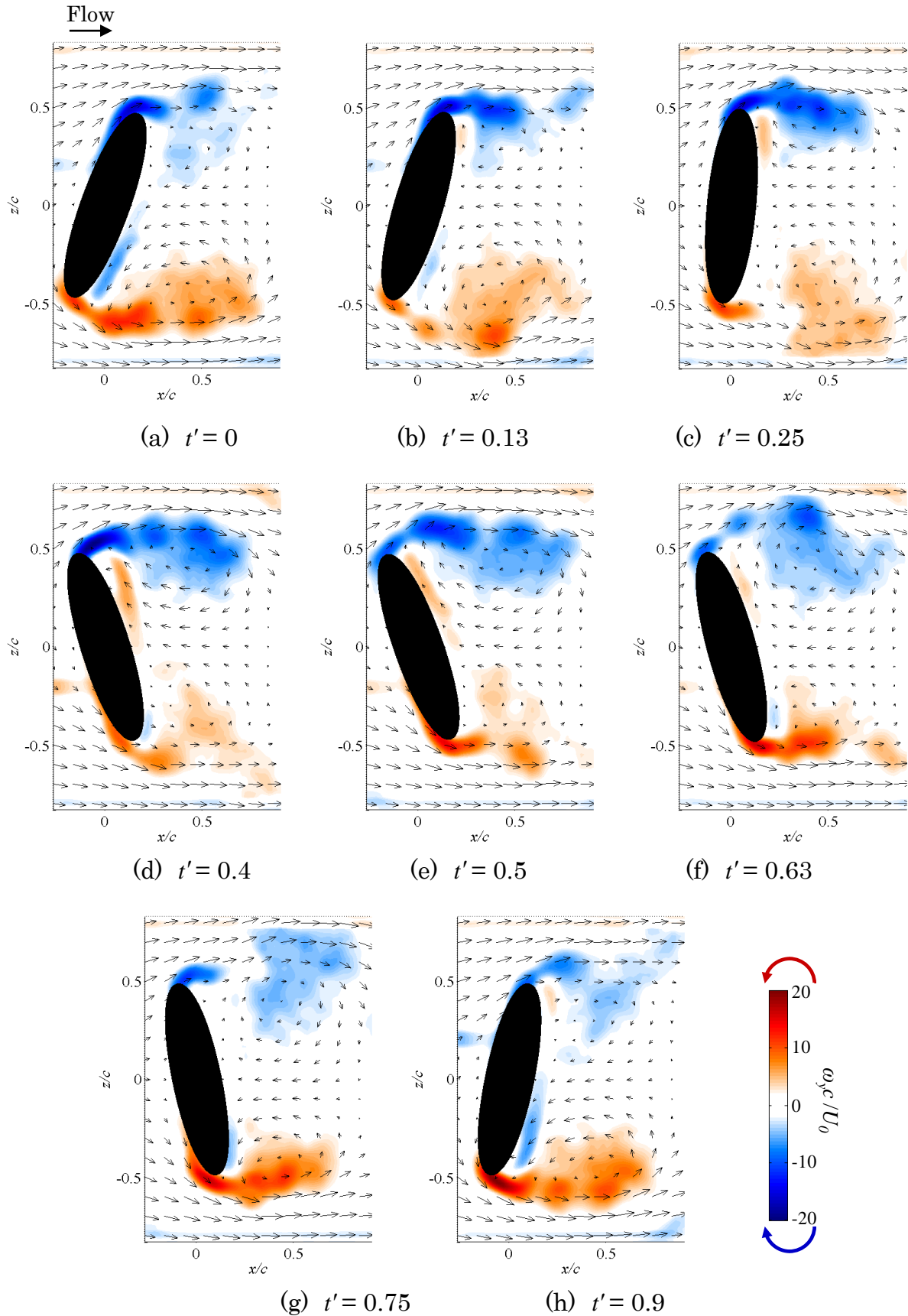


Fig. 4.7 Density map of vorticity in the x - z plane for Type-2 at $y/c = 0.0$ and $Re = 3.0 \times 10^4$

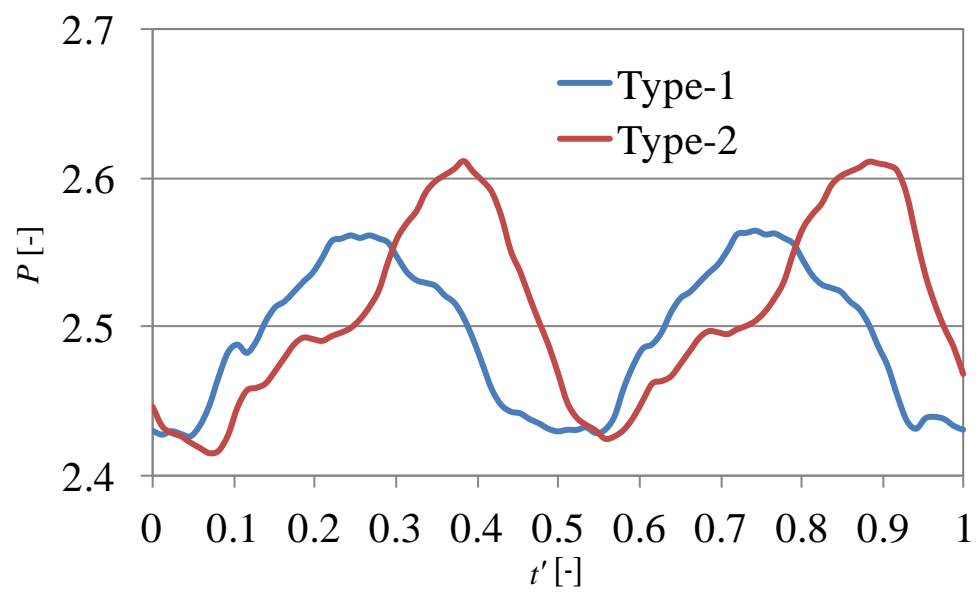
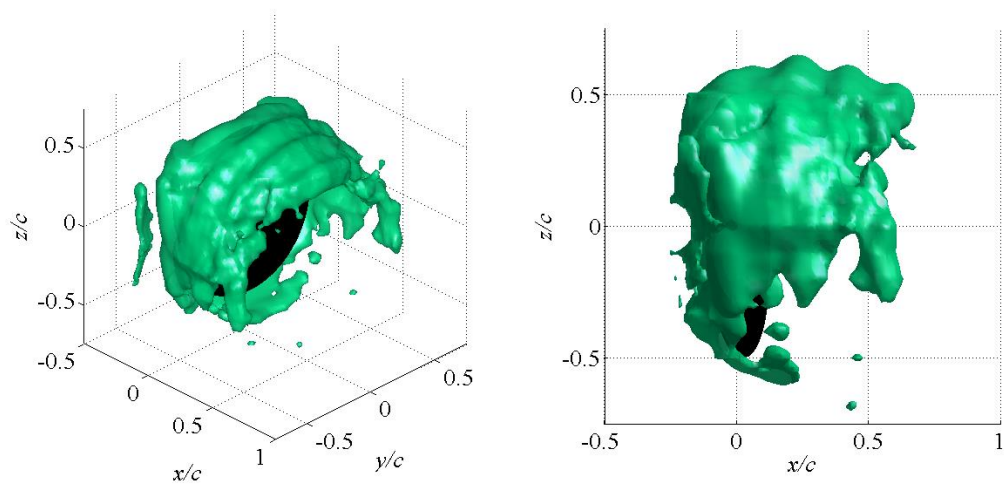
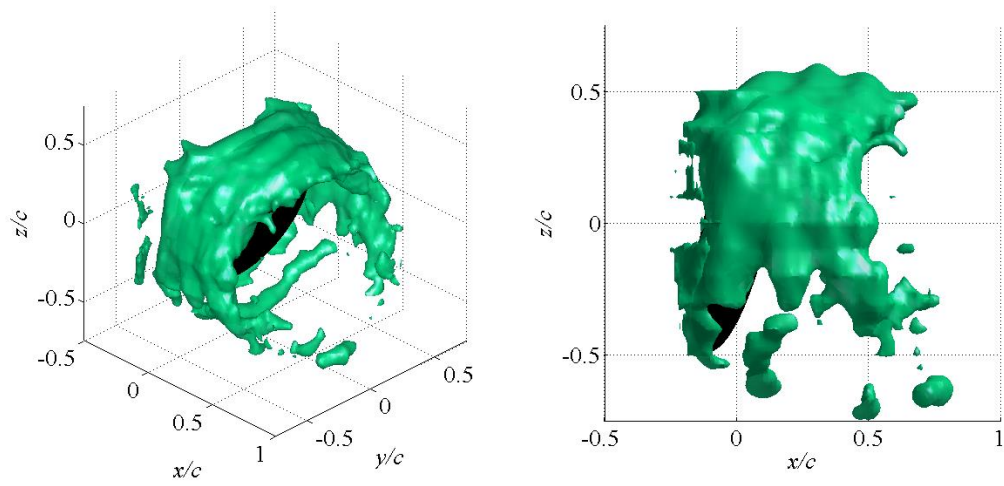
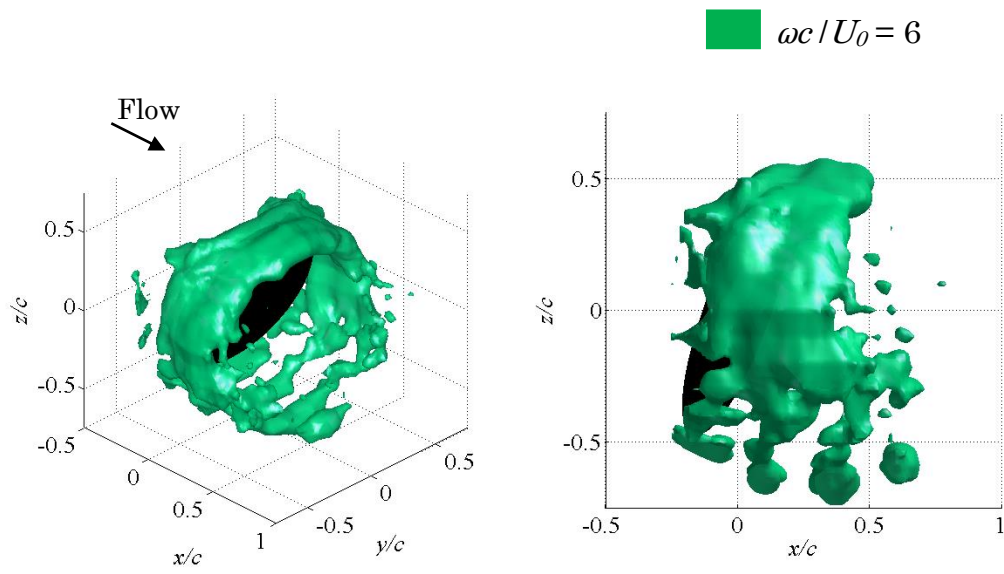
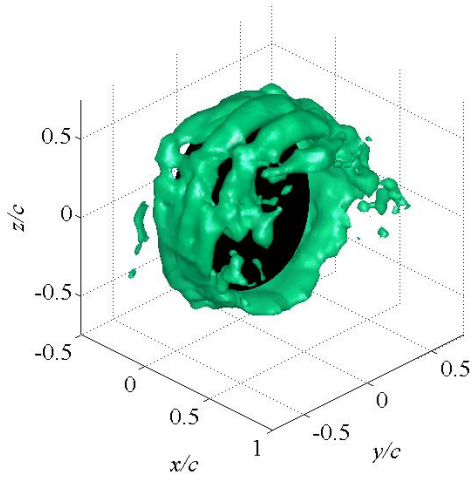
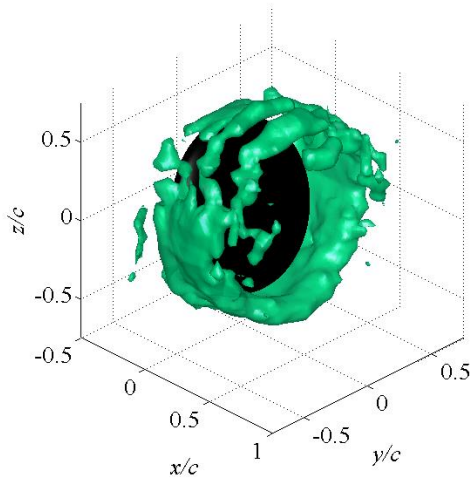
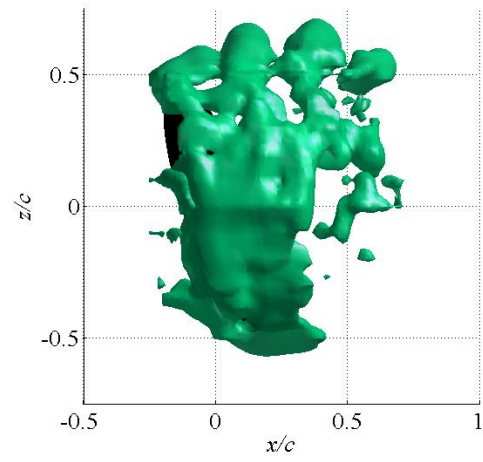


Fig. 4.8 Time history of the fluid force variation during pitch-oscillating motion at $Re = 3.0 \times 10^4$

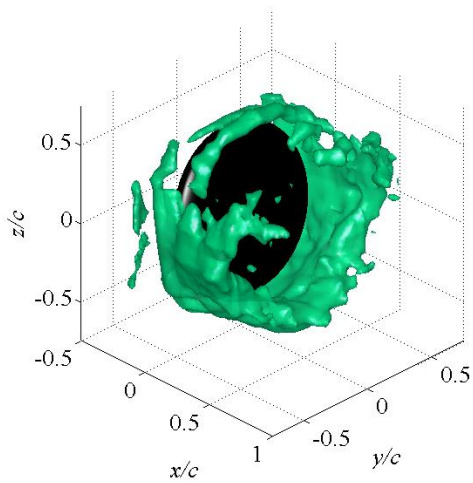
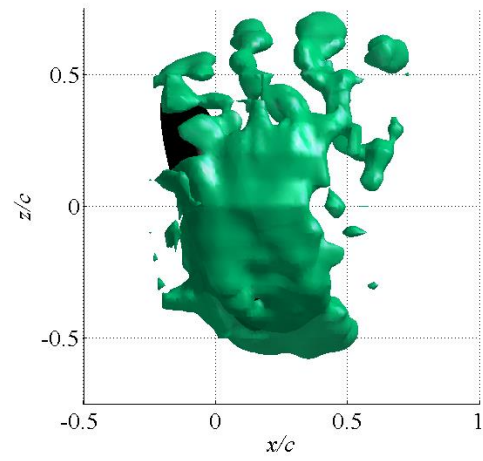




(d) $t' = 0.4$



(e) $t' = 0.5$



(f) $t' = 0.63$

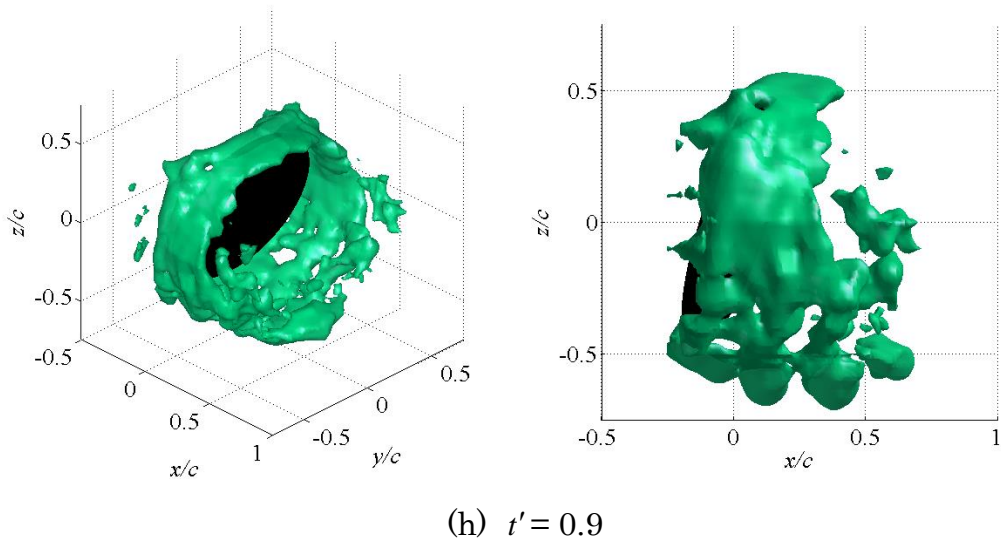
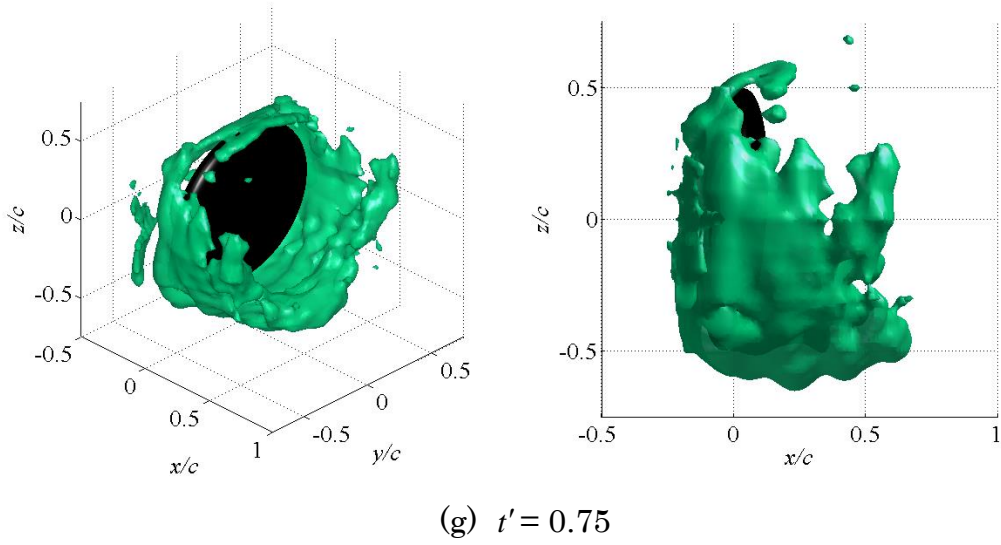
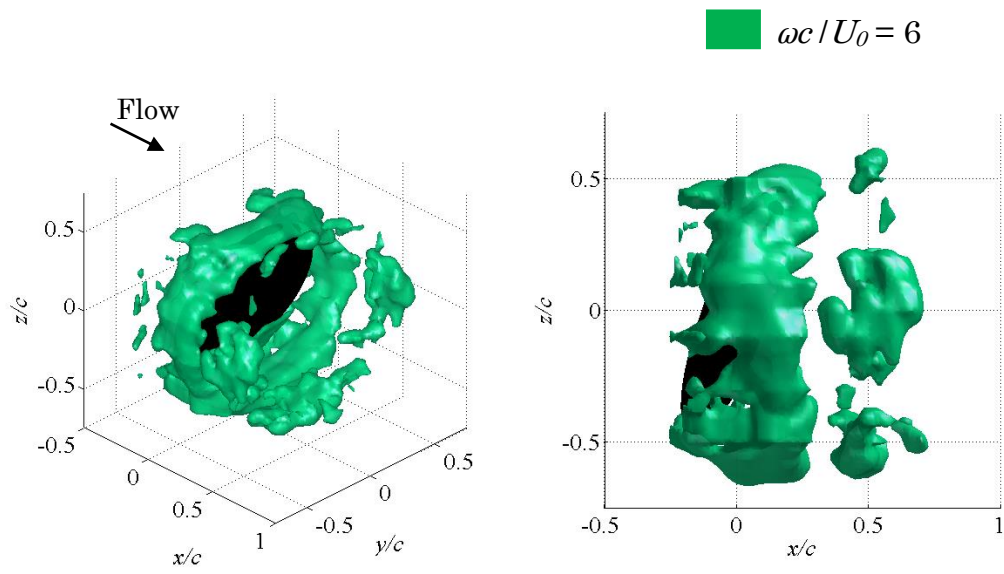
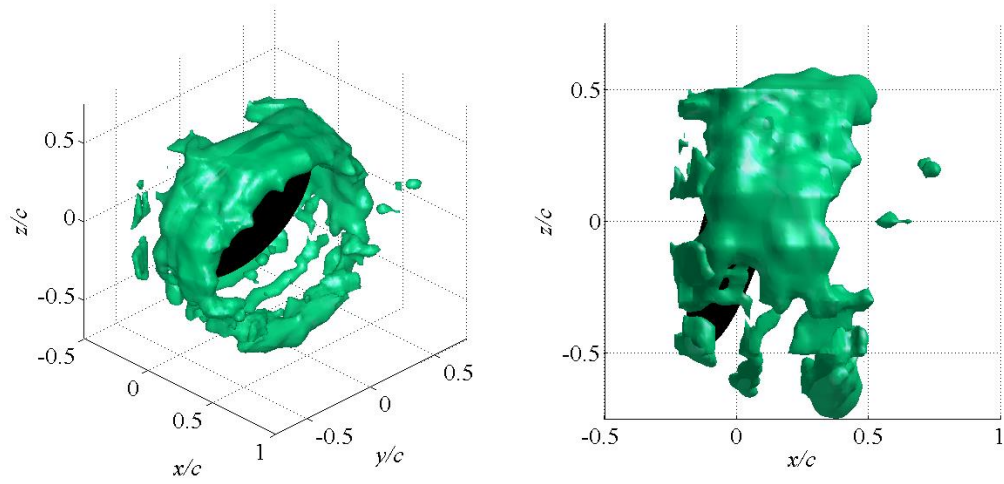
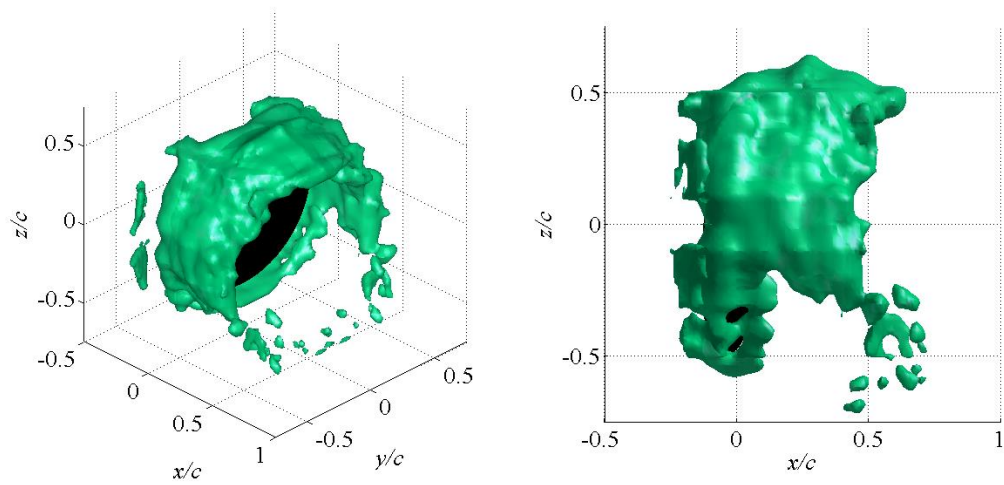
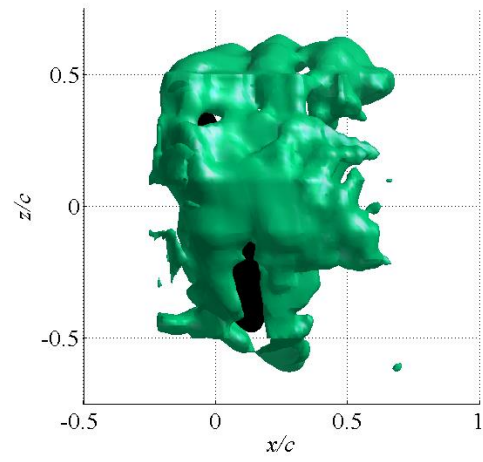
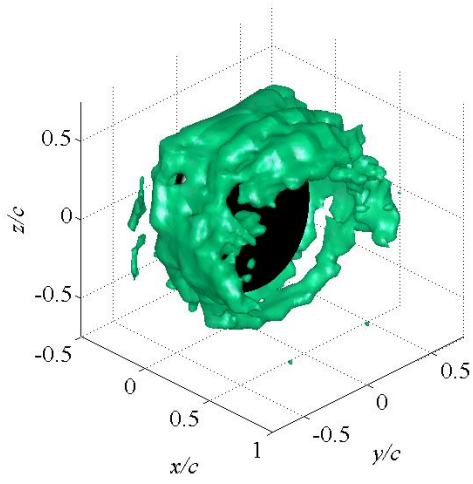
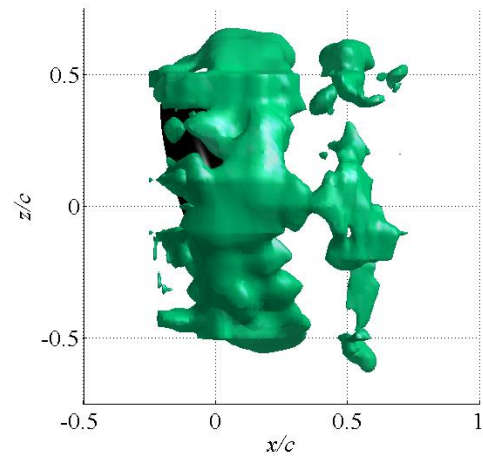
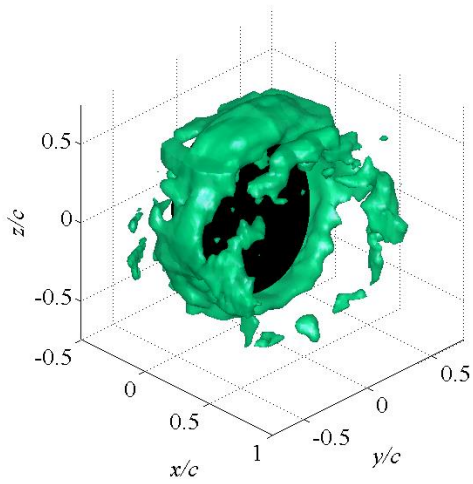


Fig. 4.9 Three-dimensional vortex structure for Type-1 at $Re = 3.0 \times 10^4$

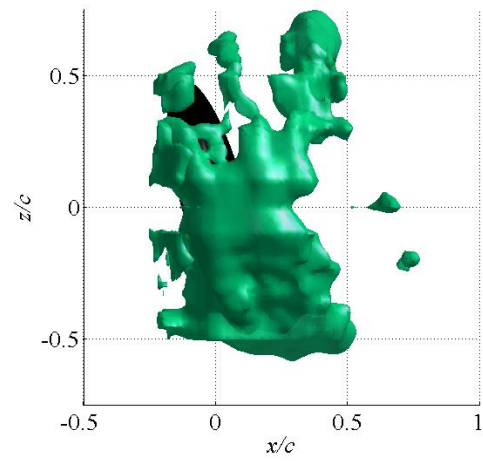
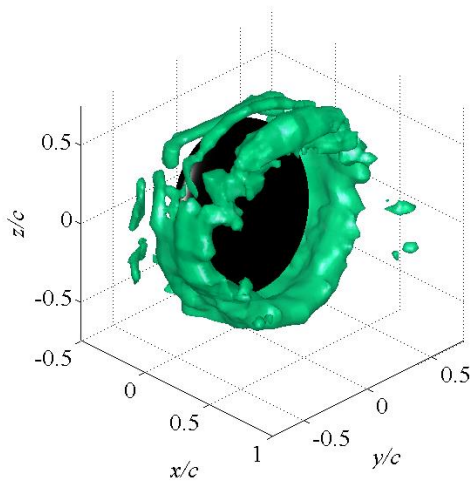
(a) $t' = 0$ (b) $t' = 0.13$ (c) $t' = 0.25$



(d) $t' = 0.4$



(e) $t' = 0.5$



(f) $t' = 0.63$

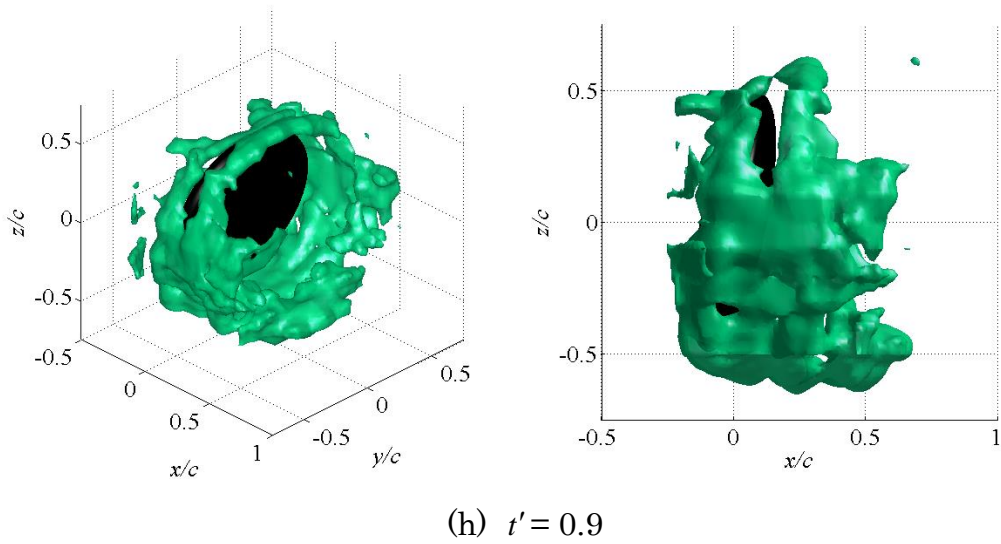
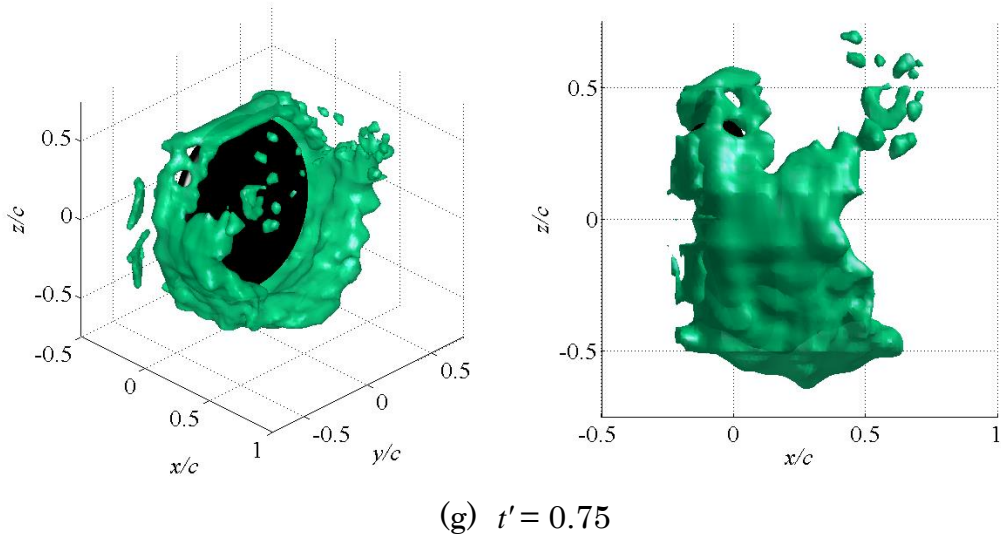


Fig. 4.10 Three-dimensional vortex structure for Type-2 at $Re = 3.0 \times 10^4$

5. EFFECT OF THREE-DIMENSIONAL AIRFOIL SHAPE ON VORTEX RING STRUCTURE DURING PITCHING MOTION

To investigate the influence of airfoil shape on unsteady fluid force during pitching motion around the oscillating 90° center angle, the three-dimensional vortex structures for discoid and rectangular airfoil were measured. The discoid and rectangular airfoils were used in this experiment.

5.1 Experimental Method

Experiments were conducted using the wind tunnel described in Fig. 2.1.1. The experiments were performed for $Re = 3.0 \times 10^4$. To investigate the influence of airfoil shape on vortex structure during pitching motion, two types of three-dimensional airfoils were used: the discoid airfoil and the rectangular airfoil with the NACA 0015 profile. Detailed information on each airfoil was provided in Section 2.3. The variation in angle of attack follows that of a sinusoidal curve and was shown in Fig. 4.1 (a). The reduced frequency, k , is defined as $k = \pi f c / U_0$. The flow fields are measured using the stereo PIV method. The stereo PIV system is shown in Fig 2.7. The measurements were performed in the region from $x/c = 0-1.0$ at intervals of $x/c = 0.033$ in the $y-z$ plane (Fig. 5.1). In order account for the fluid force caused by the unsteady effect during oscillation in two types of the airfoils (which have different cross sectional areas), the unsteady fluid force during pitching oscillation, F_{unst} , was nondimensionalized by the following equation.

$$F_{unst} = \frac{(F - F_{st})}{\overline{F_{st}}} \quad (5.1)$$

where F is the fluid force acting on the airfoil during pitching oscillation, and F_{st} is the fluid force in the stationary condition. The plotted curves in Fig. 5.8 were calculated at the angle of attack corresponding to each nondimensional time value. $\overline{F_{st}}$ is the mean value of F_{st} for each angle of attack.

5.2 Results and Discussion

5.2.1 3D Vortex Structure around a Discoid Airfoil

Figure 5.2 shows the three-dimensional vortex structure of the Q invariant of the velocity gradient tensor obtained by stereoscopic PIV. The green region in Fig. 5.2 shows the nondimensional Q iso-surface, $Qc^2/U_0^2 = 4$. A circular vortex ring forms near the wake of the airfoil at $t' = 0$. During the downstroke, vortex growth is promoted near the upper edge of the airfoil. This occurs because the pressure difference between the front and backsides of the airfoil become larger by increasing the relative velocity between the upper edge and the free-stream. The large-scale vortex exists near the upper edge of the airfoil at $t' = 0.25$. Figure 5.3 shows the three-dimensional vortex structure of each vorticity component around the discoid airfoil. In this figure, the green, red, and blue regions represent the nondimensional vorticity iso-surfaces, $|\omega_x c/U_0| = 4$, $|\omega_y c/U_0| = 7$, and $|\omega_z c/U_0| = 7$, respectively. ω_x is diminished in the wake of the airfoil throughout the cycle. In contrast, ω_y is strengthened near the upper edge of the airfoil during the downstroke, and increases near the upper edge of the airfoil from $t' = 0$ to 0.25. From $t' = 0.25$ –0.75, ω_y decreases near the upper edge of the airfoil. The variation of ω_y during pitch-oscillating motion was affected by the relative velocity between the upper edge of the airfoil and the free-stream. On the other hand, ω_z observed at both left and right extremities was not affected by the pitching motion. It is seen from Fig. 5.3 that the profile of

iso-surface ω_z does not change during pitch-oscillating motion, because the variation in the relative velocity due to the pitching motion is small near the pitching axis. Figure 5.4 plots the time history of each vorticity component throughout a pitch-oscillating cycle. Here, the vertical axis denotes the averaged nondimensional vorticity in the wake of the airfoil. ω_y most widely varies among the three vorticity components, while ω_x varies coordinated with the fluid force (Fig. 5.8). The unsteady fluid force generated by the pitch-oscillating airfoil is largely determined by ω_y .

5.2.2 3D Vortex Structure around a Rectangular Airfoil

Figure 5.5 shows the three-dimensional vortex structure around the rectangular airfoil for $k = 0.97$ and $Re = 3.0 \times 10^4$. A rectangular vortex ring forms in the wake of the rectangular airfoil at $t' = 0.08$, which was generated during the upstroke in the previous cycle. During the downstroke, the vortex growth is promoted near the upper edge of the airfoil. Furthermore, the upper part of the vortex ring is connected to the airfoil via the vortex at both left and right extremities. However, at $t' = 0.17$, the vortex ring (Fig. 5.5 (b) red dotted line) exists farther downstream than in the discoid airfoil case. Hence, the vortex at both left and right extremities (Fig. 5.5 (c) blue dotted line) is stretched in the downstream direction and the vortex ring is deformed. The upper part of the vortex ring breaks down at $t' = 0.58$, in contrast to the discoid airfoil at $t' = 0.58$. Figure 5.6 shows the three-dimensional vortex structure of each component of the vorticity around the rectangular airfoil. At $t' = 0.25$, for the rectangular airfoil, ω_x appears near the upper edge of the airfoil during downstroke (marked by the circle in Fig. 5.6 (b)). Subsequently, ω_x increases as the vortices at the left and right extremities (Fig. 5.6 (c) dotted lines) stretch in the downstream direction, causing vortex breakdown to occur. On the other hand, for the discoid airfoil, ω_x was observed farther downstream, and vortex deformation did not occur in the near wake of the discoid airfoil. Figure 5.7 plots the time history of

each vorticity component in the wake of the rectangular airfoil during a pitch-oscillating cycle. ω_x increases just before the airfoil motion changes direction. The increase in ω_x indicates that the vortices at the left and right extremities stretch in the downstream direction. In other words, the upper part of the vortex travels farther downstream (Fig. 5.5 (c) red dotted line) in contrast to the discoid airfoil (Fig. 5.2 (c) red dotted line). In addition, ω_y decreases as ω_x increases, meaning that the vorticity is transported from the upper part of the vortex to the vortices at both left and right extremities. Therefore, the ω_y decrease is rapid in comparison with to that for the discoid airfoil, and the vortex breakdown for the rectangular airfoil occurs earlier than for the discoid airfoil. ω_z is larger for the rectangular airfoil than for the discoid airfoil throughout the pitch-oscillating cycle, because the vortex near the extremity of the airfoil in the spanwise direction becomes stronger.

5.2.3 Fluid Force Characteristics

Figure 5.8 shows the unsteady fluid force variation during pitch-oscillating motion for $k = 0.97$ and $Re = 4.0 \times 10^4$. The two peaks are observed in the fluid force curve for each model. The fluid force variation is similar to the ω_y variation during one pitch-oscillating cycle. The unsteady fluid force for the discoid airfoil is greater than that for the rectangular airfoil throughout one pitch-oscillating cycle. This is because, for the discoid airfoil, the vortex breakdown was delayed (Figs. 5.2 (d) and 5.5 (d)) and the vortex exists in its wake over a prolonged period of time.

5.3 Conclusions

To investigate the effect of a three-dimensional airfoil shape on the three-dimensional vortex structure for an oscillating airfoil, two types of airfoil shapes were used. The main conclusions of this study are summarized

as follows.

1. A circular vortex ring forms in the wake of the discoid airfoil. The vortex ring in the wake of the discoid airfoil maintains its circular shape throughout the pitch-oscillating cycle.
2. A rectangular vortex ring forms in the wake of the rectangular airfoil. The vortex deforms at the extremities of the rectangular airfoil in the spanwise direction. The vortex breaks down near the airfoil.
3. The fluid force generated by the discoid airfoil throughout one pitch-oscillating cycle becomes larger than the fluid force generated by the rectangular airfoil, because the vortex exists in the wake of the discoid airfoil over a prolonged period.

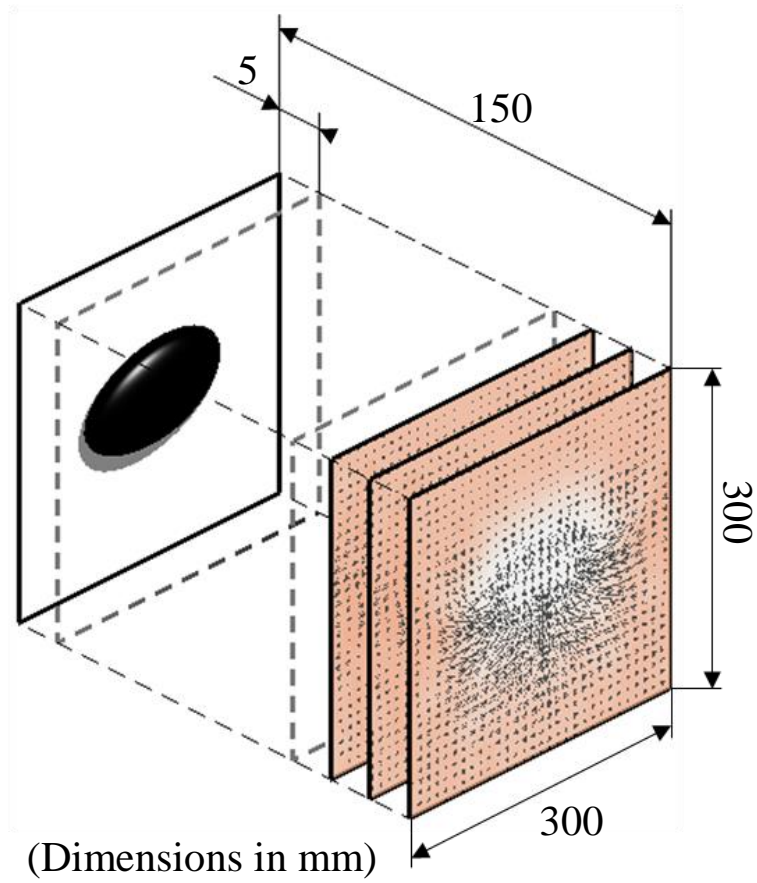
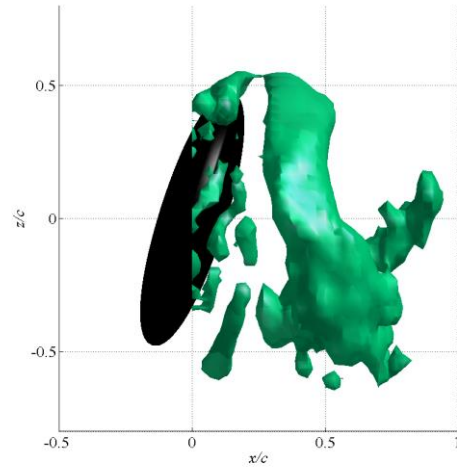
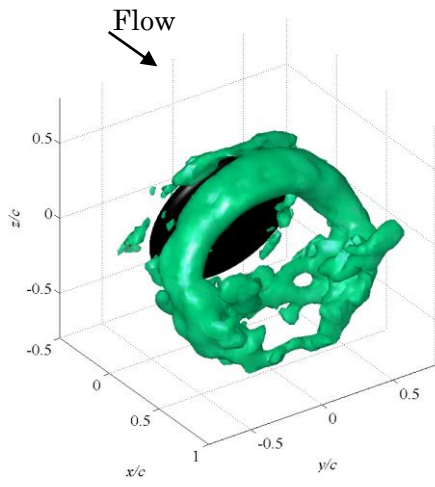
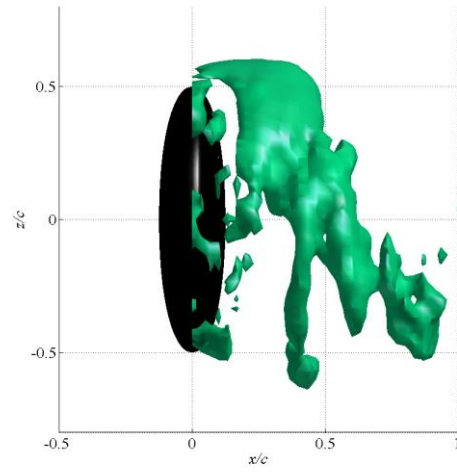
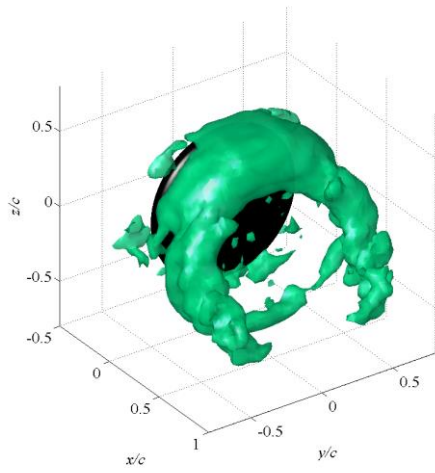
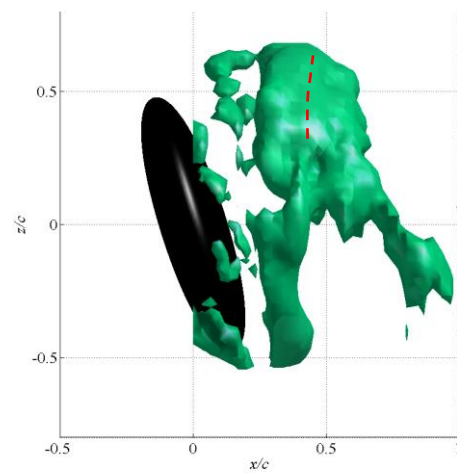
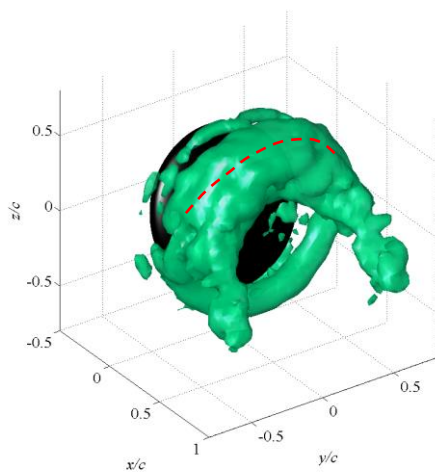


Fig. 5.1 Measurement region of stereoscopic PIV

$$Qc^2 / U_0^2 = 4$$

(a) $t' = 0.08$ (b) $t' = 0.25$ (c) $t' = 0.42$

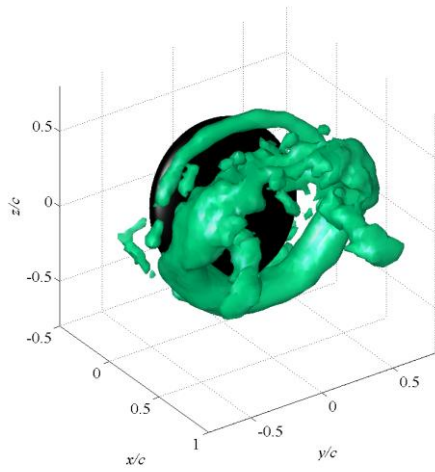
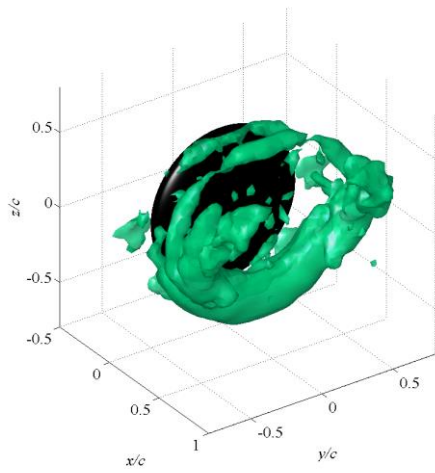
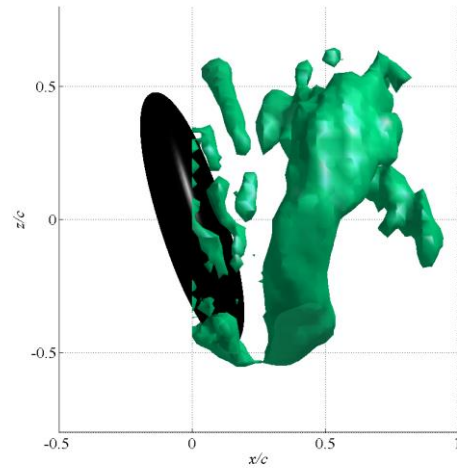
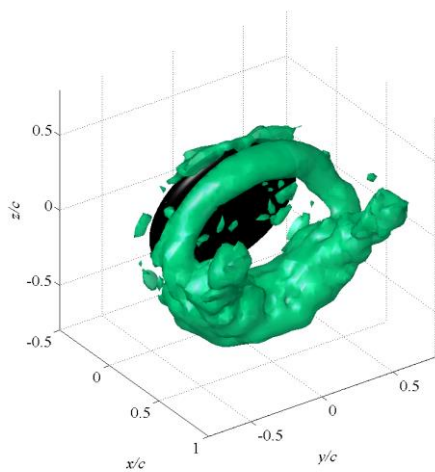
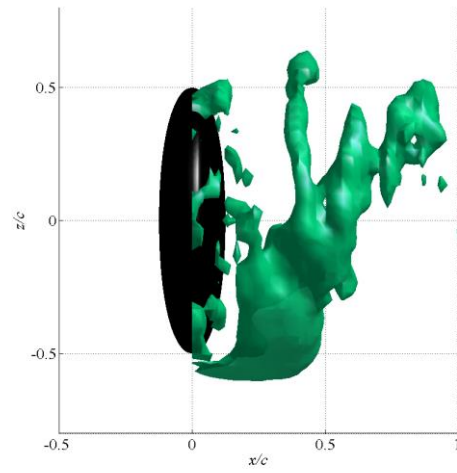
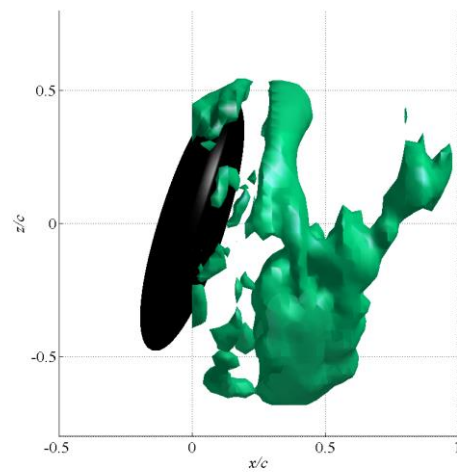
(d) $t' = 0.58$ (e) $t' = 0.75$ (f) $t' = 0.92$ 

Fig. 5.2 Three-dimensional vortex structure around the pitch-oscillating discoid airfoil for $k = 0.97$ and $Re = 3.0 \times 10^4$

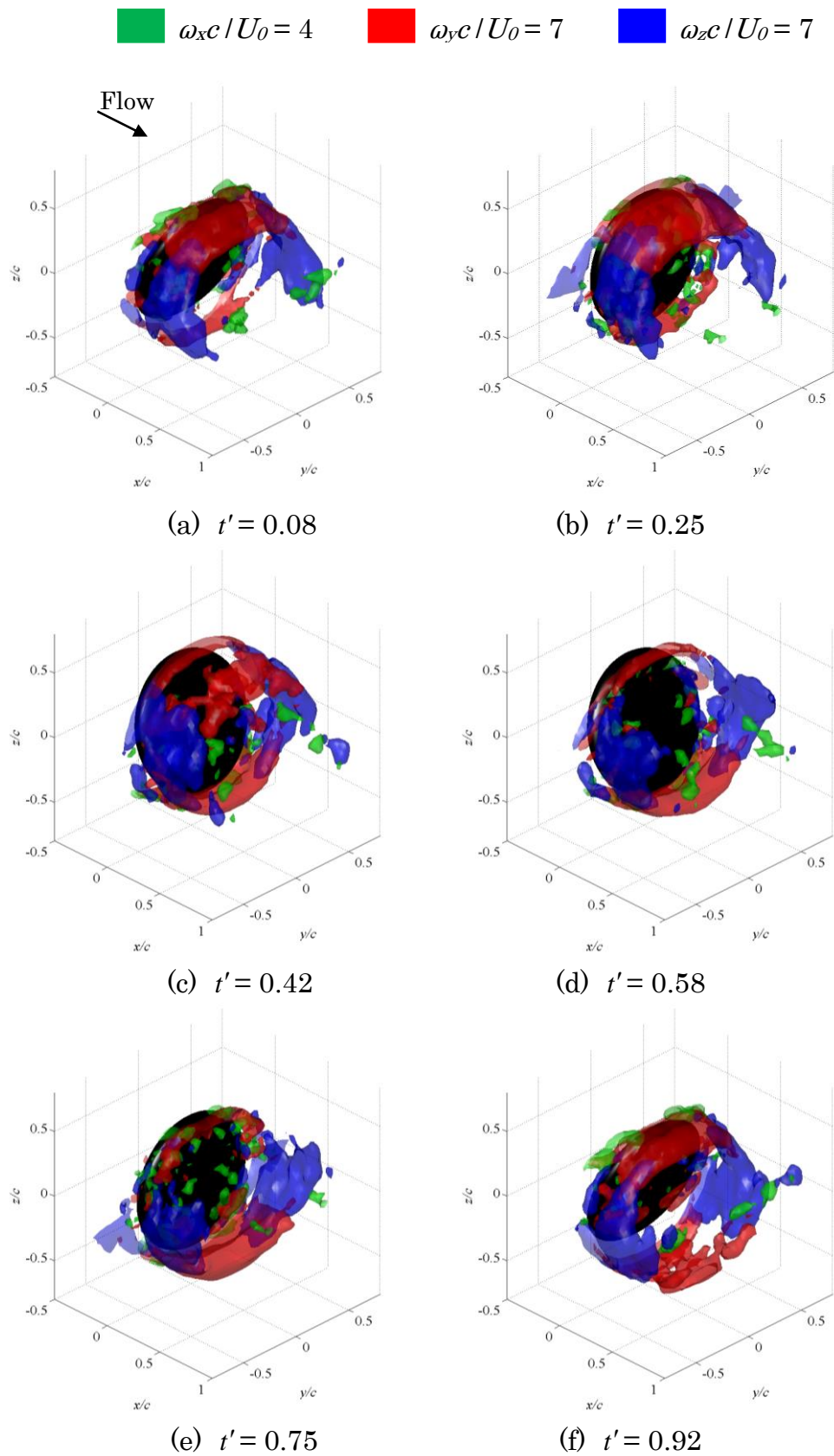


Fig. 5.3 Three-dimensional vortex structure of each vorticity component around the discoid airfoil for $k = 0.97$ and $Re = 3.0 \times 10^4$

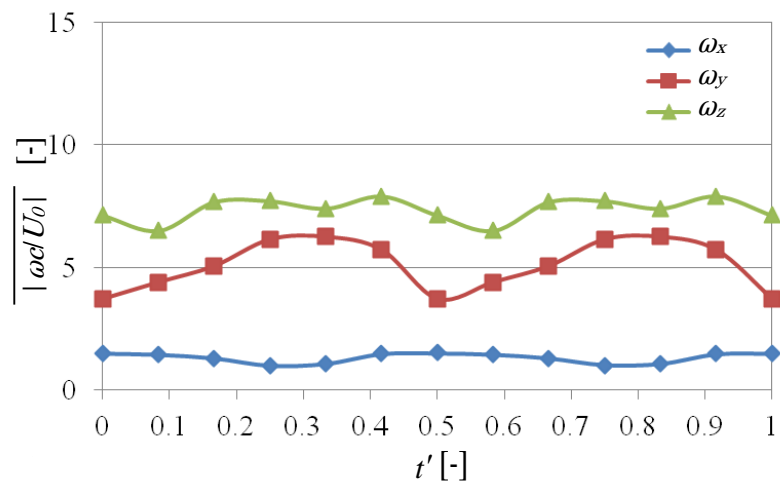
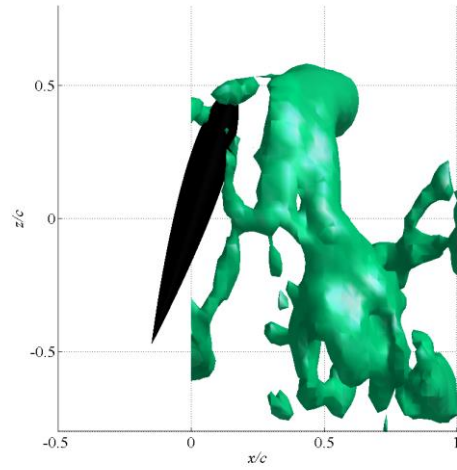
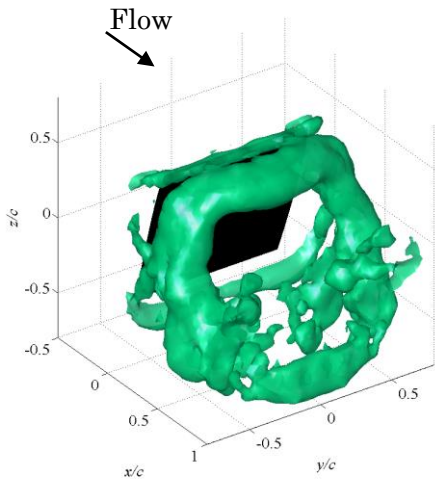
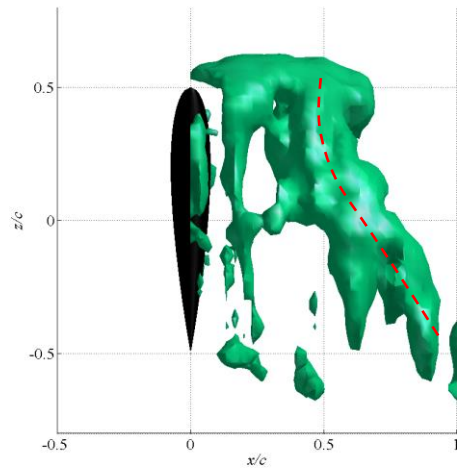
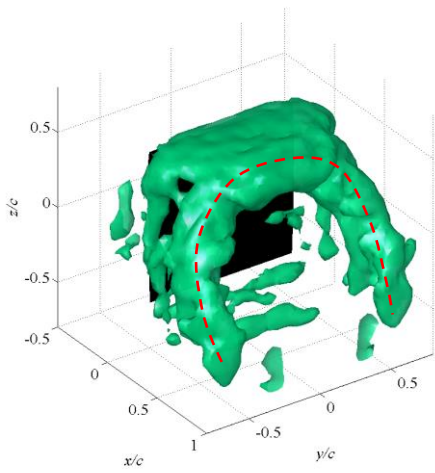


Fig. 5.4 Time history of each vorticity component during a pitch-oscillating cycle for the discoid airfoil for $k = 0.97$ and $Re = 3.0 \times 10^4$

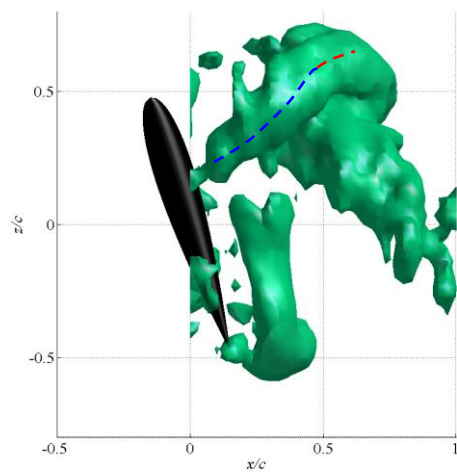
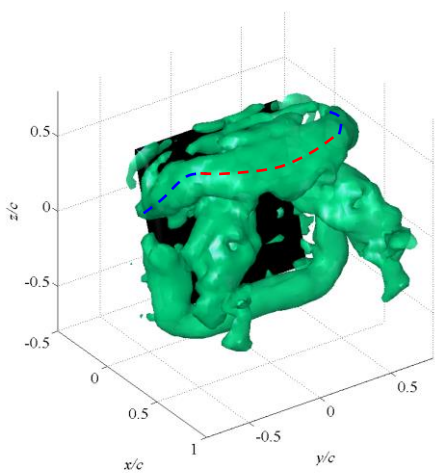
$Qc^2 / U_0^2 = 4$



(a) $t' = 0.08$



(b) $t' = 0.25$



(c) $t' = 0.42$

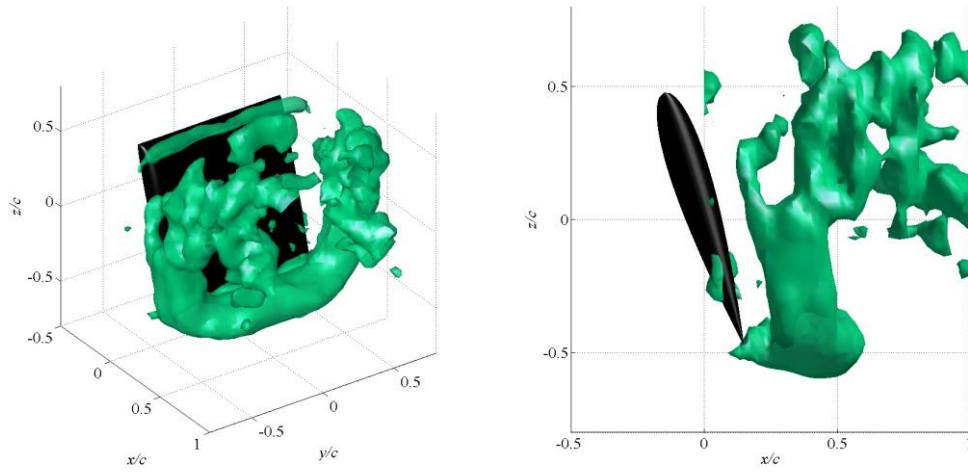
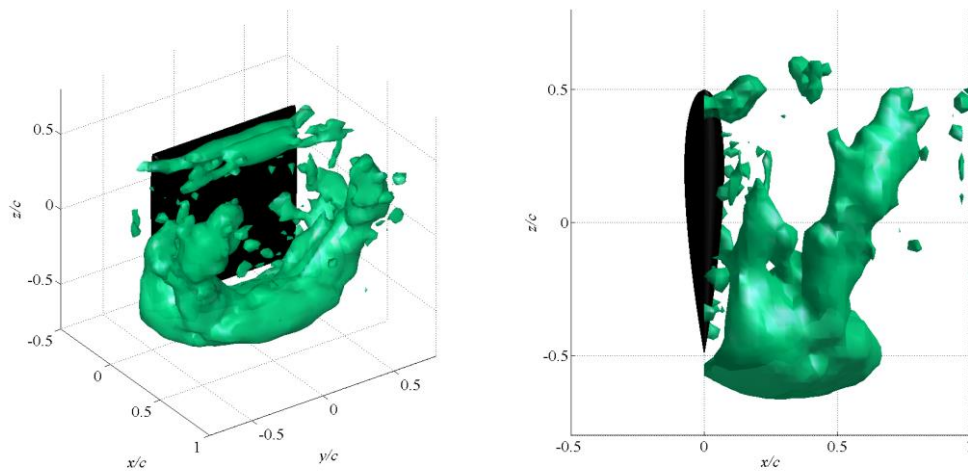
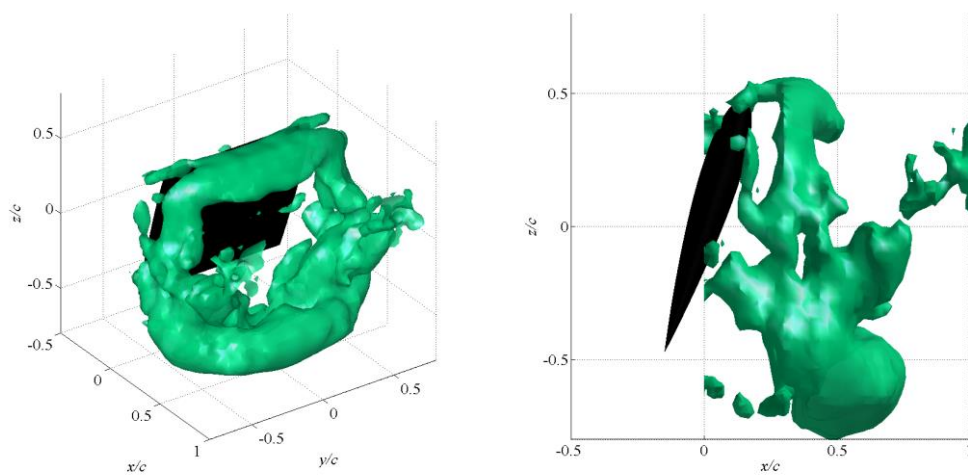
(d) $t' = 0.58$ (e) $t' = 0.75$ (f) $t' = 0.92$

Fig. 5.5 Three-dimensional vortex structure around the pitch-oscillating rectangular airfoil for $k = 0.97$ and $Re = 3.0 \times 10^4$

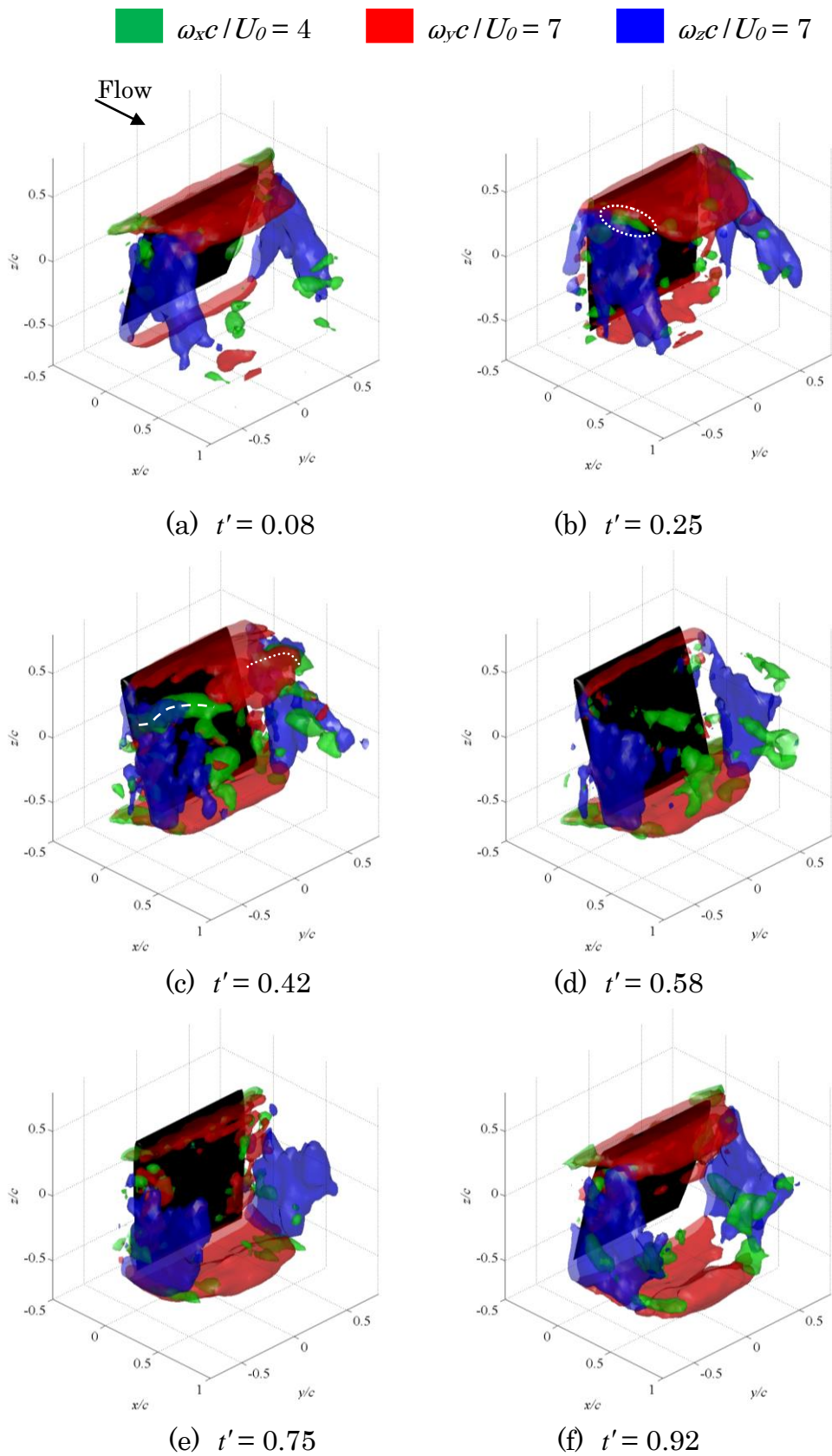


Fig. 5.6 Three-dimensional vortex structure of each vorticity component around the rectangular airfoil for $k = 0.97$ and $Re = 3.0 \times 10^4$

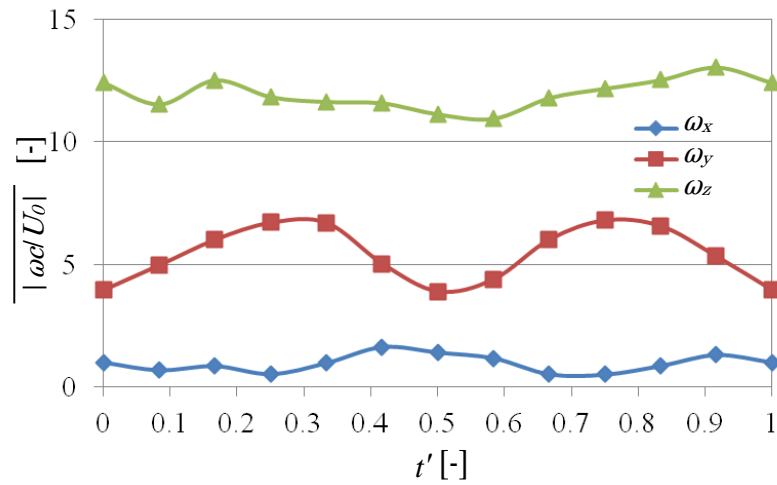


Fig. 5.7 Time history of each vorticity component during a pitch-oscillating cycle for the rectangular airfoil for $k = 0.97$ and $Re = 3.0 \times 10^4$

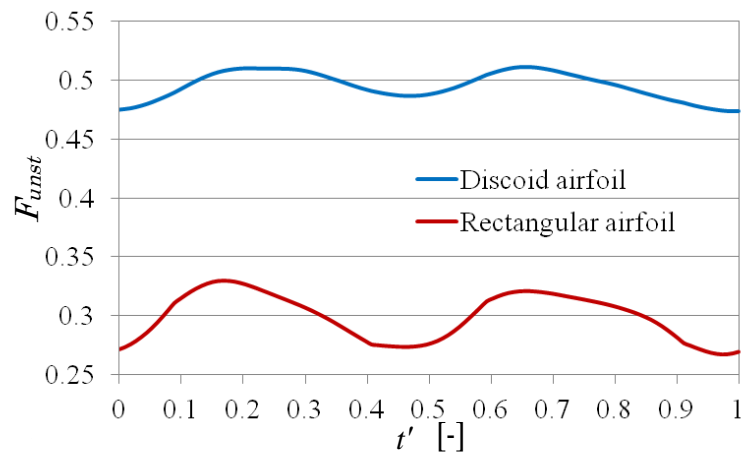


Fig. 5.8 Fluid force curve during pitch-oscillating motion for $k = 0.97$ and $Re = 4.0 \times 10^4$

6. PROPULSIVE FORCE AND THREE-DIMENSIONAL VORTEX STRUCTURE DURING MONOFIN OSCILLATION

The vortex ring structure generated by a pitch-oscillating discoid airfoil is a rather complex mechanism to use for calculating propulsive force. Therefore, the flow field and propulsive force are measured using the monofin, which generates a relatively simple vortex ring. In this chapter, the propulsive force and three-dimensional vortex structure on the monofin explains before the propulsive force estimate from the momentum of vortex ring in chapter 7.

6.1 Experimental Method

Figure 2.2.2 shows the schematic of the experimental setup. Experiments were performed in a circulating water channel, which has a length of 4.6 m, a span of 2.0 m, and a depth of 1.2 m, and which includes a glass-windowed observation section (Fig. 2.2.1). The test model was shown in Figure 2.4. The monofin has a chord length of 320 mm and a span of 360 mm. The monofin was made from laminate composite materials and its thickness decreases from the root to the tip. The oscillating motions of the monofin were operated by a drive unit. The oscillating center, a_c , in the motion was set at -20° and the pitching angle, a_θ , was $\pm 20^\circ$. The experimental conditions were determined by referencing the fin movements of the top swimmer in fin swimming (Luersen et al. 2006) [37]. Figure 6.1 shows the angle of attack of

the monofin with respect to nondimensional time. In this experiment, $t' = 0$ is defined as the upper dead point ($\alpha = 0^\circ$) during fin motion. To investigate efficient monofin swimming motion, five types of oscillations were performed. For the standard oscillation case, the variation in the angle of attack follows the pattern of a sinusoidal curve. Four types of fast kick-up and fast kick-down oscillations were given. The speed ratio in the kick-up and kick-down motions are summarized in Table 1. The propulsive forces were measured by a load cell attached to the top of the drive unit. The flow fields are measured using the stereoscopic PIV method (Fig. 2.8). Figure 6.2 shows the measurement region in the downstream direction for the stereoscopic PIV. The measurements were performed in the region from $x = 80\text{--}1020$ mm at equal intervals of $x = 20$ mm in the $y\text{--}z$ plane. The flow field is estimated using an ensemble averaged velocity over 30 pitching cycles. The three-dimensional vortex structure was visualized by the iso-surface of the Q invariant of the velocity gradient tensor.

6.2 Results and Discussion

Figure 6.3 shows the variation of the propulsive force with respect to nondimensional time. The propulsive force, P , was calculated by following equation

$$P = \frac{F - F_{st}}{\left(\overline{F - F_{st}}\right)_{\text{standard}}} \quad (6.1)$$

where F is the fluid force acting on the monofin during the oscillation, and F_{st} is the fluid force at the stationary condition. The plotted curves in Fig. 6.3 were calculated at the angle of attack corresponding to the nondimensional time. $\left(\overline{F - F_{st}}\right)_{\text{standard}}$ is the mean value of $F - F_{st}$ for each angle of attack in the standard case. For the standard case, a peak is observed at $t' = 0.76$. A negative propulsive force is observed during kick-down, which indicates that the fin motion during kick-down generates the drag force. This occurs because the trailing edge of the monofin moves in the opposite direction of

the freestream during the kick-down motion. The negative value in Fig. 6.3 indicates that the monofin moves in the propulsive direction at a speed that is lower than $U_0 = 0.5$ m/s. On the other hand, for two types of fast kick-up motion, the propulsive force curve has two peaks, and the second peak is larger than the first peak. Two peaks are observed at $t' = 0.12$ and $t' = 0.91$ for fast kick-up 1 and 2. Furthermore, the maximum propulsive force is greater than that for the standard case, and its value increases with increasing kick-up speed. The time during which the drag force is observed becomes longer as kick-down speed becomes slower. On the other hand, for two types of fast kick-down motions, a high propulsive force was observed during one oscillating cycle. A propulsive force peak occurs at $t' = 0.49$ and at $t' = 0.68$ for fast kick-down 1 and 2, respectively. Furthermore, the maximum propulsive force value increases with increasing kick-down speed. Altogether, the motion with the largest velocity difference in kick-up and kick-down speed enhanced the propulsive force during the kick-up, and the motion with the fastest kick-down speed decreases the averaged drag force during kick-down. As a result, the propulsive force during one oscillating cycle for the fast kick-down case is highest among the five oscillations.

Figure 6.4 shows the vorticity contour map and the velocity vector at $y = 0$ mm in the x - z plane for the standard, fast kick-up 1 and fast kick-down 1 motions. In this figure, each flow field corresponds to the nondimensional time immediately after the propulsive force reaches a maximum value for each motion. The monofin profile is depicted in this figure for better understanding of the fin position at the measured angle of attack. The negative and positive vortices were generated during kick-up and kick-down motion, respectively. In all cases, a negative vortex exists on the lower surface during kick-up motion. The oscillating motion with different kicking speed in kick-up and kick-down generates a strong negative vortex in comparison with that for the standard case. Hence, it is predicted that the negative vortex strength on the lower surface of the monofin during the kick-up motion is related to propulsive force generation. For fast kick-up, strong negative vortex generation is caused by an increase in the pressure

difference between the upper and lower surface of the monofin during kick-up. This is initiated by fast kick-up speed. On the other hand, for fast kick-down, a strong negative vortex is formed during the kick-up motion in spite of the slow kick-up speed. This occurs because the large pressure difference between the upper and lower surfaces was created by the increase in relative velocity at the edge of the monofin, and the remarkably strong downwash generated by the fast kick-down motion.

Figures 6.5, 6.6, and 6.7 show the three-dimensional vortex structure around the monofin for the standard, fast kick-up 1, and fast kick-down 1 cases, respectively. In these figures, the green regions show the iso-surface of the nondimensional Q value ($|Qc^2/Uo^2| = 4$). In the right column, the vector indicates the velocity in the x - z plane at $y = 0$ mm. For the standard case, two vortex rings exist in the wake of the monofin at $t' = 0$. The vortex ring shed from the monofin (Fig. 6.5 (a) blue dotted line) was generated during the kick-down in the previous cycle. The vortex ring attached to the surface of the monofin (Fig. 6.5 (a) white dotted line) was created during the kick-up motion in the previous cycle. Monofin oscillation produced a chain of linked vortex rings in the wake. During the kick-down, a vortex ring is produced on the upper surface of monofin along the edge (Fig. 6.5 (b) red dotted line). This vortex ring is perpendicular to the freestream direction. Hence, propulsive force is hardly created during the kick-down. During the kick-up motion, the vortex ring grows on the lower surface of monofin (red dotted line in Fig. 6.5 (d)). This vortex ring is slightly inclined with respect to the freestream direction. In other words, the vortex ring on the lower surface of the monofin during kick-up has the momentum in the downstream direction. The monofin yields the propulsive force by generating the vortex ring with the momentum in the downstream direction. Furthermore, the vortex ring generated by kick-down motion remains on the upper surface of the monofin (white dotted line in Fig. 6.5 (d)). For the fast kick-up 1 case, the monofin during kick-down produces the inclined vortex ring (Fig. 6.6 (b) blue dotted line) with respect to the freestream, which induces strong flow in the

freestream direction (Fig. 6.6 (b) right column). At $t' = 0.58$, the vortex ring created during kick-down stretches in the downstream direction (Fig. 6.6 (d) red dotted line), because the time during the kick-down motion is long. Similar to the standard case, the inclined vortex ring, with respect to the freestream direction, is generated along the edge on the lower surface of the monofin during kick-up motion (dotted line in Fig. 6.6 (f)), and its circulation is larger than that for the standard case (the negative vorticity in Fig. 6.4 (a) and (b)). Therefore, the high propulsive force generated during kick-up is obtained by forming the inclined vortex ring with a large momentum in the downstream direction. For the fast kick-down 1 case, the vortex ring generated by the kick-down motion exists near the monofin at the lower dead point of oscillation ($t' = 0.33$). This vortex ring induces strong downwash on the upper surface of the monofin (Fig. 6.7 right column). During kick-up, the monofin gains high propulsive force from the enhancement of the pressure difference at the upper and lower surface of the monofin. This is caused by the increase in relative velocity between strong downwash and the monofin.

The results of the experiment show that oscillating motion with different kicking speeds, in kick-up and kick-down movements enhances the maximum propulsive force compared to the standard case. This occurs because the vortex ring on the lower surface of the monofin becomes stronger during kick-up motions. Furthermore, in the case of fast kick-down, the duration of the kick-down motion becomes shorter, meaning that the drag force during one oscillating cycle can be suppressed. It was concluded that the high propulsive force generated during one oscillating cycle is yielded for the fast kick-down 1 case.

6.3 Conclusions

To investigate the influence of oscillating motion on the propulsive force and the three-dimensional vortex structure around the monofin, three types of motion were examined. The findings of the present study are

summarized as follows.

1. Oscillating motion with different kick-up and kick-down speeds enhances the maximum propulsive force compared to the standard case. Furthermore, the propulsive force generated during one oscillating cycle for the fast kick-down 1 case is the highest among the five cases. This is because the negative propulsive force generation time during kick-down is short.
2. During the kick-up motion, the inclined vortex ring with respect to the freestream is generated on the lower surface. The strength of the vortex on the lower surface of the monofin during the kick-up was increased as the velocity difference between kick-up and kick-down is increase. The vortex on the lower surface enhances the maximum propulsive force.

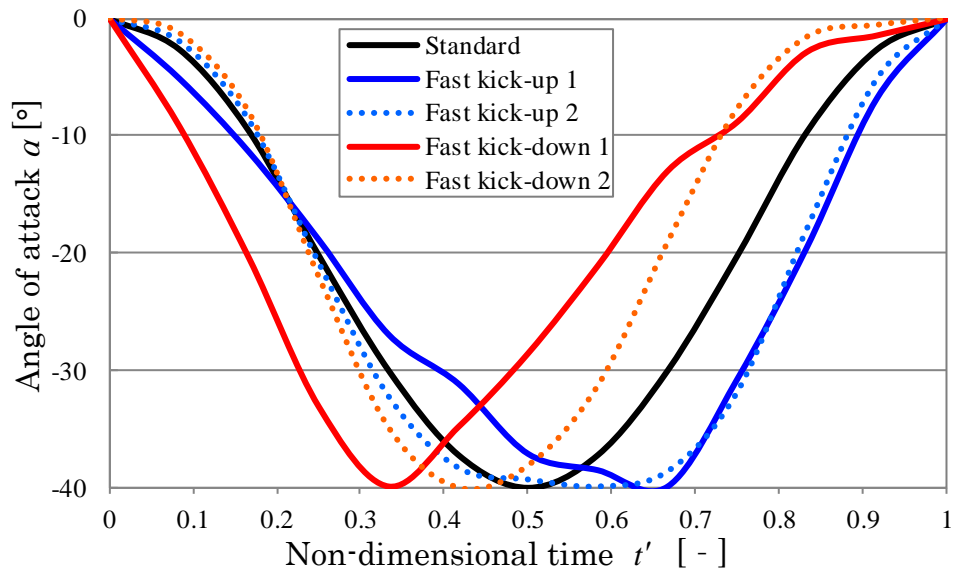


Fig. 6.1 The temporal change of α during oscillating motion

Table 6.1 Ratio of kick-up and kick-down speed

	kick-up speed : kick-down speed
standard	1 : 1
fast kick-up 1	2 : 1
fast kick-up 2	5 : 4
fast kick-down 1	1 : 2
fast kick-down 2	4 : 5

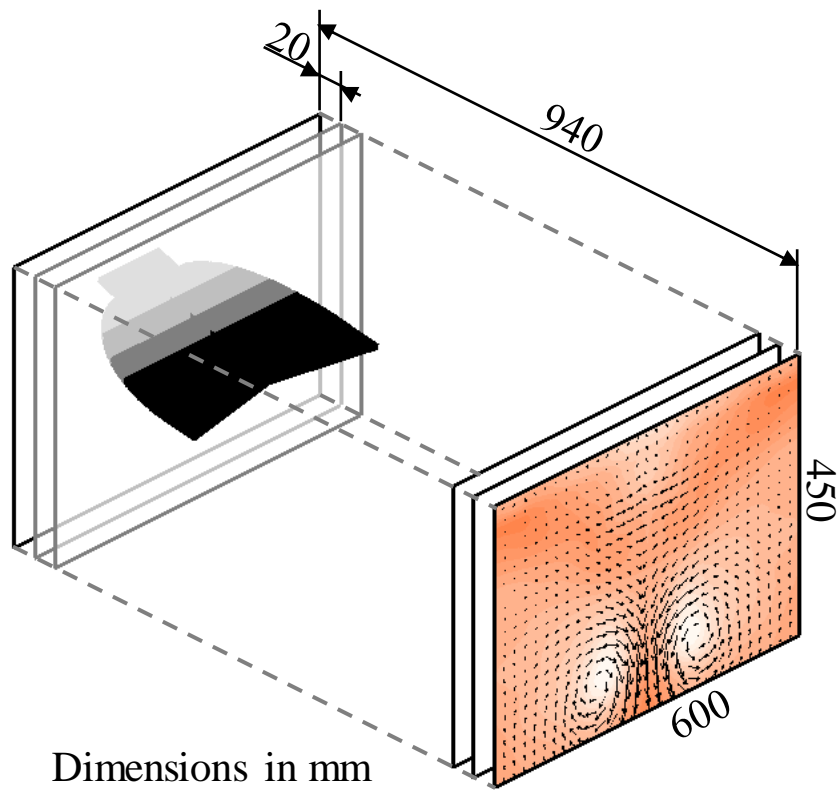


Fig. 6.2 Measurement region of stereoscopic PIV for the monofin

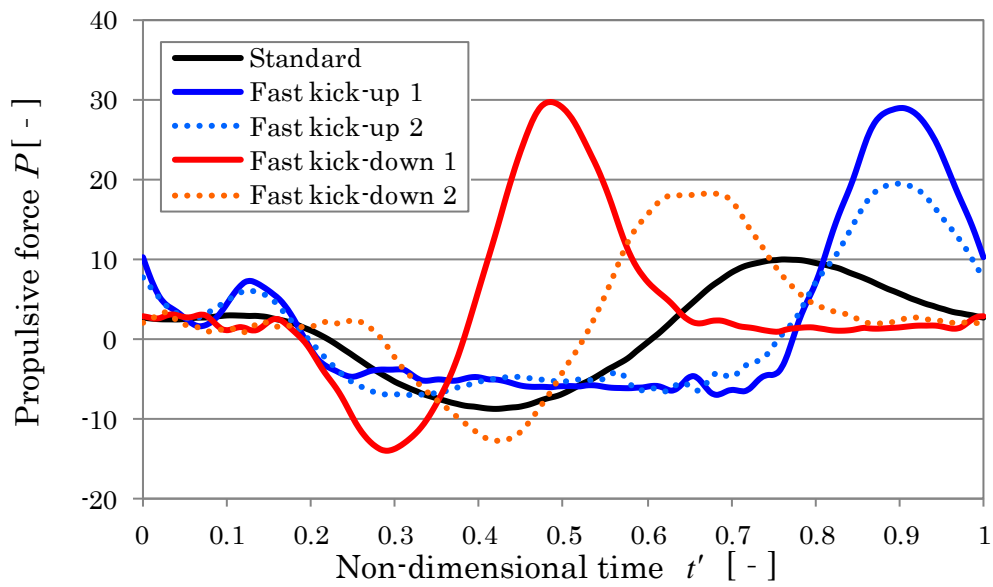
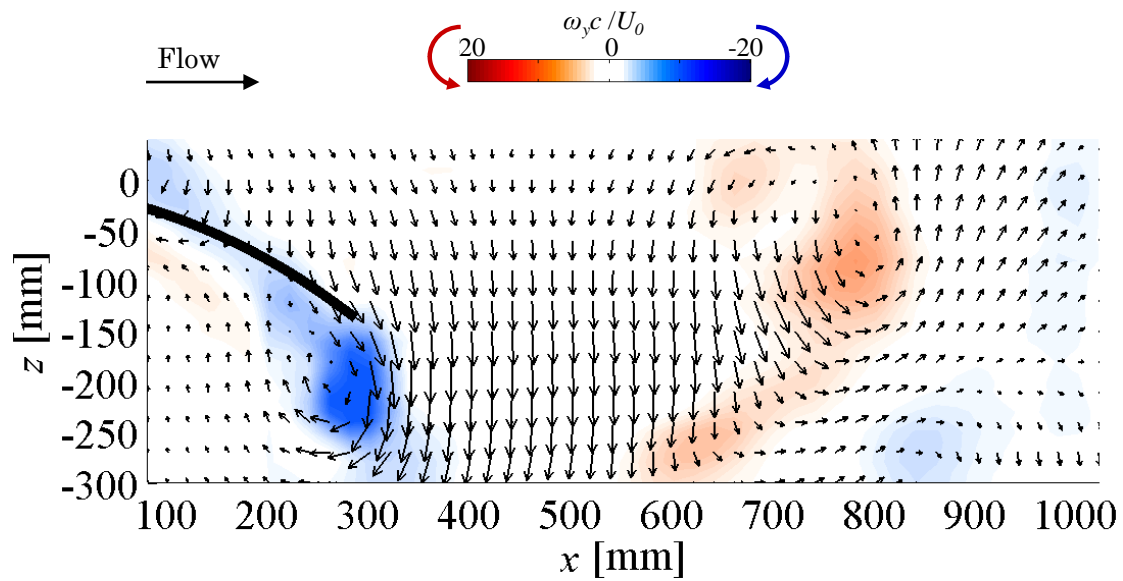
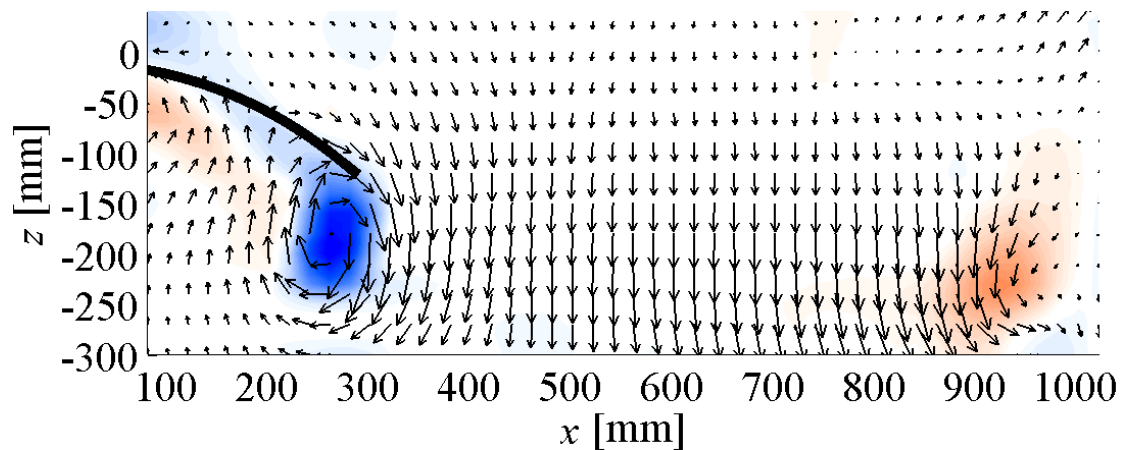


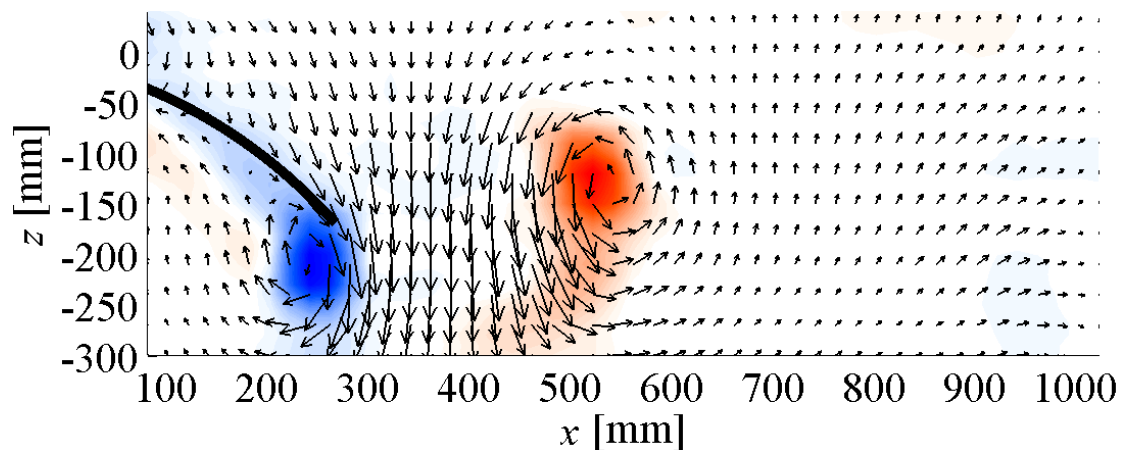
Fig. 6.3 Propulsive force variation during one kick stroke



(a) Standard



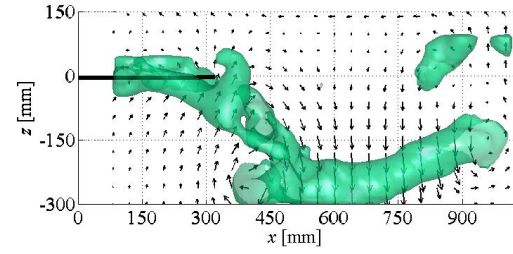
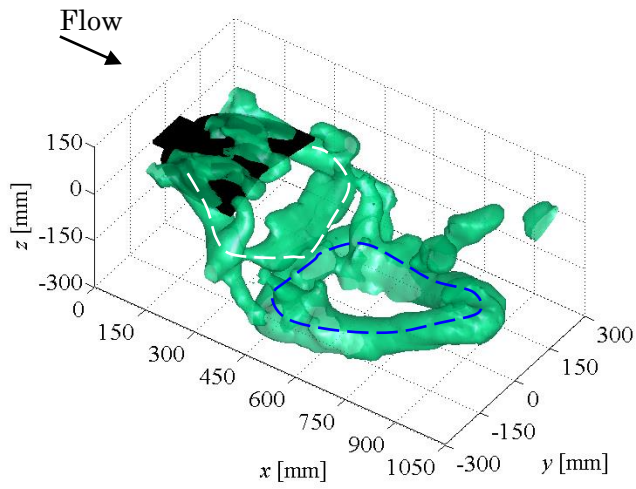
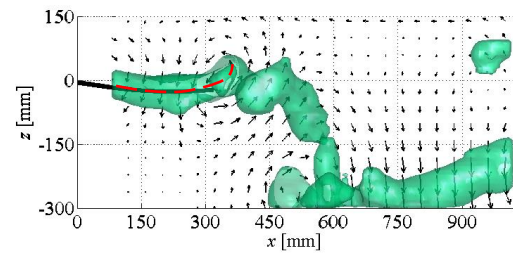
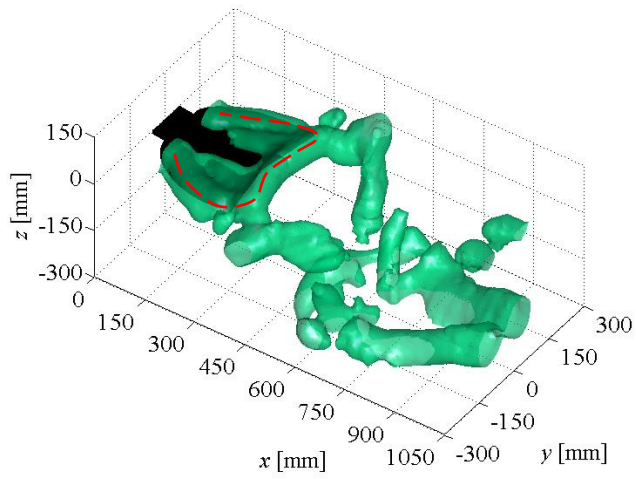
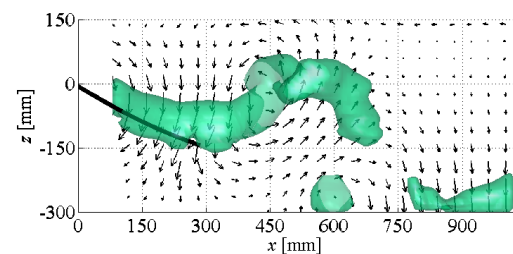
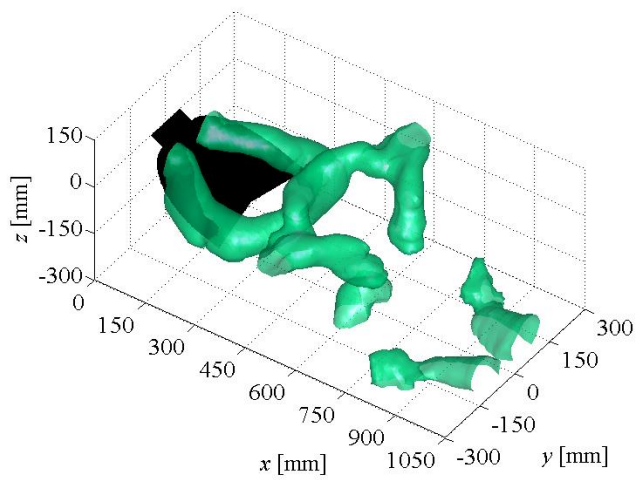
(b) Fast kick-up 1



(c) Fast kick-down 1

Fig. 6.4 Contour map of vorticity and velocity vectors in the x - z plane ($y = 0$ mm) at the time immediately after the propulsive force reaches its maximum value

$$Qc^2 / U_0^2 = 4$$

(a) $t' = 0$ (b) $t' = 0.17$ (c) $t' = 0.33$

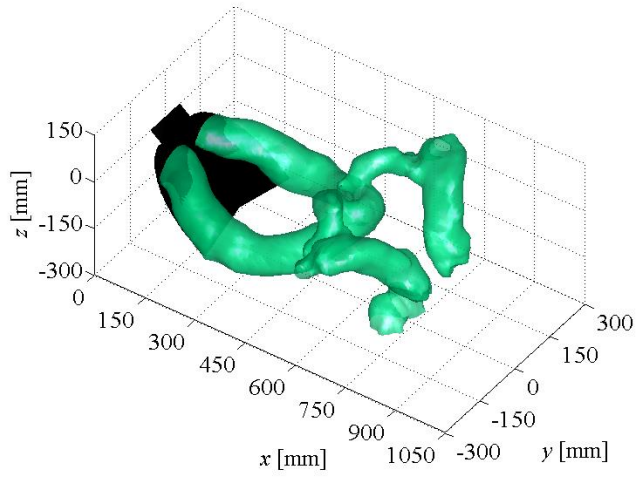
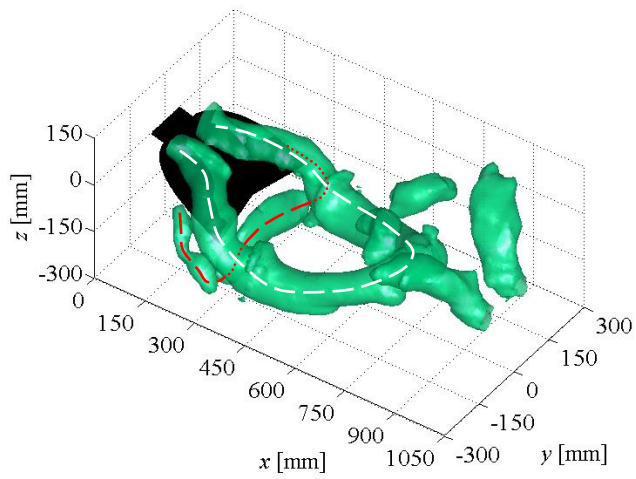
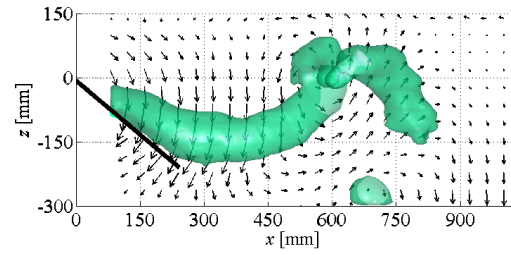
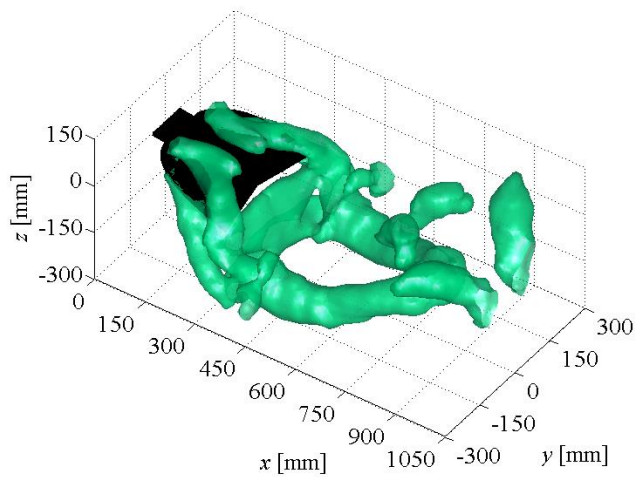
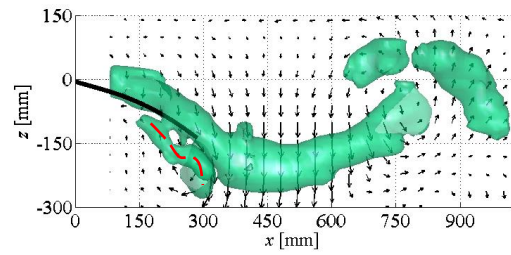
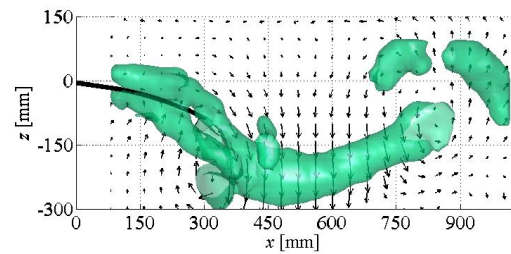
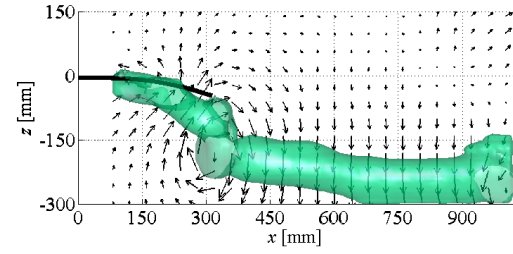
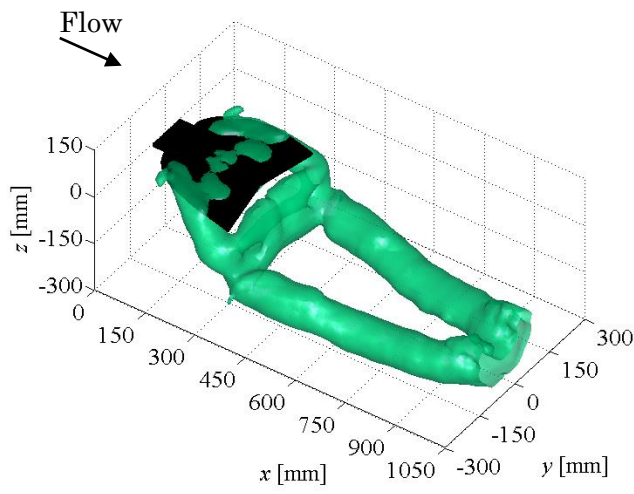
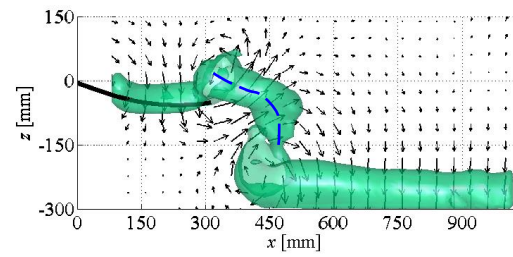
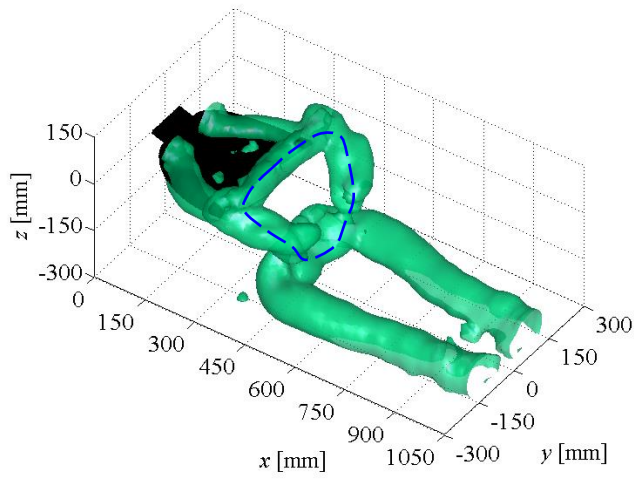
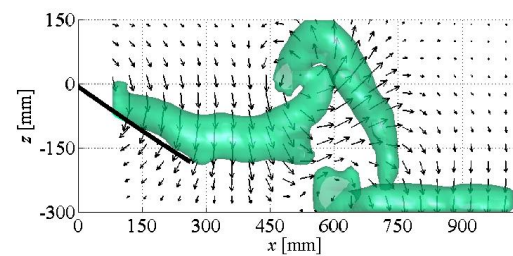
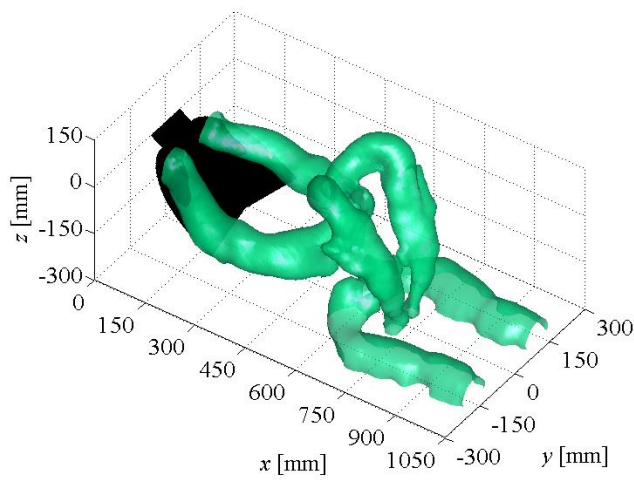
(d) $t' = 0.5$ (e) $t' = 0.75$ (f) $t' = 0.83$ 

Fig. 6.5 Three-dimensional vortex structure for the standard case

$$Qc^2 / U_0^2 = 4$$

(a) $t' = 0$ (b) $t' = 0.17$ (c) $t' = 0.42$

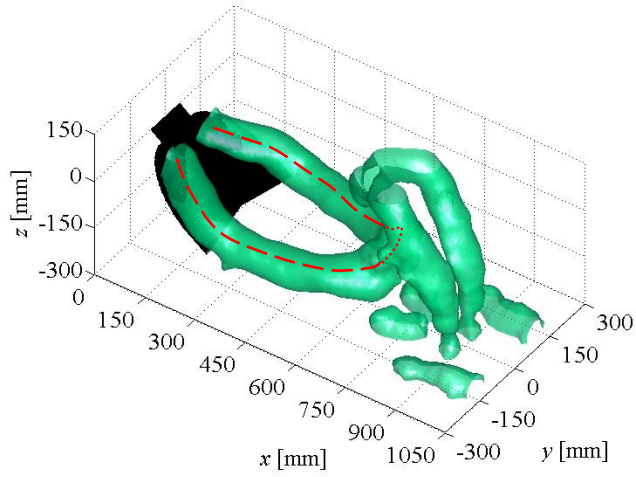
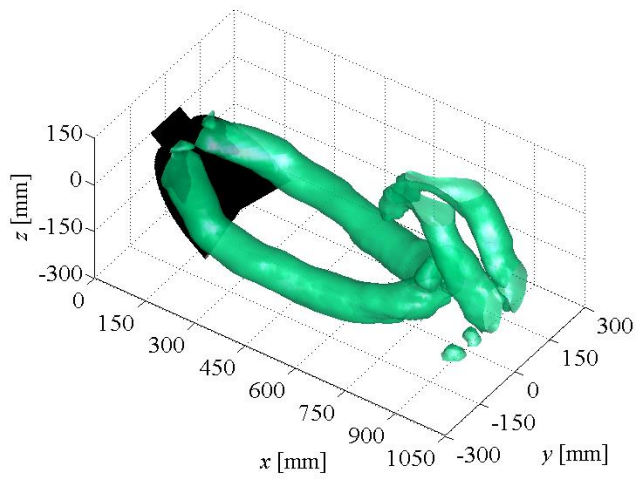
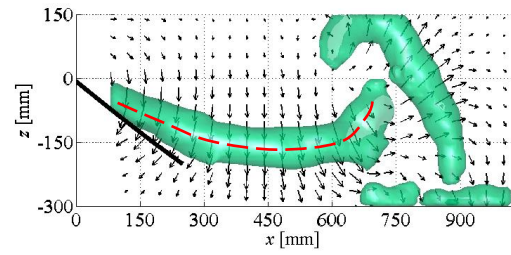
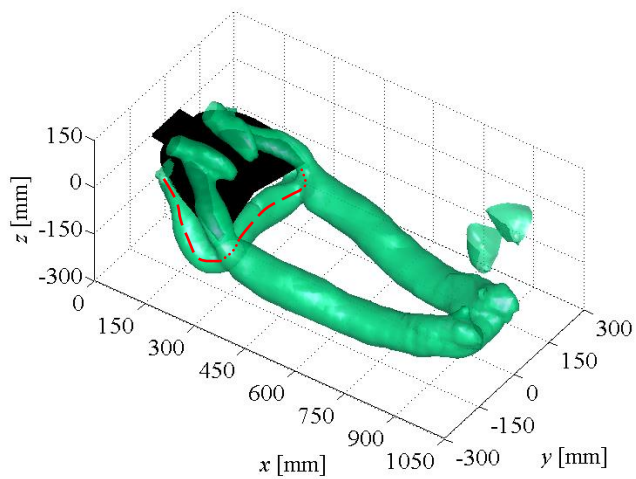
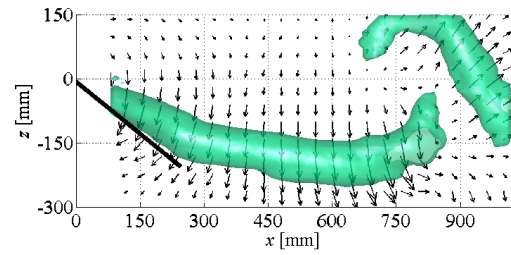
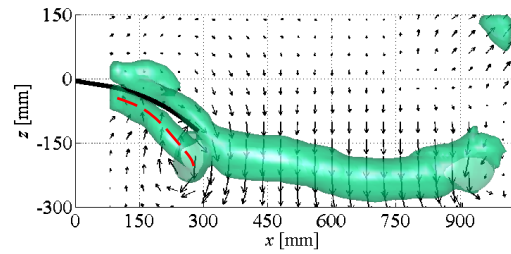

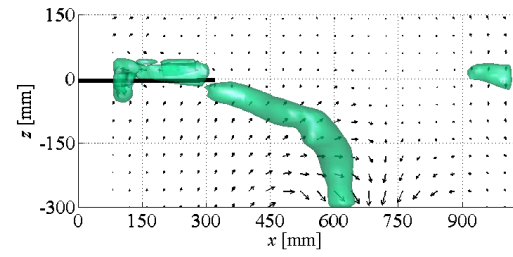
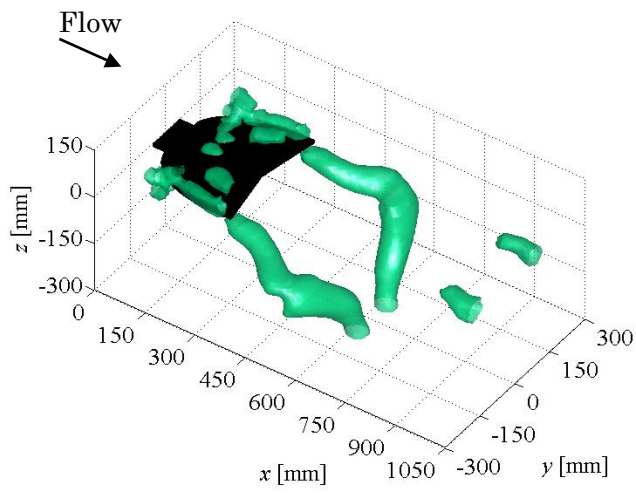
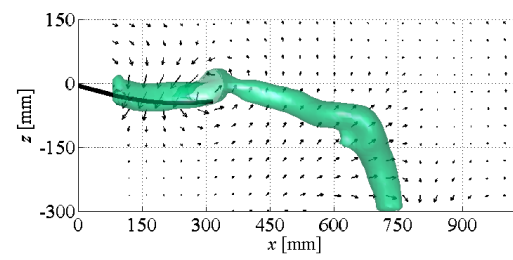
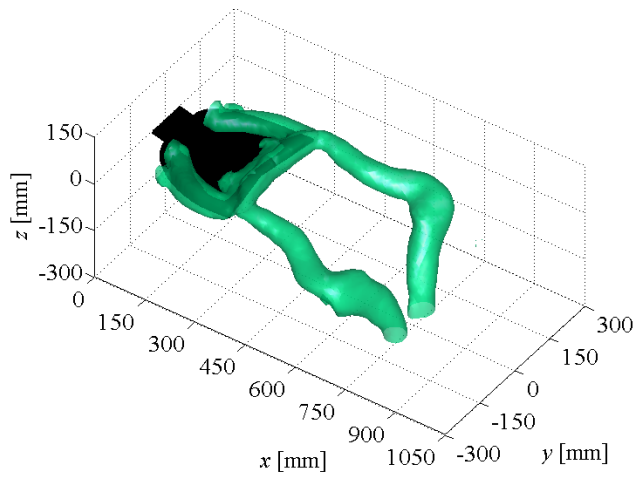
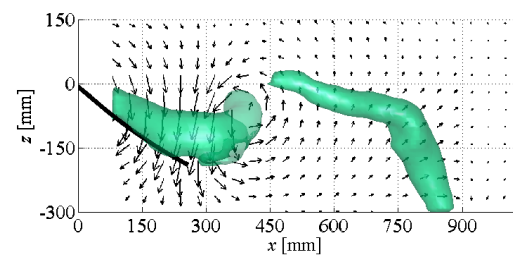
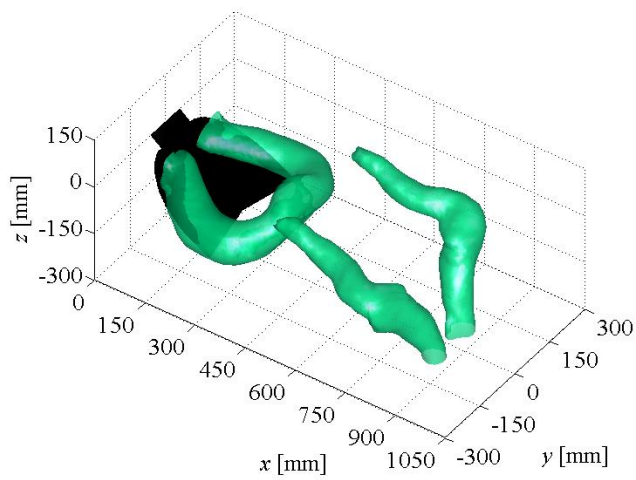
(d) $t' = 0.58$ (e) $t' = 0.75$ (f) $t' = 0.92$ 

Fig. 6.6 Three-dimensional vortex structure for the fast kick-up 1 case

 $Qc^2 / U_0^2 = 4$

(a) $t' = 0$ (b) $t' = 0.17$ (c) $t' = 0.33$

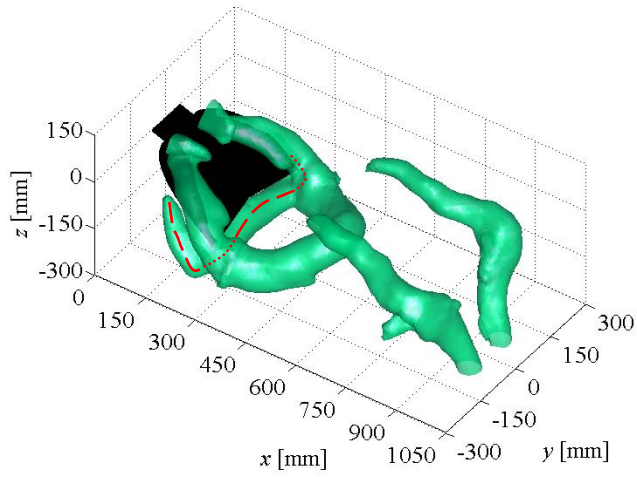
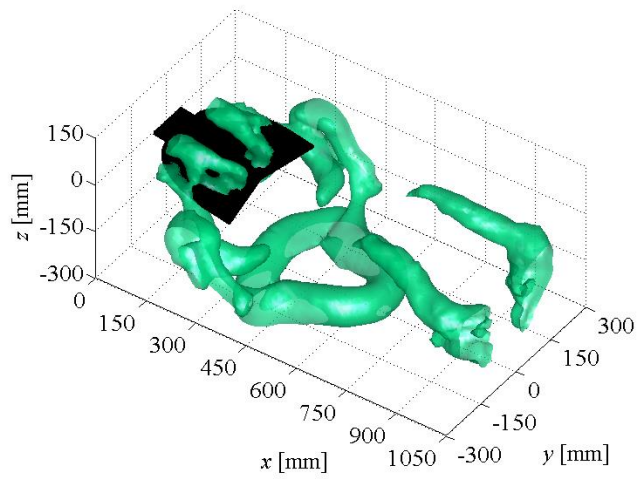
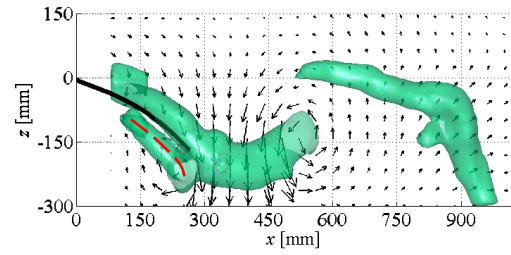
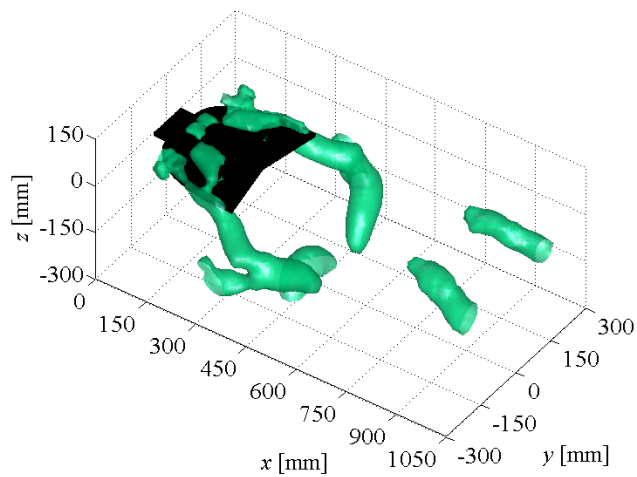
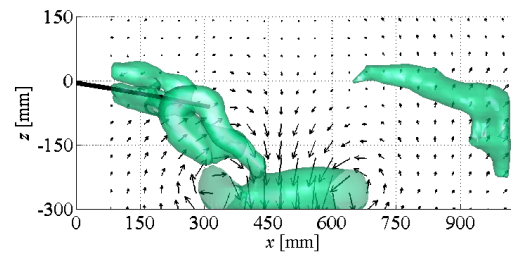
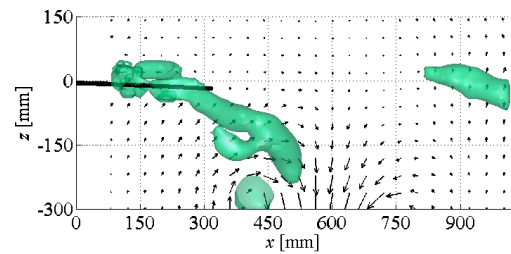
(d) $t' = 0.5$ (e) $t' = 0.67$ (f) $t' = 0.83$ 

Fig. 6.7 Three-dimensional vortex structure for the fast kick-down 1 case

7. PROPULSIVE FORCE CALCULATION BASED ON VORTEX RING

To clarify the relationship between the unsteady fluid force and the vortex ring, and to investigate the influence of the vortex ring position on the propulsive force with regard to the monofin, the propulsive forces acting on the monofin were calculated by using the momentum of the vortex ring. The propulsive force estimations were applied to the vortex ring, which was explained in Chapter 6.

7.1 Experimental Method

7.1.1 Theory of Propulsive Force Calculation

The momentum of the vortex ring is

$$M = \rho \Gamma A, \quad (7.1)$$

where ρ is the density of the water, Γ is the circulation of the vortex ring, and A is the area surrounded by the vortex line. The force is the time variation of the momentum,

$$\begin{aligned} F &= \frac{d}{dt} M \\ &= \rho \frac{d}{dt} (\Gamma A), \end{aligned} \quad (7.2)$$

where ρ is constant.

Given that the circulation and area changes with respect to time, the resultant fluid force generated by the vortex ring (Dickinson (1996)) [16] is expressed by

$$F = \rho \left(\Gamma \frac{dA}{dt} + A \frac{d\Gamma}{dt} \right). \quad (7.3)$$

The propulsive force, F_x , and the force in the heightwise direction, F_z , are

$$F_x = F \sin \left(\arctan \left(\frac{A_x}{A_z} \right) \right) \quad (7.4)$$

and

$$F_z = F \cos \left(\arctan \left(\frac{A_x}{A_z} \right) \right), \quad (7.5)$$

respectively, where A_x , and A_z are the profile areas in the x and z direction of the vortex ring, respectively.

7.1.2 Area Calculation of Vortex Ring

Muller et al. [12] and Epps et al. [13] assumed that the vortex ring is a simple circular shape with a diameter equal to the distance between the vortex pair in a two-dimensional plane. However, the three-dimensional structure of an actual vortex ring is more complex (Fig. 6.6). A more accurate calculation of the vortex ring area was performed by Imamura et al. (2013), who clarified the three-dimensional structure of the vortex ring in the wake of the oscillating fin. In this study, the area calculation of the vortex ring was performed using a method similar to that used by Imamura et al. [15]. We estimated the fluid force not only from the vortex ring attached to the monofin, but also from the shed vortex ring. Figure 7.1 shows the method of detection used for the vortex line. The 36 mesh grids perpendicular to the horizontal plane were created at equal intervals of 10° [15] around the point defined as center of the vortex ring (Fig. 7.1). The vorticities in each mesh grid were calculated using linear interpolation. The centers of the vortex core in each mesh grid were detected as a peak of the vorticity in the plane. By connecting the vortex center in each plane, the area of the vortex ring is defined as a polygon. As seen Fig. 7.2 (a) and (b), the time varying profile

areas A_x and A_z , are calculated, respectively.

7.1.3 Circulation Calculation of Vortex Ring

Imamura et al. (2013) assumed that circulation is constant over the entire vortex ring, and the vortex ring circulation was estimated by integrating the region of interest to the vortex in the central plane of the fin (at $y = 0$ in the $x-z$ plane). However, this procedure led to an overestimation of propulsive force. The problem with the assumption was determined to be that circulation is not constant over the entire vortex ring [15]. Thus, in this study, to calculate the circulation of the entire vortex ring, the following procedure is used. The mesh grids perpendicular to the vortex ring were created (Fig. 7.3) at each vortex center detected in the Section 7.1.2, and the vorticities in each mesh grid were calculated using linear interpolation. Vortex circulations in each plane were computed by Stokes theorem. The large vorticity area integration causes higher total circulation. Hence, the vorticities greater than the 25 % of the maximum vorticity were integrated. Figure 7.4 shows the circulation calculated by Stokes theorem with respect to the threshold percentage of the maximum vorticity by way of an example. The slope of a line in Fig 7.4 changes when the threshold level is below approximately 20 %, because low-level vorticities were summed over a large area. A similar trend was observed in the majority of vortex rings. Finally, the circulation of the entire vortex ring circulation was calculated by averaging the circulation in each plane.

7.2 Results and Discussion

In general, it is known that propulsive forces are generated as the result of creating and shedding of the vortex ring with momentum (Ito (2015) [38]). The time-averaged propulsive forces from the elliptical vortex ring in a

fish wake were evaluated by Nauen et al. (2002), and its values are not significantly different than the drag force measured by towing a fish body [14]. On the other hand, Imamura et al. (2013) estimated the time varying propulsive force from the vortex ring attached to the monofin surface. They showed that the measured and estimated propulsive force variations have the same behavior and value, but the calculated maximum propulsive force [15] is over three times higher than the measured value [39]. The effect of the relative position of the vortex ring to the monofin on the time varying propulsive force has not been argued. In this study, we investigated which vortex ring (e.g. attached to, connected to, or shed from the monofin) affects propulsive force generation. An "attached ring" is a vortex ring that grows on the surface of monofin (e.g. red dotted line in Fig. 6.5 (a), (b) and (e)). A "connected ring" is defined as a vortex ring connected to the monofin in spite of the other vortex ring generation on the surface of monofin, i.e. the remaining vortex ring on the monofin (e.g. white dotted line in Fig. 6.5 (e)). A "shed ring" is a vortex ring shed from the monofin (e.g. blue dotted line in Fig. 6.5 (a)). Figure 7.5 shows the propulsive force calculated from the momentum of a vortex ring with respect to the nondimensional time. The blue, red, and green lines in this figure indicate the estimated propulsive force from the "attached ring", "attached ring" + "connected ring" and all vortex rings ("attached ring" + "connected ring" + "shed ring"), respectively. The measured propulsive force is shown by the black line for comparison purposes. For the propulsive force calculated from the "attached ring," a large peak is observed $t' = 0.79$. This exists because the vortex ring was generated on the lower surface of monofin during kick-up. In comparison to the measured propulsive force, the variation of propulsive force for the "attached ring" has same tendency. The averaged and maximum forces calculated from the "attached ring" during one cycle are approximately 1.9 and 1.3 times as high as those for the measured propulsive force, respectively. The curve of force calculated from the "attached ring" and "connected ring" has a significantly large peak during kick-up. This is because the vortex ring

with momentum in upstream direction on the upper surface of monofin (white dotted line in Fig. 6.5 (e)) breaks down, in addition to the propulsive force generation caused by growing the vortex ring on the lower surface (red dotted line in Fig. 6.5 (e)). That is, the decrease in momentum in the upstream direction appeared as the propulsive force. However, the maximum propulsive force generated during kick-up was overestimated in comparison with the measured value, because the vortex ring on the upper surface of the monofin contributes to the vortex ring growth on the lower surface of monofin during kick-up. The vortex ring on the upper surface induces downward flow on the upper surface of monofin (Fig. 6.5 (c)-(e) right column). The strength of the vortex ring strength on the lower surface of the monofin was enhanced by the increase in relative velocity between the monofin tip and the downward flow. Furthermore, a significantly negative value was observed just after the upper dead point of motion. This value exists because the vortex ring, which created the high propulsive force during kick-up, is dissipated by the viscous effect and A_x decreases after the kick-up motion. In eq. (7.3), the viscous effect was not considered. Thus, the decrease in momentum in the downstream direction due to the viscous effect appears as a negative force. For the propulsive force calculated for all of the vortex rings in the measurement region (green dotted line in Fig. 7.5), negative force was observed during the fast half of the kick-up motion. This is because the vortex ring strength decreases (because of viscous effects) after the vortex ring shed in the wake of the monofin. The estimated propulsive force, including the "connected ring" or "shed ring," were significantly different from the measured propulsive force. The difference between the calculated mean propulsive force and the measured propulsive force is small in comparison with that by Imamura et al. (2011) and (2013) [15, 39]. However, the value of estimated mean propulsive force during one oscillation cycle was 1.9 times as high as the measured value. This is because the drag force in the estimated propulsive force curve was calculated to be smaller than that in the measured propulsive force curve. During kick-down, the vortex ring on

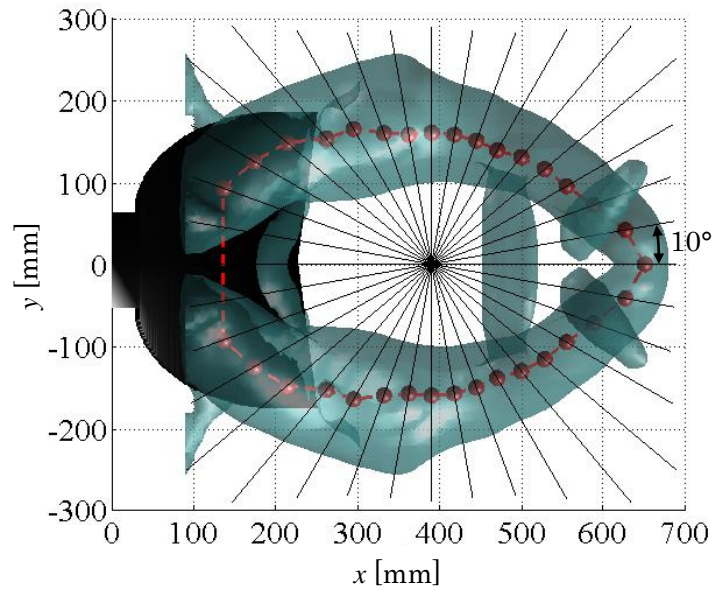
the upper surface of the monofin bends into a 'U' shape (e.g. Fig. 6.5 (d) right column). The upstream side of the 'U' shaped vortex ring (blue solid line in Fig. 7.6) induces the flow in the upstream direction, and the downstream side (red solid line in Fig. 7.6) produces the flow in the downstream direction. Thus, A_x is estimated as the difference in the profile area in the x -direction of the upstream side, A_{xu} (surrounded by blue solid line in Fig. 7.2 (a)), and the downstream side, A_{xd} (surrounded by red solid line in Fig. 7.2 (a)), of the vortex ring. That is, A_{xu} is calculated to be smaller than the actual area because the flow fields near the leading edge were not measured (blue dotted line in Fig. 7.6). As a result, the drag force during kick-down was underestimated. If it is assumed that the 'U' shaped vortex ring is generated from the leading edge, the averaged propulsive force calculated from "attached ring" during one cycle becomes 1.3 times as large as the measured value. Therefore, the propulsive force acting on the monofin can be estimated from the flow field (including the region near the leading edge) by calculating the propulsive force based on the vortex ring attached to the surface of monfin.

7.3 Conclusions

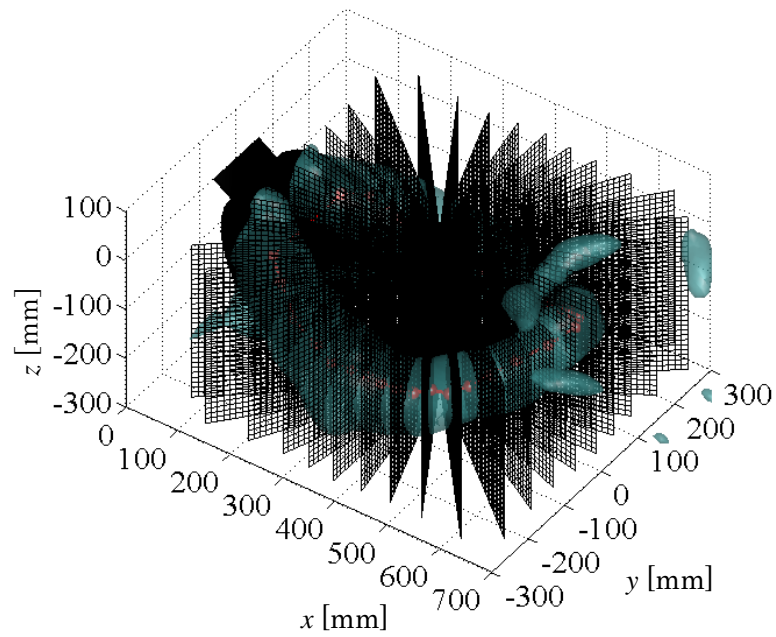
To investigate the relationship between the propulsive force and the vortex ring generated in the wake of a monofin, the propulsive force was estimated from the vortex ring. The main conclusions of this experiment are summarized as follows:

1. The propulsive force calculation, including the "connecting ring," overestimated the peak value during kick-up compared to the measured value.
2. The significantly negative force at the upper dead point of oscillation was observed in the propulsive force curve calculated from all vortex rings in the measurement region.

3. The propulsive force acting on the monofin can be estimated from the flow field, including the region near the leading edge, by calculating the propulsive force based on the vortex ring attached to the surface of the monofin.



(a) Top view



(b) Perspective view

Fig. 7.1 Detection of vortex line

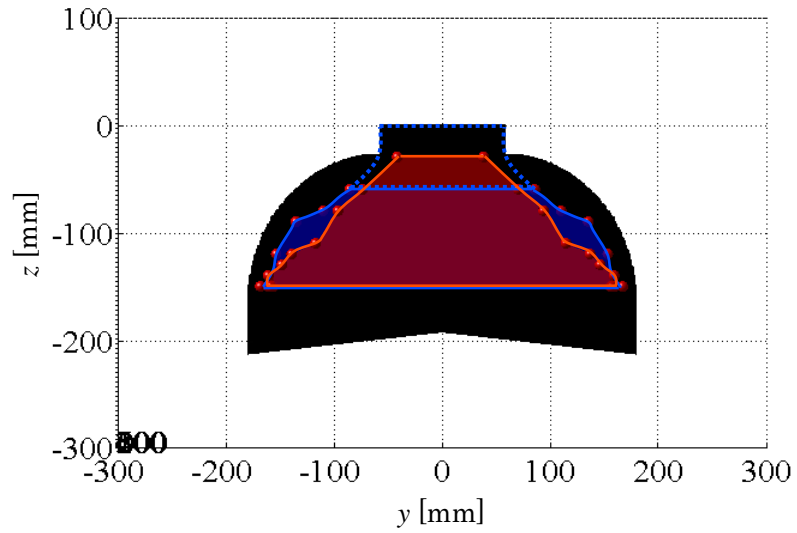
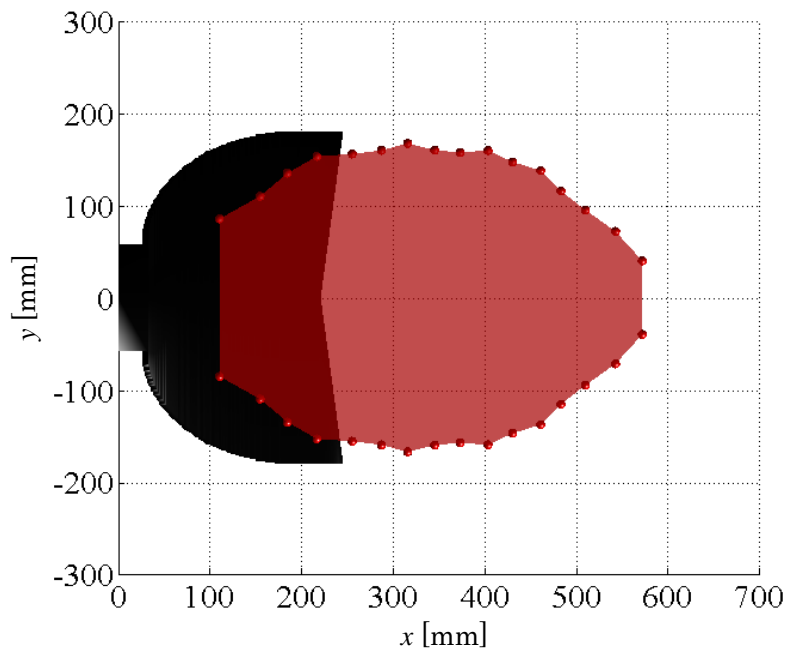
(a) Profile area in the x -direction A_x (b) Profile area in the z -direction A_z

Fig. 7.2 Calculation of vortex ring profile area

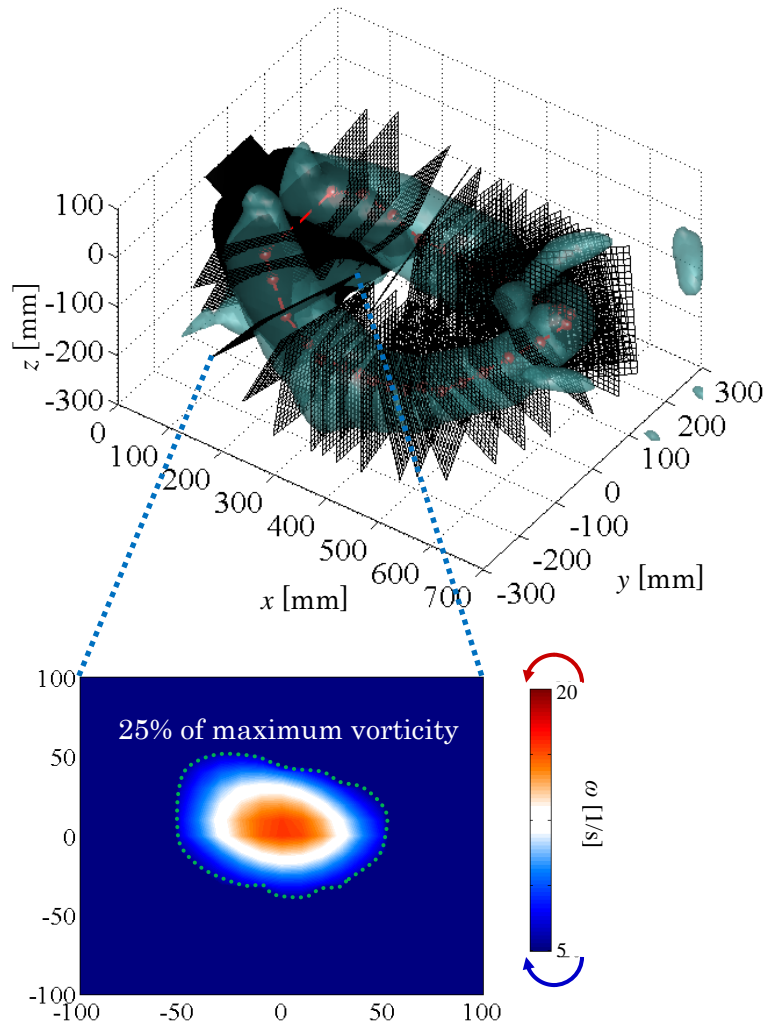


Fig. 7.3 Calculation of vortex ring circulation

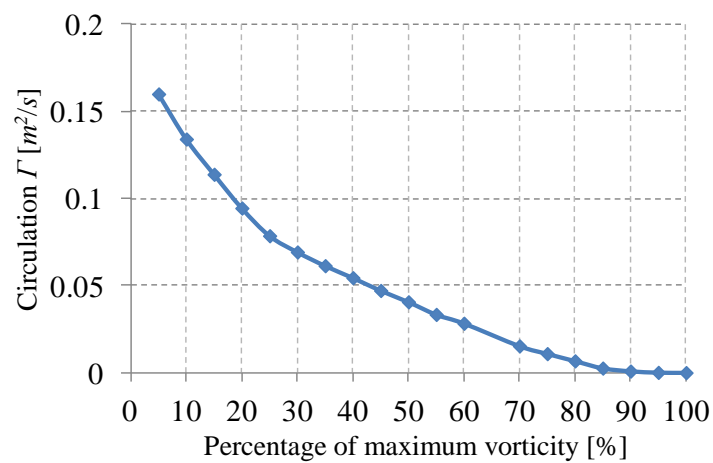


Fig. 7.4 Circulation calculated by Stokes theorem with respect to the threshold percentage of the maximum vorticity

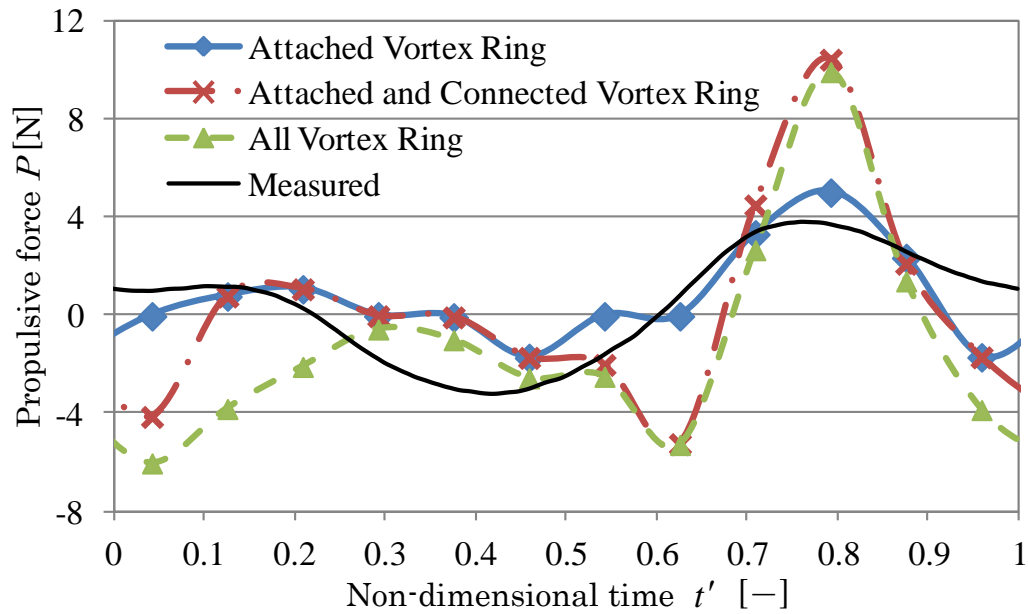


Fig. 7.5 Propulsive force calculated from vortex ring in the wake of the monofin

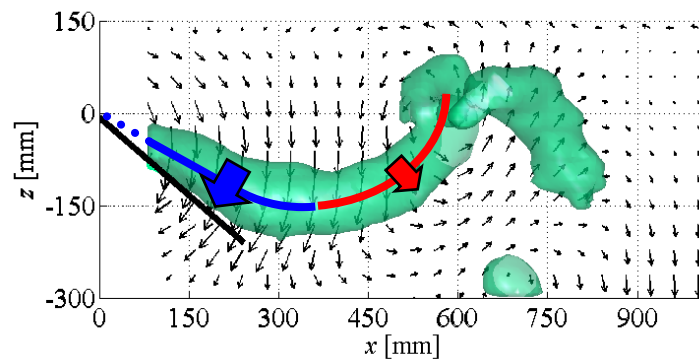


Fig. 7.6 Contribution of the upstream and downstream sides of a vortex ring to the momentum in the freestream direction

8. SUMMARY

Experimental studies on the unsteady phenomenon generated by an oscillating model were performed. The flow fields were measured using Stereoscopic PIV, which was applied at several downstream positions, and three-component velocity measurements were synchronized to the model movements to clarify the three-dimensional vortex structure around the model. To understand the fundamental relationship between unsteady fluid force and three-dimensional vortex structure, the three-dimensional airfoil was subjected to impulsive incidence variation of its angle of attack. The effect of the difference in the airfoil shape and oscillating motion on the unsteady fluid force and the three-dimensional vortex structures were investigated. Furthermore, we attempted to estimate the propulsive forces acting on the monofin by using the momentum of the vortex ring to clarify the effect of its relative position to the monofin on the time-varying propulsive force.

1. Stall delay is observed for the upward movements of the discoid and triangular airfoil, and the maximum lift coefficient is greater than that under the stationary condition. For the discoid airfoil, C_L gradually decreases after the airfoil stops moving. For the triangular airfoil, C_L decreases rapidly immediately after the triangular airfoil stops moving. The unsteady effect on the unsteady lift and flow field generated during impulsive incidence variation is greater for the discoid airfoil than for the triangular airfoil.
2. The fluid force increases as a vortex grows near the airfoil. The peak value of the fluid force for Type-2 oscillation is larger than that for Type-1 oscillation. For Type-2 oscillation, a strong vortex exists close to the airfoil over a prolonged period of time.

3. The fluid force from the discoid airfoil throughout one pitch-oscillating cycle becomes larger compared to that from the rectangular airfoil. This occurs because the vortex exists over a prolonged period of time in the wake of the discoid airfoil.
4. Oscillating motion with different kicking speed in kick-up and kick-down enhances the maximum propulsive force compared to the standard case. During the kick-up motion, the inclined vortex ring with respect to the freestream is generated on the lower surface. The strength of the vortex on the lower surface of the monofin during kick-up was increased for the motion with different kick-up and kick-down kicking speeds.
5. The propulsive force calculated from the "attached ring" is most similar to the measured propulsive force. The propulsive force acting on the monofin can be estimated from the flow field, including the region near the leading edge, by calculating the propulsive force based on the vortex ring attached to the surface of monofin.

REFERENCES

- [1] Weis-Fogh, T., "Energetics of Hovering Flight in Hummingbirds and in *Drosophila*", *Journal of Experimental Biology*, Vol. 56 (1972), pp. 79-104.
- [2] Ellington, C. P., "The Aerodynamics of Hovering Insect Flight. I. The Quasi-Steady Analysis", *Philosophical Transactions of the Royal Society of London. Series B, Biological sciences*, Vol. 305 (1984), pp. 1-15.
- [3] Gray, J., "Studies in Animal Locomotion VI. The Propulsive Powers of the Dolphin", *The Journal of Experimental Biology*, Vol. 13 (1936), pp.192-199.
- [4] Izumi K., and Kuwahara, K., "Unsteady Flow Field, Lift and Drag Measurements of Impulsively Started Elliptic Cylinder and Circular-Arc Airfoil", *Proceedings of AIAA 16th Fluid and Plasma Dynamics Conference*, AIAA -83-1711 (1983), pp.1-15.
- [5] Sana, S. P., "The Aerodynamics of Insect Flight", *The Journal of Experimental Biology*, Vol. 206 (2003), pp. 4191-4208.
- [6] Maxworthy, T., "Experiments on the Weis-Fogh Mechanism of Lift Generation by Insects in Hovering Flight. Part 1. Dynamics of the 'Fling'", *Journal of Fluid Mechanics*, Vol. 93, part 1 (1979), pp. 47-63.
- [7] Birch, J. M., Dickson, W. B., and Dickinson, M. H., "Force Production and Flow Structure of the Leading Edge Vortex on Flapping Wings at High and Low Reynolds Numbers", *The Journal of Experimental Biology*, Vol. 207 (2004), pp. 1063-1072.
- [8] Zhao, L., Deng, X., and Sane, S. P., "Modulation of Leading Edge Vorticity and Aerodynamic Forces in Flexible Flapping Wing", *Bioinspiration & Biomimetics*, Vol. 6 (2011), pp. 1-7.
- [9] Percin, M., and Oudheusden, B. W., "Three-Dimensional Flow Structures and Unsteady Forces on Pitching and Surging Revolving Flat Plates", *Experiments in Fluids*, Vol. 56, No. 47 (2015), pp. 1-19.
- [10] Fuchiwaki, M., Kuroki, T., Tanaka, K., Tababa, T., "Dynamic Behavior of the Vortex Ring Formed on a Butterfly Wing", *Experiments*

- in Fluids*, Vol. 54, No. 1450 (2013), pp. 1-12.
- [11] Flammang, B. E., Lauder, G. V., Troolin, D. R., and Strand, T. E., "Volumetric Imaging of Fish Locomotion", *Biology Letters*, Vol. 7 (2011), pp. 1-4.
- [12] Muller, U. K., Vav Den Heuvel, B. L. E., Stamhuis, E. J., and Videler, J. J., "Fish Foot Prints: Morphology and Energetics of the Wake Behind a Continuously Swimming Mullet (*Chelon Labrosus Risso*)", *The Journal of Experimental Biology*, Vol. 200 (1997), pp. 2893-2906.
- [13] Epps, B. P., and Techet A. H., "Impulse Generated during Unsteady Maneuvering of Swimming Fish", *Experiments in Fluids*, Vol. 43 (2007), pp. 691-700.
- [14] Nauen, J.C., and Lauder G. V., "Hydrodynamics of caudal fin locomotion by chub mackerel, *Scomber Japonicus* (Scombridae)", *The Journal of Experimental Biology*, Vol. 205 (2002), pp. 1709-1724.
- [15] Imamura, N., and Mastuuchi, K., "Relationship Between Vortex Ring in Tail Fin Wake and Propulsive Force", *Experiments in Fluids*, Vol. 54, No. 1605 (2013), pp. 1-13.
- [16] Dickinson, M. H., "Unsteady Mechanisms of Force Generation in Aquatic and Aerial Locomotion", *American Zoologist*, Vol. 36 (1996), pp.537-554.
- [17] Schleihauf, R., Gray, L., and DeRose, J., "Three-Dimensional Analysis of Hand Propulsion in the Sprint Front Crawl Stroke", *Biomechanics and Medicine in Swimming, Human Kinetics* (1983), pp. 173-183.
- [18] Berger, M. A. M., de Groot G., and Hollander A. P., "Hydrodynamic Drag and Lift Forces on Human Hand/Arm Models", *Journal of Biomechanics*, Vol. 28, No. 2 (1995), pp.125-133.
- [19] Matsuuchi, K., "Generating Mechanism of Propulsive Force by Pull Motion in Swimming", *Proceedings of Symposium on Sports Engineering, Symposium on Human Dynamics, The Japan Society of Mechanical Engineers* (2007), pp.188-193 (in Japanese).
- [20] Matsuuchi, K., Miwa, T., Nomura, T., Sakakibara, J., Shintani H., and Ungerechts, B. E., "Unsteady Flow Field Around a Human Hand and Propulsive Force in Swimming", *Journal of Biomechanics*, Vol. 42, No. 1 (2008), pp 42-47.
- [21] Hasegawa, H., Watanabe J., and Matsuuchi, K., "Effect of

- 3-Dimensional Airfoil Shape on Unsteady Fluid Forces in Pitching Motion", *Journal of Fluid Science and Technology*, Vol. 5, No. 2 (2010), pp 270-280.
- [22] Nakashima, S., Suzuki, S., and Nakajima, K., "Development of a Simulation Model for Monofin Swimming", *Journal of Biomechanical Science and Engineering*, No. 5, Vol. 4 (2010), pp. 408-420.
- [23] Gautier, J., Baly, L., Zanone, P. G., and Watier, B., "A Kinematic Study of Finswimming at Surface", *Journal of Sports Science and Medicine*, Vol. 3 (2004), pp. 91-95.
- [24] Nicolas, G., and Bideau, B., "A Kinematic and Dynamic Comparison of Surface and Underwater Displacement in High Level Monofin Swimming", *Human Movement Science*, Vol. 28 (2009), pp. 480-493.
- [25] Arellano, R., Pardillo, and S., Gavilan, A., "Underwater Undulatory Swimming: Kinematic Characteristics, Vortex Generation and Application During the Start, Turn and Swimming Strokes", *Proceedings of the XXth International Symposium on Biomechanics in Sports – Swimming* (2002), pp. 1-12.
- [26] Nicolas, G., Bideau, B., Colobert, B., and Berton, E., "How are Strouhal Number, Drag, and Efficiency Adjusted in High Level Underwater Monofin Swimming?", *Human Movement Science*, Vol. 26 (2007), pp. 426-442.
- [27] Haniu, T., Hasegawa, H., "Vortex Flow around a Three-Dimensional Airfoil during Impulsive Incidence Variation", *Proceedings of the 6th International Conference on Vortex Flows and Vortex Models* (Nagoya, Japan), (2014), pp. 1-5.
- [28] Haniu, T., Hasegawa, H., Nakagawa, K., "Vortex Shedding from a Pitch-Oscillating Discoid Airfoil", *Journal of the Japanese Society for Experimental Mechanics*, Vol.14, No. Special_Issue (2014), pp. s71-s75.
- [29] Haniu, T., Hasegawa, H., Takagi, H., Shimojo, H., "Stereoscopic PIV Measurements of Three-dimensional Vortex Structure in the Wake of a Monofin", *Proceedings of 11th International Symposium on Particle Image Velocimetry – PIV'15* (Santa Barbara, CA, USA) (2015), pp. 1-5.
- [30] Haniu, T., Hasegawa, H., "Stereo PIV measurements of vortex behavior produced by a pitch-oscillating discoid airfoil", *Journal of Fluid Science and Technology*, Vol. 9, No. 3 (2014), pp. 1-8.
- [31] Haniu, T., Hasegawa, H., "Three-dimensional Vortex Structure using

- Phase-averaged Stereoscopic PIV for an Oscillating Airfoil", *Journal of Visualization*, Vol. 18, Issue 3 (2015), pp. 553-561.
- [32] Miura, H., and Kida, S., "Vortex Tube Dynamics in Turbulence", *Research Institute for Mathematical Sciences Kokyuroku*, Vol. 1029 (1998), pp. 121-130.
- [33] Aihara, Y., Koyama, H., and Murashige, A., "Transient Aerodynamic Characteristics of a Two-Dimensional Airfoil During Stepwise Incidence Variation", *Journal of Aircraft*, Vol. 22, No. 8 (1985), pp. 661-668.
- [34] Hasegawa, H., Shimakawa, T., Matsuuchi, K., and Nakagawa, K., "Transient Vortex Structure of a Discoid Airfoil During Impulsive Incidence Variation", *Journal of the Visualization Society of Japan*, Vol. 34, No. 6 (2014), pp. 9-16 (in Japanese).
- [35] Azuma, A., "Fluid dynamics, *Asakura Publishing Co., Ltd* (1993), pp. 20-21 (in Japanese).
- [36] Arita, R., Kase, A. and Ohba, K., "Experiments of an Enlarged Realistic Flapping Wing Model for Elucidating Mosquito's Flight", *The Japan Society of Mechanical Engineers, Series B*, Vol. 79, No. 775 (2011), pp. 823-831 (in Japanese).
- [37] Luersen, M. A., Riche, R. L., and Maitre, O. L., "A Computationally Efficient Approach to Swimming Monofin Optimization", *Structural and Multidisciplinary Optimization*, No. 31 (2006), pp. 488-496.
- [38] Ito, S., "Vortex rings and the reaction forces occurring at flight or swimming occasion concerning creatures", *Research Institute for Mathematical Sciences Kokyuroku*, Vol. 1900 (2014), pp. 26-36 (In Japanese).
- [39] Imamura, N., and Matsuuchi, K., "Visualization of the Three-dimensional Vortex Structure in the Wake of an Oscillating Wing of a Fin Type", *Proceedings of 9th International Symposium on Particle Image Velocimetry – PIV'11* (Kobe, Japan) (2011), pp. 1-4.

APPENDIX A: LIST OF USED : SYMBOLS

x, y, z	Cartesian coordinates
u, v, w	velocity components
$\omega_x, \omega_y, \omega_z$	vorticity components
$\Delta x, \Delta y, \Delta z$	mesh spacing of each direction
S	rate of stretching tensor
\mathcal{Q}	rate of rotation tensor
Q	Q invariant of velocity gradient tensor
c	chord length
Re	Reynolds number
U_0	free stream velocity
ν	kinematic viscosity
ρ	density
t	time
T	period of one pitch-oscillating cycle
Δt	time interval between two sequence image capturing
α	angle of attack
t_a	time period during which airfoil's angle of attack is varied
T^*	nondimensional rise time
α_0	amplitude angle during impulsive incidence variation
C_L	lift coefficient
C_{Lmax}	maximum lift coefficient
t'	nondimensional time
α_0	amplitude angle during pitch-oscillating motion
α_c	angle of the pitching center
f	frequency
k	reduced frequency
F	fluid force acting on the test model
F_{unst}	nondimensional unsteady fluid force
F_{st}	fluid force under stationary condition
P	propulsive force
M	momentum

Γ	circulation of the vortex ring
A	area surrounded by vortex line
F_x	propulsive force calculated from the vortex ring
F_z	force in the height direction calculated from the vortex ring
A_x	profile area in the x direction
A_z	profile area in the z direction

APPENDIX B: PROPULSIVE FORCE ESTIMATION PROGRAM BASED ON VORTEX RING MOMENTUM

```

%%%%%%%%%%%%%%%%%%%%%%%%%%%%%%%%%%%%%%%%%%%%%%%%%%%%%%%%%%%%%%%%%%%%%%%%%%%%%%
%   <<Program of Propulsive Force Estimation Based on Vortex Ring Momentum>>   %
%                                                                                   %
%   This program is calculating the time varying profile area and circulation   %
%       for each vortex ring in the wake of a monofin                           %
%                                                                                   %
%                                                                                   %
%                               2015. 12. 23                                     %
%                               by                                                %
%                               T. HANIU                                          %
%                                                                                   %
%%%%%%%%%%%%%%%%%%%%%%%%%%%%%%%%%%%%%%%%%%%%%%%%%%%%%%%%%%%%%%%%%%%%%%%%%%%%%%

clear all
close all

A = zeros(12, 36);
for T = 1 : 12
    for Vnum = 1 : 5
        clearvars -except NUM T Vnum A

        CSVFOLDA = 'FLODERNAME';
        AOA = [-40 -36 -28 -16 -8 -3 0 -1 -8 -19 -30 -38];
        AOAtc = [-40 -42 -42 -39 -27 -13 1 9 5 -6 -19 -30];

        listhire = dir('hire.csv');
        [imn h] = size(listhire);

```

```

name = char(listhire(1).name);
data = (dlmread(name, ',', 0, 0));
[yhire xhire] = size(data);
Y3 = data(:, 1:4);
X3 = data(:, 5:8);

Zhire(1 : floor(yhire / 4), 1) = 1.4;
Zhire(floor(yhire / 4) + 1 : floor(yhire / 4 * 2), 1) = 1.1;
Zhire(floor(yhire / 4 * 2) + 1:floor(yhire / 4 * 3), 1) = 0.9;
Zhire(floor(yhire / 4 * 3) + 1:floor((yhire / 4 * 4)), 1) = 0.7;

Z3(:, 1) = Zhire * 0;
Z3(:, 2) = Zhire * 0;
Z3(:, 3) = Zhire * 0 + 1;
Z3(:, 4) = Zhire * 0 + 1;
Z3 = Z3 * 10;

xh = 320;
for i = 1 : yhire
    for j = 1 : 4
        if X3(i, j) > xh
            X3(i, j) = xh;
        end
    end
end

omel = 2;

peaknum = (dlmread(sprintf('%s/circulation/peak_num_T%d.csv', CSVFOLDA, T), ',',
1, 1));
if peaknum(1, Vnum) ~ = 0
    bound = (dlmread(sprintf('%s / circulation / bound_T%d.csv', CSVFOLDA, T),
',', 1, 1));
    xu = bound(1, Vnum);
    xd = bound(2, Vnum);
    yf = bound(3, Vnum);

```

```

yb = bound(4, Vnum);
zu = bound(5, Vnum);
zd = bound(6, Vnum);
name = char(sprintf('%s/omega_%02.0f.mat', CSVFOLDA, T));
load(name);
name = char(sprintf('%s/omegax_%02.0f.mat', CSVFOLDA, T));
load(name);
name = char(sprintf('%s/omegay_%02.0f.mat', CSVFOLDA, T));
load(name);
name = char(sprintf('%s/omegaz_%02.0f.mat', CSVFOLDA, T));
load(name);
name = char(sprintf('%s/U_%02.0f.mat', CSVFOLDA, T));
load(name);
name = char(sprintf('%s/V_%02.0f.mat', CSVFOLDA, T));
load(name);
name = char(sprintf('%s/W_%02.0f.mat', CSVFOLDA, T));
load(name);
name = char(sprintf('%s/x_%02.0f.mat', CSVFOLDA, T));
load(name);
name = char(sprintf('%s/y_%02.0f.mat', CSVFOLDA, T));
load(name);
name = char(sprintf('%s/z_%02.0f.mat', CSVFOLDA, T));
load(name);
[nz ny nx] = size(omega0);

f = figure;
set(f, 'Position', [50, 50, 650, 600]);
set(gcf, 'Color', 'w');
set(0, 'defaultAxesFontSize', 20)
set(0, 'defaultAxesFontName', 'times new roman')
set(0, 'DefaultAxesLineWidth', 1);
hold on

s3 = patch(isosurface(x, y, z, omega0 * 0.27 / 0.5, omel));
set(s3, 'FaceColor', [0.3 0.7 0.7], 'EdgeColor', 'none', 'FaceAlpha', 0.3);
s3 = patch(isosurface(x, -y, z, omega0 * 0.27 / 0.5, omel));

```

```

set(s3, 'FaceColor', [0.3 0.7 0.7], 'EdgeColor', 'none', 'FaceAlpha', 0.3);

X4 = X3;
Z4 = Z3;
deg0 = A0Ate(1, T) - A0A(1, T);
count = 0;
for i0 = 45:157
X4 = X4 - X4(i0, 1);
Z4 = Z4 - Z4(i0, 1);
deg = -deg0 / (320 - X3(45, 1)) * (X4(i0 + 1, 1)) / 180 * pi;
clear x13 y13 z13 r13 X13 Y13

if i0 > 157
    x13 = X4(i0 : yhire + count, :);
    y13 = Z4(i0 : yhire + count, :);
    count = count + 1;
else
    x13 = X4(i0 : yhire, :);
    y13 = Z4(i0 : yhire, :);
end
end
[n h] = size(x13);
for i = 1 : n
    for j = 1 : h
        if x13(i, j) >= 0
            theta13(i, j) = atan(y13(i, j), x13(i, j));
            r13(i, j) = (x13(i, j)^2 + y13(i, j)^2)^0.5;
            X13(i, j) = r13(i, j) * cos(theta13(i, j) + deg);
            Y13(i, j) = r13(i, j) * sin(theta13(i, j) + deg);
        end
    end
end
X13(isnan(X13)) = 0;
Y13(isnan(Y13)) = 0;
    if i0 > 157
        X4(i0 : yhire + count, :) = X13;
        Z4(i0 : yhire + count, :) = Y13;
    else

```

```

        X4(i0 : yhire, :) = X13;
        Z4(i0 : yhire, :) = Y13;
    end
    X4 = X4;
    Z4 = Z4;
end

aoa = -A0A(1,T) / 180 * pi;
x14 = X4 - X4(1, 1);
y14 = Z4 - Z4(1, 1);
z14 = Y3;
[n h] = size(x14);
for i = 1 : n
    for j = 1 : h
        theta14(i, j) = atan2(y14(i, j), x14(i, j));
        r14(i, j) = (x14(i, j)^2 + y14(i, j)^2)^0.5;
        X14(i, j) = r14(i, j) * cos(theta14(i, j) + aoa);
        Y14(i, j) = r14(i, j) * sin(theta14(i, j) + aoa);
    end
end
X14(isnan(X14)) = 0;
Y14(isnan(Y14)) = 0;
Xfin(1 : yhire, :) = X14;
Yfin(1 : yhire, :) = Y3;
Zfin(1 : yhire, :) = Y14;
Xfin(yhire + 1:2 * yhire, :) = X14;
Yfin(yhire + 1:2 * yhire, :) = -Y3;
Zfin(yhire + 1:2 * yhire, :) = Y14;
p1 = surf(Xfin, Yfin + 5, Zfin);
set(p1, 'edgecolor', 'none', 'facecolor', 'k');

lighting phong;
light('position', [1, -1, 1]);
axis equal;

set(gca, 'XGrid', 'on', 'YGrid', 'on', 'ZGrid', 'on');

```

```

xlabel(' ¥itx / c');
hx = get(gca, 'xlabel');
ylabel(' ¥ity / c');
hy = get(gca, 'ylabel');
zlabel(' ¥itz / c');
hz = get(gca, 'zlabel');
xlim([0 1020]);
xlim([0 700]);
ylim([-300 300]);
zlim([-300 100]);
set(gca, 'xtick', 0 : 100 : 1020);
set(gca, 'ytick', -300 : 100 : 300);
set(gca, 'ztick', -300 : 100 : 100);

view(0, 0);
cam = 35;
camorbit(cam, 40);

xc = (xu + xd) / 2;
yc = (yf + yb) / 2;
zc = (zu + zd) / 2;

%% Vortex Core Center Detection%%
N = 36;

l0 = ((xd - xc)^2 + (yb - yc)^2)^0.5;
nr0 = floor(l0 / 10);
xr = zeros(floor((zu - zd) / 10), nr0, N);
yr = zeros(floor((zu - zd) / 10), nr0, N);
zr = zeros(floor((zu - zd) / 10), nr0, N);

xmeshnum = zeros(N, 1);
deg2 = atan2((yb - yc), (xd - xc));
for nt = 1 : N
    deg = (nt - 1) / N * 2 * pi - pi;
    if (deg <= deg2 && deg >= -deg2) || (deg >= pi - deg2) || (deg <= -pi +

```


deg2)

```

        l = abs((xd - xc) / cos(deg));
    else
        l = abs((yb - yc) / sin(deg));
    end
    nr = floor(l / 10);
    xmeshnum(nt, 1) = nr;
    for ir = 1 : nr
        for k = 1 : floor((zu - zd) / 10)
            xr(k, ir, nt) = (ir - 1) * 10 * cos(deg) + xc;
            yr(k, ir, nt) = (ir - 1) * 10 * sin(deg) + yc;
            zr(k, ir, nt) = (k - 1) * 10 + zd;
        end
    end
    p = mesh(xr(:, 1 : nr, nt), yr(:, 1 : nr, nt), zr(:, 1 : nr, nt));
    set(p, 'edgecolor', 'k', 'facecolor', 'none');
end

xrnon = (xr - min(min(min(x)))) / 10 + 1;
yrnon = (yr - min(min(min(y)))) / 10 + 1;
zrnon = (zr - min(min(min(z)))) / 10 + 1;

Ur = zeros(floor((zu - zd) / 10), nr0, N);
Vr = zeros(floor((zu - zd) / 10), nr0, N);
Wr = zeros(floor((zu - zd) / 10), nr0, N);
omegar = zeros(floor((zu - zd) / 10), nr0, N);
omegaxr = zeros(floor((zu - zd) / 10), nr0, N);
omegayr = zeros(floor((zu - zd) / 10), nr0, N);
omegazr = zeros(floor((zu - zd) / 10), nr0, N);

for nt = 1 : N
    for ir = 1 : nr0
        for k = 1 : floor((zu - zd) / 10)
            if ir <= xmeshnum(nt, 1)
                for I = floor(xrnon(k, ir, nt)) : floor(xrnon(k, ir, nt)) +

```

1

```

for J = floor(yrnon(k, ir, nt)) : floor(yrnon(k, ir, nt))
+ 1
for K = floor(zrnon(k, ir, nt)) : floor(zrnon(k, ir,
nt)) + 1
if (I > 0 && I <= nx) && (J > 0 && J <= ny) &&
(K > 0 && K <= nz)
Ur(k, ir, nt) = U(K, J, I) * (1 - abs(xrnon(k,
ir, nt) - I))...
* (1 - abs(yrnon(k, ir,
nt) - J))...
* (1 - abs(zrnon(k, ir,
nt) - K))...
+ Ur(k, ir, nt);
Vr(k, ir, nt) = V(K, J, I) * (1 - abs(xrnon(k,
ir, nt) - I))...
* (1 - abs(yrnon(k, ir,
nt) - J))...
* (1 - abs(zrnon(k, ir,
nt) - K))...
+ Vr(k, ir, nt);
Wr(k, ir, nt) = W(K, J, I) * (1 - abs(xrnon(k,
ir, nt) - I))...
* (1 - abs(yrnon(k, ir,
nt) - J))...
* (1 - abs(zrnon(k, ir,
nt) - K))...
+ Wr(k, ir, nt);
omegar(k, ir, nt) = omega0(K, J, I) * (1 -
abs(xrnon(k, ir, nt) - I))...
* (1 - abs(yrnon(k, ir,
nt) - J))...
* (1 - abs(zrnon(k, ir,
nt) - K))...
+ omegar(k, ir, nt);
omegaxr(k, ir, nt) = omegax0(K, J, I) * (1
- abs(xrnon(k, ir, nt) - I))...

```

```

* (1 - abs(yrnon(k, ir,
nt) - J))...
* (1 - abs(zrnon(k, ir,
nt) - K))...
+ omegaxr(k, ir, nt);
omegayr(k, ir, nt) = omegay0(K, J, I) * (1
- abs(xrnon(k, ir, nt) - I))...
* (1 - abs(yrnon(k, ir,
nt) - J))...
* (1 - abs(zrnon(k, ir,
nt) - K))...
+ omegayr(k, ir, nt);
omegazr(k, ir, nt) = omegaz0(K, J, I) * (1
- abs(xrnon(k, ir, nt) - I))...
* (1 - abs(yrnon(k, ir,
nt) - J))...
* (1 - abs(zrnon(k, ir,
nt) - K))...
+ omegazr(k, ir, nt);
end
end
end
end
else
xr(k, ir, nt) = xr(k, xmeshnum(nt, 1), nt);
yr(k, ir, nt) = yr(k, xmeshnum(nt, 1), nt);
zr(k, ir, nt) = zr(k, xmeshnum(nt, 1), nt);
end
end
end
end
s3 = patch(isosurface(xr, yr, zr, omegar * 0.27 / 0.5, omel));
set(s3, 'FaceColor', [0.3 0.7 0.7], 'EdgeColor', 'none', 'FaceAlpha', 0.7);

pnum = 50;
omep0 = zeros(pnum, 1, N);

```

```

omexp0 = zeros (pnum, 1, N);
omeyp0 = zeros (pnum, 1, N);
omezp0 = zeros (pnum, 1, N);
Up0 = zeros (pnum, 1, N);
Vp0 = zeros (pnum, 1, N);
Wp0 = zeros (pnum, 1, N);
xp0 = zeros (pnum, 1, N);
yp0 = zeros (pnum, 1, N);
zp0 = zeros (pnum, 1, N);
for nt = 1 : N
    for ir = 1 : xmeshnum(nt, 1)
        for k = 1 : floor((zu - zd) / 10)
            count = 0;
            count1 = 0;
            for I = ir - 1 : ir + 1
                for K = k - 1 : k + 1
                    if (I > 0 && I <= xmeshnum(nt, 1)) && (K > 0 && K <=
floor((zu - zd) / 10))
                        count1 = count1 + 1;
                        if omegar(k, ir, nt) >= omegar(K, I, nt)
                            count = count + 1;
                        end
                    end
                end
            end
        end
    end
    if count == count1
        c = 0;
        for ip = 1 : pnum
            if omegar(k, ir, nt) >= omep0(ip, 1, nt) && c == 0
                c = 1;
                for ip2 = pnum : -1 : ip + 1
                    xp0(ip2, 1, nt) = xp0(ip2 - 1, 1, nt);
                    yp0(ip2, 1, nt) = yp0(ip2 - 1, 1, nt);
                    zp0(ip2, 1, nt) = zp0(ip2 - 1, 1, nt);
                    omep0(ip2, 1, nt) = omep0(ip2 - 1, 1, nt);
                    omexp0(ip2, 1, nt) = omexp0(ip2 - 1, 1, nt);
                end
            end
        end
    end
end

```

```

        omeyp0(ip2, 1, nt) = omeyp0(ip2 - 1, 1, nt);
        omezp0(ip2, 1, nt) = omezp0(ip2 - 1, 1, nt);
        Up0(ip2, 1, nt) = Up0(ip2 - 1, 1, nt);
        Vp0(ip2, 1, nt) = Vp0(ip2 - 1, 1, nt);
        Wp0(ip2, 1, nt) = Wp0(ip2 - 1, 1, nt);
    end
    xp0(ip, 1, nt) = xr(k, ir, nt);
    yp0(ip, 1, nt) = yr(k, ir, nt);
    zp0(ip, 1, nt) = zr(k, ir, nt);
    omep0(ip, 1, nt) = omegar(k, ir, nt);
    omexp0(ip, 1, nt) = omegaxr(k, ir, nt);
    omeyp0(ip, 1, nt) = omegayr(k, ir, nt);
    omezp0(ip, 1, nt) = omegazr(k, ir, nt);
    Up0(ip, 1, nt) = Ur(k, ir, nt);
    Vp0(ip, 1, nt) = Vr(k, ir, nt);
    Wp0(ip, 1, nt) = Wr(k, ir, nt);
end
end
end
end
end
end
end
end

N0 = peaknum(1, Vnum);
N1 = peaknum(2, Vnum);
count = 0;
for nt = N0 : N1
    if peaknum(nt + 2, Vnum) == 0
    else
        count = count + 1;
        omep(count, 1) = omep0(peaknum(nt + 2, Vnum), 1, nt);
        omexp(count, 1) = omexp0(peaknum(nt + 2, Vnum), 1, nt);
        omeyp(count, 1) = omeyp0(peaknum(nt + 2, Vnum), 1, nt);
        omezp(count, 1) = omezp0(peaknum(nt + 2, Vnum), 1, nt);
        Up(count, 1) = Up0(peaknum(nt + 2, Vnum), 1, nt);
        Vp(count, 1) = Vp0(peaknum(nt + 2, Vnum), 1, nt);
    end
end

```

```

        Wp(count, 1) = Wp0(peaknum(nt + 2, Vnum), 1, nt);
        xp(count, 1) = xp0(peaknum(nt + 2, Vnum), 1, nt);
        yp(count, 1) = yp0(peaknum(nt + 2, Vnum), 1, nt);
        zp(count, 1) = zp0(peaknum(nt + 2, Vnum), 1, nt);
        [xs ys zs] = sphere(100);
        a = 10;
        surf(xs * a + xp(count, 1), ys * a + yp(count, 1), zs * a + zp(count,
1), ...
            'facecolor', 'r', 'edgecolor', 'none');
    end
end
Np = count;
xpp = xp;
xpp(Np + 1, 1) = xp(1, 1);
ypp = yp;
ypp(Np + 1, 1) = yp(1, 1);
zpp = zp;
zpp(Np + 1, 1) = zp(1, 1);
plot3(xpp, ypp, zpp, 'r--', 'linewidth', 2);
patch(xpp, ypp, zpp, 'r', 'edgecolor', 'none', 'facealpha', 0.7);

%% Profile Area Calculation %%
%Az
Sxy = 0;
for nt = 1 : Np
    nt1 = nt + 1;
    if nt == Np
        nt1 = 1;
    end
    a = ((xp(nt, 1) - xp(nt1, 1))^2 + (yp(nt, 1) - yp(nt1, 1))^2)^0.5;
    b = ((xp(nt, 1) - xc)^2 + (yp(nt, 1) - yc)^2)^0.5;
    c = ((xp(nt1, 1) - xc)^2 + (yp(nt1, 1) - yc)^2)^0.5;
    d = (a + b + c) / 2;
    Sxy = Sxy + (d * (d - a) * (d - b) * (d - c))^0.5;
    patch([xc xp(nt, 1) xp(nt1, 1) xc], [yc yp(nt, 1) yp(nt1, 1) yc], ...
        [zc zp(nt, 1) zp(nt1, 1) zc], 'r', 'edgecolor', 'none', 'facealpha',

```

```

0.7);

    end

    %Ax
    Syzp = 0;
    Syzn = 0;
    zpmin = min(zp);
    for nt = 1 : Np
        nt1 = nt + 1;
        if nt == Np
            nt1 = 1;
        end
        pon = (yp(nt1, 1) - yc) * (zp(nt, 1) - zpmin) - (yp(nt, 1) - yc) * (zp(nt1,
1) - zpmin);

        a = ((yp(nt, 1) - yp(nt1, 1))^2 + (zp(nt, 1) - zp(nt1, 1))^2)^0.5;
        b = ((yp(nt, 1) - yc)^2 + (zp(nt, 1) - zpmin)^2)^0.5;
        c = ((yp(nt1, 1) - yc)^2 + (zp(nt1, 1) - zpmin)^2)^0.5;
        d = (a + b + c) / 2;

        if pon > 0
            Syzp = Syzp + (d * (d - a) * (d - b) * (d - c))^0.5;
            patch([xc xp(nt, 1) xp(nt1, 1) xc], [yc yp(nt, 1) yp(nt1, 1) yc],...
                [zpmin zp(nt, 1) zp(nt1, 1) zpmin], 'r', 'edgecolor', 'none',
'facealpha', 0.7);
        elseif pon < 0
            Syzn = Syzn + (d * (d - a) * (d - b) * (d - c))^0.5;
            patch([xc xp(nt, 1) xp(nt1, 1) xc], [yc yp(nt, 1) yp(nt1, 1) yc],...
                [zpmin zp(nt, 1) zp(nt1, 1) zpmin], 'b', 'edgecolor', 'none',
'facealpha', 0.7);
        end
    end

end

%% Circulation Calculation %%
a = 100;
I = 0;
da = 10;

```

```

for i = -a : da : a
    I = I + 1;
    J = 0;
    for j = -a : da : a
        J = J + 1;
        pmx0(J, I) = 0;
        pmy0(J, I) = i;
        pmz0(J, I) = j;
    end
end
[nj, ni] = size(pmx0);

for nt = 1 : Np
    nts = nt - 1;
    if nts == 0
        nts = Np;
    end
    ntl = nt + 1;
    if ntl == Np + 1
        ntl = 1;
    end
    theta2(nt, 1) = (atan2(zp(ntl, 1) - zp(nts, 1), ((xp(ntl, 1) - xp(nts, 1))^2
+ (yp(ntl, 1) - yp(nts, 1))^2)^0.5));
    theta1(nt, 1) = (atan2(yp(ntl, 1) - yp(nts, 1), xp(ntl, 1) - xp(nts, 1)));

    rx1 = [cos(theta1(nt, 1)) -sin(theta1(nt, 1)) 0
           sin(theta1(nt, 1)) cos(theta1(nt, 1)) 0
           0 0 1];
    rx2 = [cos(theta2(nt, 1)) 0 -sin(theta2(nt, 1))
           0 1 0
           sin(theta2(nt, 1)) 0 cos(theta2(nt, 1))];
    I = 0;
    for i = -a : da : a
        I = I + 1;
        J = 0;
        for j = -a : da : a

```



```

    J = J + 1;
    x0y0z0 = [pmx0(J, I)
              pmy0(J, I)
              pmz0(J, I)];
    xyz = rx1 * rx2 * x0y0z0;
    pmx1(J, I) = xyz(1, 1);
    pmy1(J, I) = xyz(2, 1);
    pmz1(J, I) = xyz(3, 1);
end
end

if Vnum == 5
    if nt == Np / 2 - 1
        pmx(:, :, nt + 1) = pmx1 + xp(nt + 1, 1);
        pmy(:, :, nt + 1) = pmy1 + yp(nt + 1, 1);
        pmz(:, :, nt + 1) = pmz1 + zp(nt + 1, 1);
        pmx(:, :, nt) = pmx1 + xp(nt, 1);
        pmy(:, :, nt) = pmy1 + yp(nt, 1);
        pmz(:, :, nt) = pmz1 + zp(nt, 1);
    elseif nt == Np / 2 || nt == Np / 2 + 1
    elseif nt == Np / 2 + 2
        pmx(:, :, nt - 1) = pmx1 + xp(nt - 1, 1);
        pmy(:, :, nt - 1) = pmy1 + yp(nt - 1, 1);
        pmz(:, :, nt - 1) = pmz1 + zp(nt - 1, 1);
        pmx(:, :, nt) = pmx1 + xp(nt, 1);
        pmy(:, :, nt) = pmy1 + yp(nt, 1);
        pmz(:, :, nt) = pmz1 + zp(nt, 1);
    else
        pmx(:, :, nt) = pmx1 + xp(nt, 1);
        pmy(:, :, nt) = pmy1 + yp(nt, 1);
        pmz(:, :, nt) = pmz1 + zp(nt, 1);
    end
elseif peaknum(3, Vnum)~ = 0
    pmx(:, :, nt) = pmx1 + xp(nt, 1);
    pmy(:, :, nt) = pmy1 + yp(nt, 1);
    pmz(:, :, nt) = pmz1 + zp(nt, 1);

```

```

else
    if nt == 2
        pmx(:, :, nt - 1) = pmx1 + xp(nt - 1, 1);
        pmy(:, :, nt - 1) = pmy1 + yp(nt - 1, 1);
        pmz(:, :, nt - 1) = pmz1 + zp(nt - 1, 1);
        pmx(:, :, nt) = pmx1 + xp(nt, 1);
        pmy(:, :, nt) = pmy1 + yp(nt, 1);
        pmz(:, :, nt) = pmz1 + zp(nt, 1);
    elseif nt == Np - 1
        pmx(:, :, Np) = pmx1 + xp(nt + 1, 1);
        pmy(:, :, Np) = pmy1 + yp(nt + 1, 1);
        pmz(:, :, Np) = pmz1 + zp(nt + 1, 1);
        pmx(:, :, nt) = pmx1 + xp(nt, 1);
        pmy(:, :, nt) = pmy1 + yp(nt, 1);
        pmz(:, :, nt) = pmz1 + zp(nt, 1);
    elseif nt == Np
    else
        pmx(:, :, nt) = pmx1 + xp(nt, 1);
        pmy(:, :, nt) = pmy1 + yp(nt, 1);
        pmz(:, :, nt) = pmz1 + zp(nt, 1);
    end
end
end

for nt = 1 : Np
    p = mesh(pmx(:, :, nt), pmy(:, :, nt), pmz(:, :, nt));
    set(p, 'edgecolor', 'k', 'facecolor', 'none');
end

xrnon = (pmx - min(min(min(x)))) / 10 + 1;
yrnon = (pmy - min(min(min(y)))) / 10 + 1;
zrnon = (pmz - min(min(min(z)))) / 10 + 1;

Ucir = zeros(nj, ni, Np);
Vcir = zeros(nj, ni, Np);
Wcir = zeros(nj, ni, Np);

```

```

omegacir = zeros(nj, ni, Np);
omegaxcir = zeros(nj, ni, Np);
omegaycir = zeros(nj, ni, Np);
omegazcir = zeros(nj, ni, Np);
omeperp = zeros(nj, ni, Np);

for nt = 1 : Np
    nts = nt - 1;
    if nts == 0
        nts = Np;
    end
    ntl = nt + 1;
    if ntl == Np + 1
        ntl = 1;
    end
    dx = xp(ntl, 1) - xp(nts, 1);
    dy = yp(ntl, 1) - yp(nts, 1);
    dz = zp(ntl, 1) - zp(nts, 1);
    for i = 1 : ni
        for j = 1 : nj
            for I = floor(xrnon(j, i, nt)) : floor(xrnon(j, i, nt)) + 1
                for J = floor(yrnon(j, i, nt)) : floor(yrnon(j, i, nt)) + 1
                    for K = floor(zrnon(j, i, nt)) : floor(zrnon(j, i, nt)) + 1
                        if (I > 0 && I <= nx) && (J > 0 && J <= ny) && (K >
0 && K <= nz)
                            Ucir(j, i, nt) = U(K, J, I) * (1 - abs(xrnon(j,
i, nt) - I))...
                                                                * (1 - abs(yrnon(j, i, nt)
- J))...
                                                                * (1 - abs(zrnon(j, i, nt)
- K))...
                            + Ucir(j, i, nt);
                            Vcir(j, i, nt) = V(K, J, I) * (1 - abs(xrnon(j,
i, nt) - I))...
                                                                * (1 - abs(yrnon(j, i, nt)

```

$$\begin{aligned}
& - J)) \dots && * (1 - \text{abs}(\text{zrnon}(j, i, \text{nt}))) \\
& - K)) \dots && + \text{Vcir}(j, i, \text{nt}); \\
& \text{Wcir}(j, i, \text{nt}) = \text{W}(K, J, I) * (1 - \text{abs}(\text{xrnon}(j, \\
& i, \text{nt}) - I)) \dots && * (1 - \text{abs}(\text{yrnon}(j, i, \text{nt}))) \\
& - J)) \dots && * (1 - \text{abs}(\text{zrnon}(j, i, \text{nt}))) \\
& - K)) \dots && + \text{Wcir}(j, i, \text{nt}); \\
& \text{omegacir}(j, i, \text{nt}) = \text{omega0}(K, J, I) * (1 - \\
& \text{abs}(\text{xrnon}(j, i, \text{nt}) - I)) \dots && * (1 - \text{abs}(\text{yrnon}(j, i, \text{nt}))) \\
& - J)) \dots && * (1 - \text{abs}(\text{zrnon}(j, i, \text{nt}))) \\
& - K)) \dots && + \text{omegacir}(j, i, \text{nt}); \\
& \text{omegaxcir}(j, i, \text{nt}) = \text{omegax0}(K, J, I) * (1 - \\
& \text{abs}(\text{xrnon}(j, i, \text{nt}) - I)) \dots && * (1 - \text{abs}(\text{yrnon}(j, i, \text{nt}))) \\
& - J)) \dots && * (1 - \text{abs}(\text{zrnon}(j, i, \text{nt}))) \\
& - K)) \dots && + \text{omegaxcir}(j, i, \text{nt}); \\
& \text{omegaycir}(j, i, \text{nt}) = \text{omegay0}(K, J, I) * (1 - \\
& \text{abs}(\text{xrnon}(j, i, \text{nt}) - I)) \dots && * (1 - \text{abs}(\text{yrnon}(j, i, \text{nt}))) \\
& - J)) \dots && * (1 - \text{abs}(\text{zrnon}(j, i, \text{nt}))) \\
& - K)) \dots && + \text{omegaycir}(j, i, \text{nt}); \\
& \text{omegazcir}(j, i, \text{nt}) = \text{omegaz0}(K, J, I) * (1 - \\
& \text{abs}(\text{xrnon}(j, i, \text{nt}) - I)) \dots && * (1 - \text{abs}(\text{yrnon}(j, i, \text{nt}))) \\
& - J)) \dots &&
\end{aligned}$$

```

* (1 - abs(zrnon(j, i, nt)
- K))...
+ omegazcir(j, i, nt);
end
end
end
end
omeperp(j, i, nt) = abs(omegaxcir(j, i, nt) * cos(atan2(dy, dx))
* cos(atan2(dz, (dx^2 + dy^2)^0.5)))...
+ abs(omegaycir(j, i, nt) * cos(atan2(dx, dy)) *
cos(atan2(dz, (dx^2 + dy^2)^0.5)))...
+ abs(omegazcir(j, i, nt) * cos(atan2(dy, dz)) *
cos(atan2(dx, (dz^2 + dy^2)^0.5)));
end
end
AAAA = omegacir - omeperp;

count = zeros(nj, ni);
count((nj + 1) / 2, (ni + 1) / 2) = 1;
for k = 1 : (nj - 1) / 2 - 1
    for i = (ni + 1) / 2 - k : (ni + 1) / 2 + k
        for j = (nj + 1) / 2 - k : (nj + 1) / 2 + k
            if omeperp(i, j, nt) > 20 * 0.25
                for I = i - 1 : i + 1
                    for J = j - 1 : j + 1
                        if count(J, I) == 1
                            count(j, i) = 1;
                        end
                    end
                end
            end
        end
    end
end
end
end
for i = 1 : ni
    for j = 1 : nj

```

```

        if count(j, i) == 0
            omeperp(i, j, nt) = 0;
        end
    end
end
end
end

f = figure;
s3 = patch(isosurface(pmx, pmy, pmz, omeperp * 0.27 / 0.5, ome1));
set(s3, 'FaceColor', [0.3 0.7 0.7], 'EdgeColor', 'none', 'FaceAlpha', 0.9);
xlim([0 1020]);
ylim([-300 300]);
zlim([-300 300]);
view(0, 0);
cam = 35;
camorbit(cam, 40);

circu = 0;
l = 0;
for nt = 1 : Np
    nt1 = nt + 1;
    if nt1 > Np
        nt1 = 1;
    end
    l = l + ((xp(nt1, 1) - xp(nt, 1))^2 + (yp(nt1, 1) - yp(nt, 1))^2 + (zp(nt1,
1) - zp(nt, 1))^2)^0.5;
end
counttt = 0;
for nt = 1 : Np
    nt1 = nt + 1;
    if nt1 > Np
        nt1 = 1;
    end
    nt0 = nt - 1;
    if nt0 < 1
        nt0 = Np;
    end
end

```

```

end
l0 = (((xp(nt1, 1) - xp(nt, 1))^2 + (yp(nt1, 1) - yp(nt, 1))^2 + (zp(nt1,
1) - zp(nt, 1))^2)^0.5...
+ ((xp(nt0, 1) - xp(nt, 1))^2 + (yp(nt0, 1) - yp(nt, 1))^2 + (zp(nt0,
1) - zp(nt, 1))^2)^0.5) / 2;
l0 = l0 / l;
counttt = counttt + l0;
for i = 1 : ni
    for j = 1 : nj
        if omeperp(j, i, nt) > 20 * 0.25
            circu = circu + omeperp(j, i, nt) * 10 * 10 * 10^(-6) * l0;
        end
    end
end
end

if Vnum == 2 || Vnum == 4
    Sxy = -Sxy;
    Syzp = -Syzp;
    Syzn = -Syzn;
end
A(T, 1 + ((Vnum - 1) * 9)) = T;
A(T, 2 + ((Vnum - 1) * 9)) = (T - 1) / 12;
A(T, 3 + ((Vnum - 1) * 9)) = Sxy;
A(T, 4 + ((Vnum - 1) * 9)) = Syzp;
A(T, 5 + ((Vnum - 1) * 9)) = Syzn;
A(T, 6 + ((Vnum - 1) * 9)) = Syzp - Syzn;
A(T, 7 + ((Vnum - 1) * 9)) = (Sxy^2 + (Syzp - Syzn)^2)^0.5;
A(T, 8 + ((Vnum - 1) * 9)) = circu;
else
    A(T, 1 + ((Vnum - 1) * 9)) = T;
    A(T, 2 + ((Vnum - 1) * 9)) = (T - 1) / 12;
    A(T, 3 + ((Vnum - 1) * 9)) = 0;
    A(T, 4 + ((Vnum - 1) * 9)) = 0;
    A(T, 5 + ((Vnum - 1) * 9)) = 0;
    A(T, 6 + ((Vnum - 1) * 9)) = 0;

```

$$A(T, 7 + (Vnum - 1) * 9) = 0;$$

$$A(T, 8 + (Vnum - 1) * 9) = 0;$$

end

end

end